National Technical University of Athens
School of Naval Architecture and Marine Engineering
Shipbuilding Technology Laboratory

Corrosion behavior of super-hydrophobic surfaces on copper substrate in 3.5% NaCl solution

FOURKAS VLASIOS

SUPERVISOR, PROFESSOR D.I. PANTELIS

ATHENS 2014

Acknowledgements

For this project, which took me over one year to complete, I have been supported and assisted by many people, who I would like to thank and express my gratitude.

Firstly, I would like to thank my supervisor, Professor D.I. Pantelis, for his trust, support and encouragement throughout my entire effort.

I would like to especially thank Mrs. Tsiourva for her guidance, help and support, Dr A. Kontos and P. Falaras from National Center of Scientific Research, Demokritos for the contact angle measurements and SEM images. During my experimental work I received a great deal of help from the technical staff of the laboratory to whom I express my gratitude.

Table of Contents:

Abstract

A novel method for the formation of a composite super-hydrophobic film, composed of flower-like surface nanostructures, and how that innovative super-hydrophobic film affects corrosion behavior of the material, was studied within the present paper. The film was formed on fresh copper surface. The super-hydrophobic film was pretreated by myristic acid (*n*-tetradecanoic acid), ($CH_3(CH_2)_{12}COOH$), chemically adsorbed onto the copper wafer. The film structure was probed with contact angle measurement (CA), scanning electron microscopy (SEM), and atomic force microscopy (AFM). Moreover, the corrosion resistance of bare and modified samples in 3.5% NaCl, were investigated by Open Circuit and Potentiodynamic Polarization Measurements (PPM). Experimental results show that the corrosion resistance of Cu with super-hydrophobic surface was improved remarkably, because of its unique nanostructure. All experimental results proved that the super-hydrophobic surface can improve the corrosion resistance of copper significantly. The air trapped in the nano-crevices of the film was suggested to be responsible for the superior water-repellent property.

Περίληψη

Στα πλαίσια της παρούσας διπλωματικής μελετήθηκε μια καινοτόμος μέθοδος σχηματισμού σύνθετης υπερ-υδρόφοβης επιφάνειας, αποτελούμενης από νανοδομές υπό την μορφή λουλουδιών (flower-like surface nanostructures) και πως αυτή η καινοτόμος υπερ-υδρόφοβη επιφάνεια επηρεάζει τη συμπεριφορά του υλικού σε διάβρωση.

Το στρώμα σχηματίστηκε πάνω σε ενεργή επιφάνεια χαλκού, η οποία προηγουμένως είχε λειανθεί έως 1500 SiC και προσβληθεί με HNO_3, για την απομάκρυνση τυχόν οξειδίων. Η υπέρ-υδρόφοβη επιφάνεια σχηματίστηκε με την εμβάπτιση των δοκιμίων σε διάλυμα μυριστικού οξέος ($CH_3(CH_2)_{12}COOH$) 0.06M, σε αιθανόλη, το οποίο προσροφάται χημικά πάνω στην επιφάνεια του χαλκού. Για τη μελέτη της υπερ-υδρόφοβης επιφάνειας που προέκυψε, πραγματοποιήθηκαν μετρήσεις της Γωνίας Επαφής (Contact Angle), παρατηρήσεις στο Ηλεκτρονικό Μικροσκόπιο Σάρωσης (SEM), και σε Μικροσκόπιο Ατομικής Δύναμης (AFM). Η συμπεριφορά σε διάβρωση μελετήθηκε με ηλεκτροχημικές μετρήσεις Ανοιχτού Κυκλώματος (Open Circuit), καθώς και Ποτενσιοδυναμικές Καμπύλες Πόλωσης (PPM), σε διάλυμα NaCl 3.5%.

Όλα τα πειραματικά αποτελέσματα απέδειξαν σαφή βελτίωση της συμπεριφοράς σε διάβρωση των υπερ-υδρόφοβων επιφανειών. Ο παγιδευμένος αέρας στις νάνο-εσοχές της οργανικής επίστρωσης που δημιουργήθηκε θεωρείται ότι παρέχει τις υπέρ-υδρόφοβες ιδιότητες των χημικά προσβεβλημένων επιφανειών.

1. Introduction

The superhydrophobicity (hydrophobicity) of solid surfaces has been investigated with considerable attention over the past few years and remarkable progress has been achieved. It has been discovered that water droplets on hydrophobic surfaces can exhibit a contact angle higher than 90°, and some can even be approaching approximately up to 180°. In particular, the contact angles related to superhydrophobic (or ultrahydrophobic) surfaces are greater than 150°. And those superhydrophobic surfaces are very likely to have phenomenal roughness with micro- or nanosized (or even smaller) protrusions coming out of the surface. Therefore, the liquid might contact only a few bits of the superhydrophobic surface with- out fully wetting it. Indeed, fluid interacting with superhydrophobic surfaces is one important discipline of research in the 21st century, and can essentially influence a lot of cutting-edge topics in engineer- ing and biotech research which involve surface structures, fluid motivation, and their physical and chemical properties. Basically, the contact angle related wetting phenomena are of great interest and importance to current research progress. A considerable amount of work has been carried out to study the involved mechanisms and principles. Interestingly, many methods that are used to create manmade superhydrophobic surfaces are inspired by the “Lotus Effect”. Recent research has indicated that there are even more superhydrophobic surfaces in nature and this helps to promote the applications of biomimetic ideas into practical fields.

Also, it is noticed that the underlying theories interpreting the phenomena are mainly focused on Young equation, Wenzel equation, and Cassie–Baxter equation, while the wetting phenomena have been studied over the past decade. Based on these theories, people have understood that either surface energy or surface structure (roughness) can influence the contact angle of liquid droplets on solid surfaces. However, such equations are not sufficient to thoroughly explain the mechanisms of wetting phenomena, although they are still necessary. This review attempts to discuss concisely the most recent research progress into the superhydrophobicity of solid surfaces with regard to the wetting process, both theoretically and experimentally. From an overall point of view, the work dis- cussed in this paper will include reviewing the fundamental theories and their complement, the superhydrophobic surfaces that are discovered in nature, the way manmade superhydrophobic surfaces are prepared, the functions and applications of these surfaces, and emphasize on their corrosion resistance and general behaviour against corrosion. Finally, we will provide our conclusions and outlook on the future of superhydrophobic field.

2. Theoretical models [1][3][4][5][19][20][22]

As discussed in the Introduction, although some research work has been undertaken to study the wetting phenomena on superhydrophobic surfaces, there are still quite a few critical questions remaining unsolved. For example, it is not yet fully known how and when a stable wetting state can be achieved. An interesting observation that both homogeneous and heterogeneous wetting states could coexist on the same surface, as shown in Fig. 1, was reported by Callies and Quéré in 2005

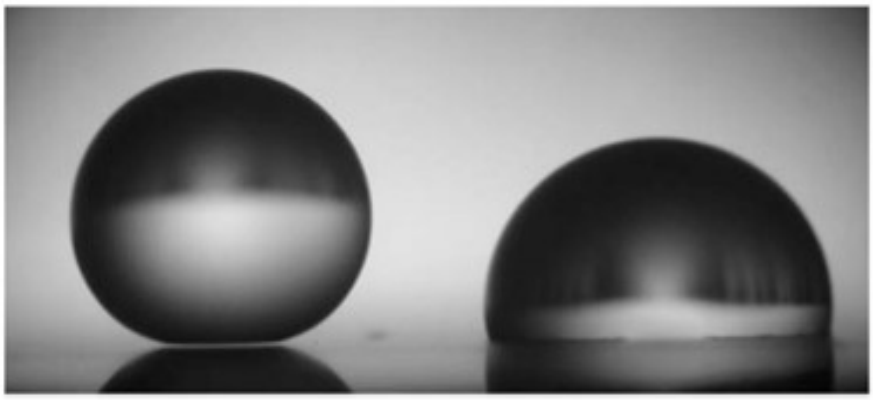

Fig. 1. Millimetric water drops (of the same volume) deposited on a superhydrophobic substrate. The heterogeneous state (left) and homogeneous state (right) can coexist [3]

the homogeneous state (Fig. 1, right) could be obtained by pressing one liquid droplet in the heterogeneous state (Fig. 1, left) against the solid substrate. This meant the state of a droplet on a solid surface was somehow related to the process how the droplet was delivered and formed. However, it was also suggested by other research work that the wetting state should be induced by surface roughness. To clarify the complex wetting process and mechanism, this section focuses on the fundamental theories of wet- ting, involving contact angles, wetting models, state transitions, and the role of surface energy.

2.1. Wetting Models

The starting point of a wetting model is defined by the Young equation, derived for a sessile drop on an ideal rigid, homogeneous, flat and inert surface. The drop contacts its substrate on a disk (radius = R) where the three phases of the system coexist, and the so-called three phase contact line is formed, as shown in Fig. 2.

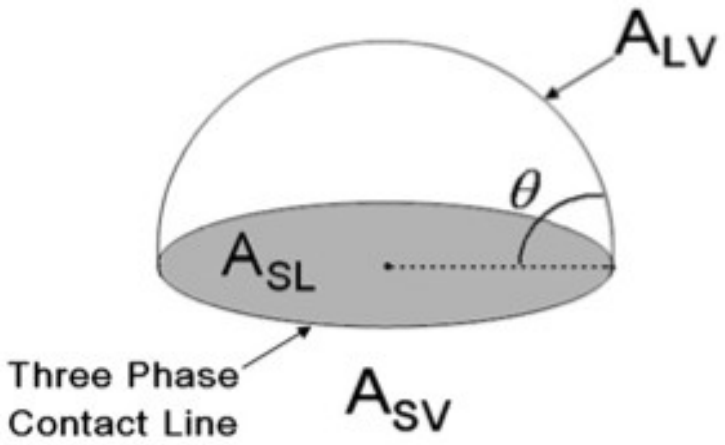

Fig. 2. A liquid drop showing contact angle θ balanced by three interfaces. The letter 'A' indicates the interfaces as well as their contact areas. SV, SL and LV correspond to the interfaces between solid, liquid and vapor respectively. [3]

The liquid joins the solid at a contact angle θ. Each interface draws the contact line so as to minimize the corresponding surface area, balancing the surface tensions on the direction of potential motion so that there will yield a relation attributed to Young, as shown in Eq. (2.1), although it does not explicitly show up in Young's publication:

$$cos\theta = \frac{(\gamma_{SV} - \gamma_{SL})}{\gamma_{LV}} \qquad 2.1$$

where γ is the surface tension that indicates the energy per unit surface area of the interface. The Young equation unambiguously relates the intrinsic contact angle θ (Young Contact Angle) to interfacial tensions (energies). However, since real surfaces usually vary in the surface conditions, most scenarios regarding contact angles in practice cannot be fully explained by the Young equation. Wenzel then proposed an equation relating the contact angle to surface roughness and surface energies. It can be written as:

$$r(\gamma_{SV} - \gamma_{SL}) = \gamma_{LV} cos\theta'_{W} \qquad 2.2$$

where θ'w is the apparent Wenzel contact angle, which measures the apparent contact angle

influenced by the roughness of solid surfaces. r corresponds to the “roughness factor”, also referred to as the roughness area ratio of the actual surface with respect to the geometric surface. The reformed Wenzel equation is normally written as:

$$cos\theta'_W = r\,cos\theta \qquad 2.3$$

The Wenzel equation assumes the water will penetrate into the grooves caused by the surface roughness, and therefore the Wenzel equation is related to the homogeneous wetting regime. The ‘apparent’ Wenzel contact angle θ'w is in contrast with the ‘real’ angle θ, because close inspection of a rough surface would always reveal the ‘real’ contact angle on any element that could be regarded as smooth. The measurement of contact angles might therefore be somewhat arbitrary, for one might pursue this argument to molecular or atomic dimensions. Fortunately, for practical purposes, it is possible to have a reasonable division of surfaces into ‘smooth’ and ‘rough’. The Wenzel equation states that the wettability can be improved by the surface roughness for a hydrophilic surface, but might get worse for a hydrophobic one .

In general, there are two types of stable wetting states, namely, homogeneous wetting state and heterogeneous wetting state, and the metastable states in-between. While the Wenzel equation is applicable to the homogeneous wetting regime, the Cassie–Baxter equation corresponds to the heterogeneous wetting regime. If the surface roughness is illustrated as pillars or protrusions, the 2-dimensional schematics of those wetting states can be shown in Fig. 3.

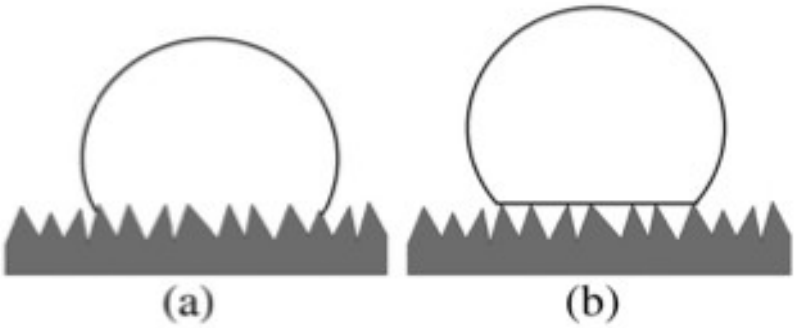

Fig. 3. The homogeneous wetting state (a) and heterogeneous wetting state (b). The liquid drop in the homogeneous wetting state follows the solid surface and penetrates into the grooves caused by the protrusions; the liquid drop in the heterogeneous wet- ting state only contacts the top of the protrusions, leaving air below into the grooves. [3]

Thus, a homogeneous state corresponds to the fact that the liquid drop fills up the roughness grooves [Fig. 3(a)] and the Wenzel equation is applied; a heterogeneous state refers to the fact that air bubbles are entrapped inside the grooves underneath the liquid [Fig. 3(b)] and the Cassie–Baxter (CB) equation is then applied. In the heterogeneous state, the liquid only contacts the solid at the top of the protrusions on a fraction denoted as φs , which is the ratio of the total area of the solid–liquid interface with respect to the total area of solid–liquid and liquid–air interfaces in a plane geometrical area of unity parallel to the rough surface. If only air was present between the solid and the liquid, the ‘contact angle’ would be 180°. The contact angle θ' of a “fakir” drop (Fig. 1, left) is caused by both the solid and the air, and this yields:

$$cos\theta' = -1 + \varphi_S(cos\theta + 1) = \varphi_S . cos\theta + \varphi_S - 1 \quad 2.4$$

Besides, if we turn to the ratio of the actual wetted area to the projected area, r_f, which is also referred to as the roughness ratio of the fraction, it will give rise to the modified form of the CB equation:

$$cos\theta'_{CB} = r_f . \varphi_S . cos\theta + \varphi_S - 1 \quad 2.5$$

When $\varphi_S = 1$ and $r_f = r$, the CB equation turns into the Wenzel equation. Eq. (2.5) interprets the multilayered roughness and is more suitable for the hierarchical surface structure, which has been found much morphologically closer to the natural model of superhydrophobic surfaces. Thus it is conceived that both surface roughness and its structure (morphology) can have impact on the value of contact angles and therefore the states of wetting. If the intrinsic contact angle of a water-repelling surface is fixed for a particular material, it will be the way to prepare the surfaces that determines the surfaces' wettability.

To sum up briefly for this part, the Young equation builds up the basic theory for wetting phenomena on ideal smooth surfaces. The Wenzel equation is valid if the surface is homogeneously wetted, while the CB equation applies to a heterogeneous state. At this point, it seems that people have already got the theoretical support to study those involved scenes. However, the real situation is not that simple. As recently realized, both Wenzel equation and CB equation could be correct only if the drop is sufficiently large compared with the typical roughness scale. It is still under debate that when and how a stable wetting state can be achieved. Also, there might be a transition between homogeneous state and heterogeneous state, and it is even not fully understood how this transition happens. Thus, we can only say that those mentioned theories are to some extent necessary, but not sufficient for entirely describing wetting phenomena on solid surfaces. To solve these questions, further investigation related to the wetting process is needed. In the following section, we will discuss the issues of contact angles to interpret the involved mechanisms.

2.2. Contact Angles and their Hysteresis

After a series of experiments to test the water repellence on fractal surfaces. One typical process was to prepare fractal surfaces made of alkylketene dimer (AKD) and measure the contact angles. The maximum contact angle reported in their work was 174°, as shown in Fig. 4.

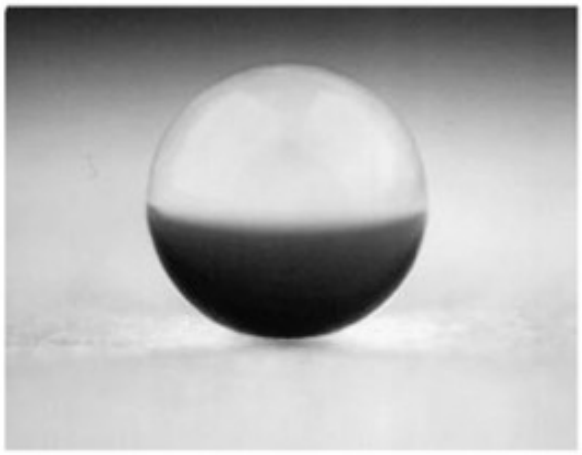

Fig. 4. A water droplet of which the contact angle is 174° placed on the AKD surface [3]

They argued that the maximum contact angle could be approaching to 180° if there was no adsorption. This was a sparking point in the long run of studying contact angles on superhydrophobic surfaces, for it opened the door of possibility for succeeding researchers to approach the extremely high contact angles in practical fields. Afterwards, there indeed were a few reported cases of high contact angles. Some researchers even reported contact angles up to 180°. Fig. 5 shows a few cases of the extremely high contact angles of liquid droplets on superhydrophobic surfaces.

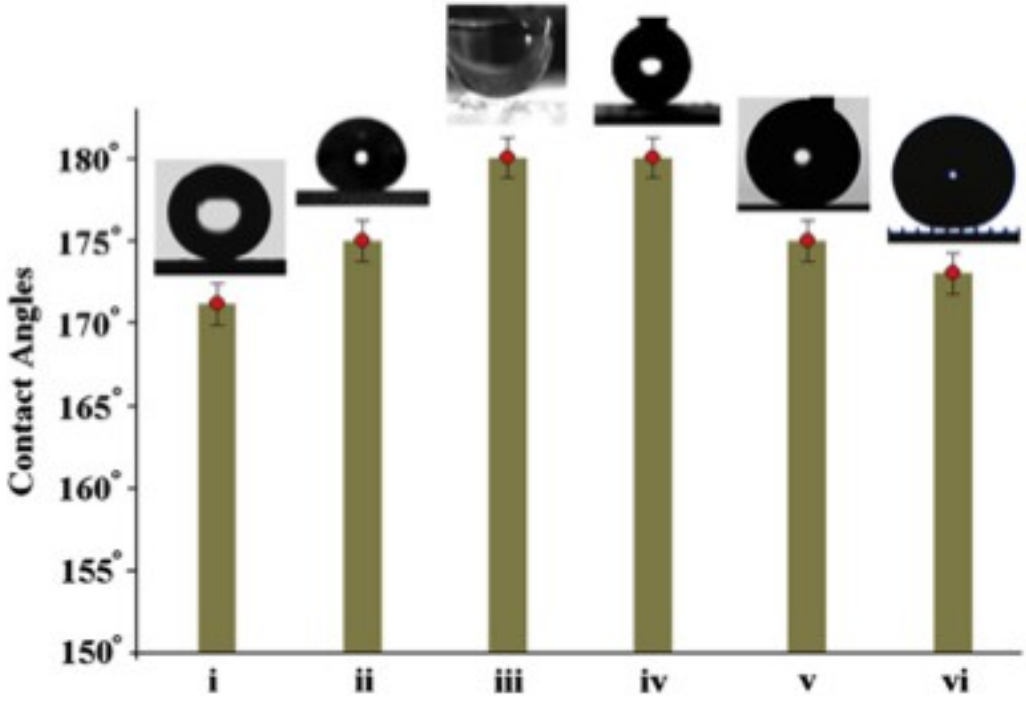

Fig. 5. High contact angles of liquid droplets on artificial superhydrophobic surfaces. i: 171.2±1.6°, measured on poly(vinyl alcohol) nanofibers; ii: 175±0.7°, mea- sured on the coating of SiO2 nanoparticles; iii: 180°, measured on submicrometered particles of tetrafluoroethylene oligomers; iv: 180°, measured on fluorinated nanoparticles; v: 175–180°, achieved by using DRIE patterning of con- trolled parameters; vi: 173(−3, +6)°, achieved by using silicon etching and gas phase isotropic etching. [3]

However,there was no clear interpretation for the contact angle hysteresis (CAH) in the experiment and theory related to the aforementioned AKD superhydrophobic surfaces. Also, the lack of completely consistent measurement standards might make other high contact angles uncertain to decide. Because of the contact angle hysteresis, the maximum value of a measured contact angle is not the only criterion to define a stable superhydrophobic state. To describe a superhydrophobic state, the static angle as well as the CAH should be measured both. For an extremely stable superhydrophobic state, its static contact angle should be as high as possible, and its CAH as small as possible, otherwise the achieved wetting state might transit to a different one.

Also, the fitting modes that people adopted to measure the contact angles can affect their values: it was reported that ellipse fitting, circle fitting, tangent searching, and Laplace–Young fitting could cause various values of contact angles of similarly shaped droplets as shown in Fig. 6. That's why the liquid drops in Fig. 5 just look similar but have different values. Therefore, the fitting mode should be clearly mentioned to reflect the real situation of wetting.

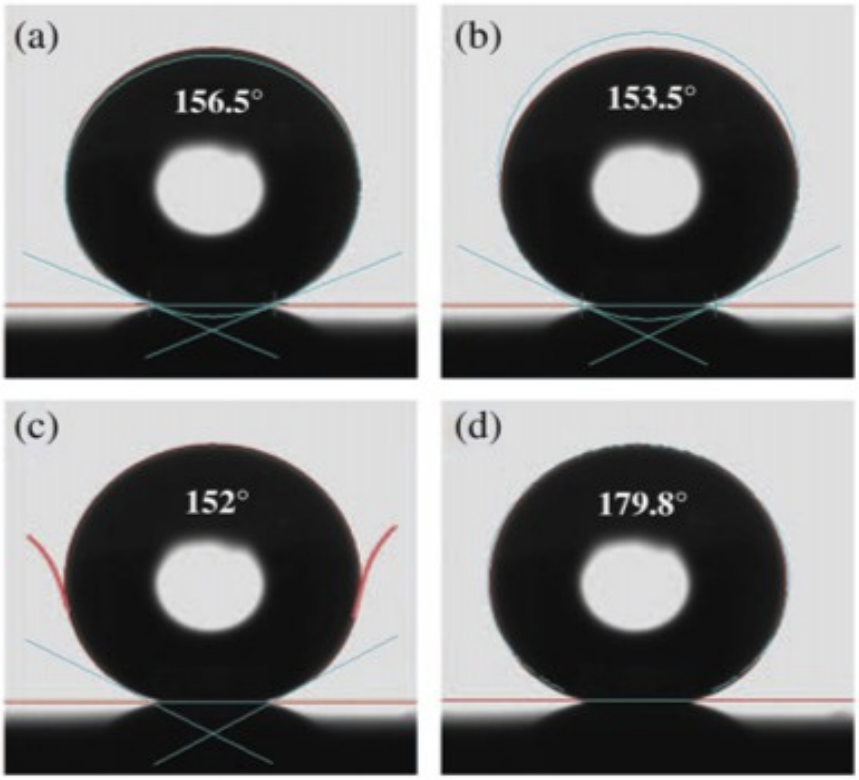

Fig. 6. Ellipse fitting (a), circle fitting (b), tangent searching (c), and Laplace–Young fit- ting (d) make static contact angles of the same water droplet different. The figures include the simulation lines of the profile of the water droplets and the horizontal baselines. [3]

On the other hand, the CAH can be explained schematically in two manners. First, as shown in Fig. 7, the liquid drop will advance at the lower side and recede at the upper side when the substrate is inclined at θD, which is the sliding angle. In order to let the liquid droplet slide off, the substrate must be tilted at/over the sliding angle. On this occasion, the liquid wets the substrate at the advancing point and dewets it at the receding point. Thus, θA is the advancing contact angle and θR is the receding contact angle. They stay constant during the sliding process as long as the surrounding conditions don't change.

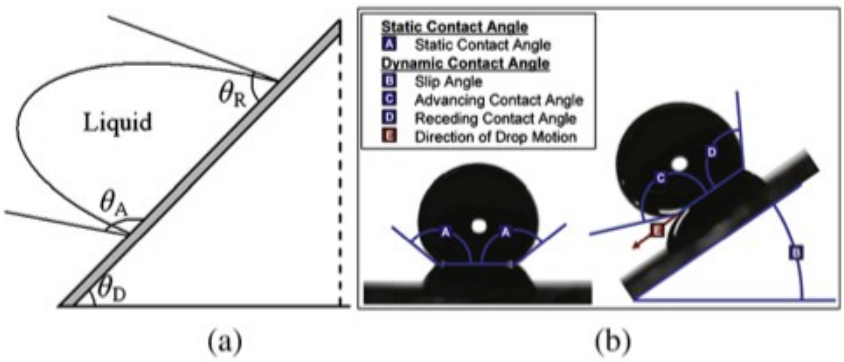

Fig. 7. (a) A liquid drop theoretically sliding on a declination of θD without acceleration. θA is the advancing angle, and θR is the receding angle. (b) The schematic of static contact angle and dynamic contact angles. [3]

Secondly, if one withdraws liquid from a droplet on the solid surface, the volume of the droplet as well as the contact angle will decrease, but the contact area of the droplet on the surface will not change until it begins to recede, as shown in Fig. 8(a). Similarly, if one adds water to the droplet, the volume as well as the contact angle will increase, but the contact area will not change until the droplet begins to advance, as shown in Fig. 8(b). Thus, the contact angles during receding and advancing are denoted as receding contact angle θ_R and advancing contact angle θ_A, respectively. The difference between advancing and receding contact angles is termed as the CAH. Corresponding to the description, a typical experimental process of CAH is shown in Fig. 8(c). The contact angle of a metastable droplet formed on a solid surface can be at any value between receding and advancing contact angles. Some CAH is quite low, within 5° , which does not affect the superhydrophobicity dramatically. However, some can be as much as 40°, which might even change the wetting state. From this point of view, it is not only the static contact angle but also the receding and advancing contact angles that can characterize a surface.

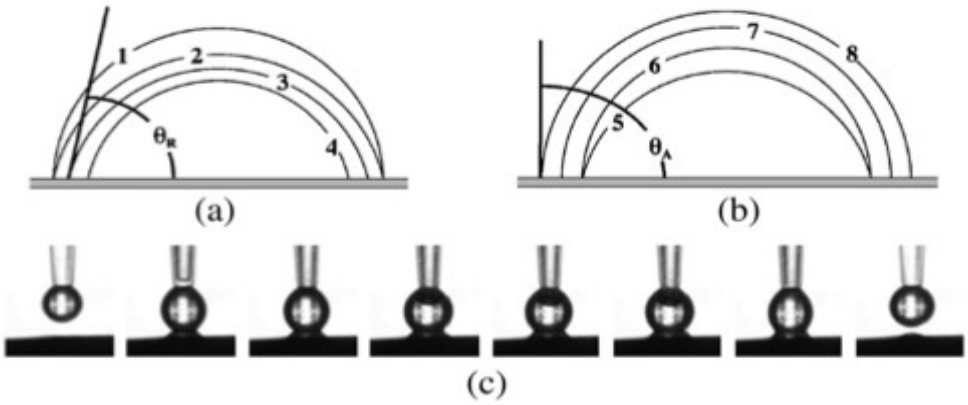

Fig. 8. (a) The droplet is pinned at the three-phase contact line until θR is reached at stage 2 and θR remains constant, if external force and/or energy is not considered, during sub- sequent volume decreasing. (b) The droplet is pinned at the three-phase contact line until θA reaches stage 6. (c) A growing and shrinking drop sequence. [3]

2.3. Surface tension and surface free energy

Although the surface tension is referred to as the free energy per unit area, it can also be equally thought of as the force per unit length, which is measured in N/m. The surface free energy is an important characteristic of every surface or interface. In the bulk of the body, chemical bonds exist between the molecules. To break the chemical bonds, a certain amount of energy has to be applied. Molecules that do not form bonds at the side of the surface have higher (potential) energy than those that form the bonds. This additional energy caused by the higher energy is called surface or interface free energy and measured in the energy per area units, that is, in the SI system, J/m^2. Thermodynamically, the concepts of surface tension, surface tension force, surface energy density, and surface free energy are different. However, these concepts, in most cases studying superhydrophobic or superhydrophilic surfaces, are now numerically equivalent to each other when temperature and pressure are assumed constant. To make it clear, it is necessary to assume that there is no adsorption at the interfaces as well. That's the ideal condition for the assumption that the surface tension is equivalent to the surface free energy. For a superhydrophobic surface, the dry area should have lower surface energy than the wet area. And the shape of a droplet on the superhydrophobic surface spontaneously assumes a more spherical shape to minimize its energy. Thus the liquid–air surface is promoted. The surface roughness can adjust the effect of surface energy as an amplifier. Hence a liquid droplet forms a high contact angle on the rough low-energy surface and a low contact angle on the rough high-energy surface.

2.4. Wetting transitions

It is no doubt that those that obtained high contact angles mentioned above should be due to the superhydrophobicity of the surfaces, which can be prompted in quite a few manners (see subsequent sections). However, for most cases, the wetting state has not been presented clearly when a high contact angle is shaped up. As stated previously, Wenzel and Cassie–Baxter states might be both suitable for superhydrophobic surfaces; but on the other hand, whether or not the liquid droplet rests partially on the solid surface as well as the air respectively is still under investigation. Also, the CAH in the CB state can be normally lower than in the Wenzel state, and there- fore CB state might be more stable. There is an apparent difference between those two states. If the CAH is relatively big, a transition might happen, and this makes the wetting less stable or metastable. It is noted from our aforesaid discussion that the advancing contact angle related to a 'superhydrophobic' surface might be greater than 150° and the receding contact angle less than 150°. When it comes down to a hydrophobic surface, the advancing contact angle might be greater than 90° and receding contact angle less than 90°. Strictly speaking, these states are not 100% superhydrophobic or hydrophobic, as the advancing and receding contact angles can change the wetting states. It should be attributed to the incongruous and inhomogeneous distribution of structural and chemical properties on the surface. That is to say, those factors including structural and chemical properties and even adhesive force can cause the hysteresis of contact angles and pinning of liquid droplets. Thus, we continue to discuss the transition based on contact angles between wetting states.

2.4.1. *Critical contact angle*

Bico et al. suggested a critical contact angle θc between Wenzel state and CB state by equating Eq. (2.3) with Eq. (2.4). This critical contact angle was determined by the surface design. That the air was entrapped into the surface grooves should be favored only if θ was greater than θc. Moreover, the impact from r_f, the rough- ness ratio of projected protrusions, will need to be included into the critical contact angle for further investigation. Thus, after equating Eq. (2.3) with Eq. (2.5), one can get:

$$\cos\theta'_C = \frac{(1-\varphi_S)}{(r_f.\varphi_S - r)} \qquad 2.6$$

where θ_c' is the critical contact angle with the effect of r_f. Then the homogeneous wetting will be preferred only if the Young contact angle is smaller than θ_c' , otherwise the drop will exhibit a heterogeneous wetting state, theoretically, as shown in Fig. 9. However, it has been found in many cases that the CB state can exist in a scenario of moderate contact angles, which means that Wenzel and CB states may even coexist on the same particular surface. Our previous research indicates that how the droplet is delivered or formed also has much to do with the contact angle. As shown in Fig. 10, the contact angle decreased from around 170° to around 145° when the droplet was being pressed to spread on the substrate. Meanwhile, the advancing and receding angles changed with the con- tact angles. From this point of view, the state of a liquid droplet on a solid surface is related to

how the droplet adapts itself with the surface. This gives rise to the design of superhydrophobic surfaces because a transition between the two states can cause a significant change of contact angles as mentioned earlier on.

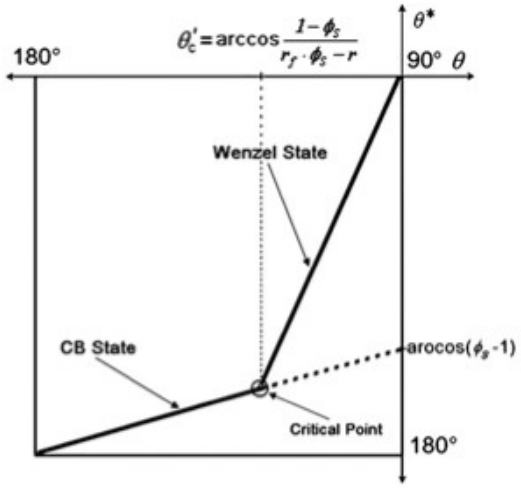

Fig. 9. Wenzel and CB wetting models with impact from rf. Theoretically, Wenzel state: 90°<θ<θc' ; CB state: θc' <θ<180°. However, the CB regime can also be observed for θ<θc' , shown as the dotted line after the critical point. [3]

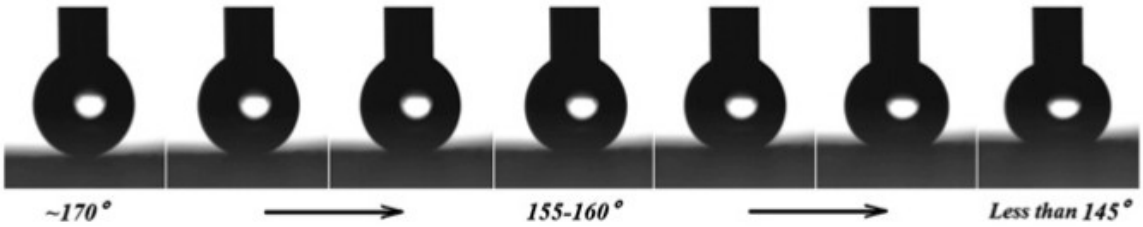

Fig. 10. Contact angles varying from around 170° to less than 145°. [3]

2.4.2. *Energy equations*

The transitions occur between the wetting states: either from CB state to Wenzel state or from Wenzel state to CB state. We herein discuss the transitions from an energetic point of view. Patankar has supposed that the shape of the droplet in equilibrium state is energetically minimized for a given value of the apparent contact angle θ':

$$G = A_{LV} \cdot \gamma_{LV} - \cos\theta' \cdot A_{SL} \cdot \gamma_{LV} \qquad 2.7$$

where:

$$\cos\theta' = (\gamma_{SV} - \gamma_{SL})^{eff} / \gamma_{LV}$$
$$A_{LV} = 2\pi R^2 (1 - \cos\beta) \qquad 2.8$$
$$A_{SL} = \pi R^2 \sin^2\beta$$

$(\gamma_{SV}-\gamma_{SL})_{eff}$ is assumed as the effective energy per unit area of liquid–substrate contact (interface) with respect to the dry substrate. β is the contact angle of the droplet formed on the substrate surface. G is the energy change from the initial state to the final state. And for a given apparent contact angle θ', the energy of the droplet is minimized. The energy change is:

$$\frac{G}{(9\pi^{(1/3)} V^{(2/3)} \gamma_{LV})} = (1 - \cos\theta')^{(2/3)} (2 + \cos\theta')^{(1/3)} \qquad 2.9$$

From the right side of Eq. (2.9), it's noted that the energy increases with θ' monotonically when $0° \le \theta' \le 180°$. Consequently, a higher apparent contact angle will lead to a higher energy and vice versa.

To include the impact from surface roughness, we establish a theoretical setup which is rough with surface protrusions , as shown in Fig. 11. It can be noticed that ALV should have covered the liquid-vapor interface inside the contact area under the drop and ASL should have included the effect caused by surface geometry as well. Thus, we include the surface roughness and the fraction of the protrusions (pillars) to reform the energy equations for heterogeneous and homogeneous wetting states respectively.

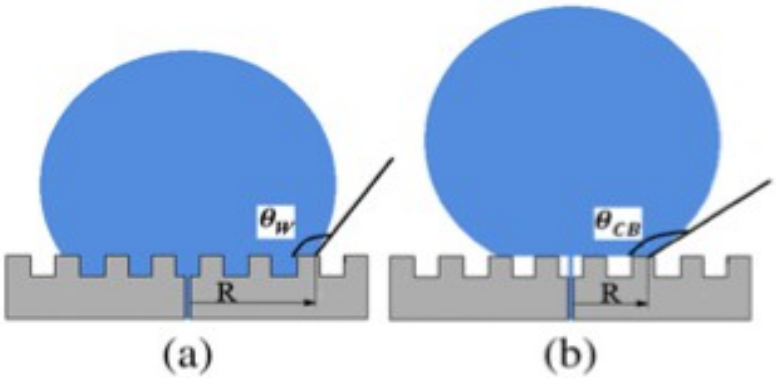

Fig. 11. Filling the liquid up to a rough surface through the solid substrate: (a) homogenous Wenzel fashion; (b) heterogeneous CB fashion. R is the radius of the circular con- tact area between solid and liquid. [3]

For a heterogeneous wetting state, the contact areas of liquid–vapor and solid–liquid interfaces are:

$$A'_{LV} = 2\pi R^2 (1 - \cos\beta) + (1 - \varphi_S) \pi R^2 \sin^2\beta \qquad 2.10$$

$$A_{SL}=\pi R^2 r_f \varphi_s \sin^2\beta$$

And thus the energy required for a liquid drop to get its heterogeneous zone equilibrium state is:

$$G_{CB}=A'_{LV}.\gamma_{LV}-cos\theta\,.\,A'_{SL}.\gamma_{LV}$$

Subsequently Lagrange Multiplying is needed to minimize the equilibrium energy of the drop under a restricted volume V:

$$F=\frac{G}{\gamma_{LV}}+\lambda[V-\pi R^3/_3(1-cos\beta)^2(2+cos\beta)] \qquad 2.12$$

$$\begin{aligned}&\frac{dF}{dR}=0\\&\frac{dF}{d\beta}=0\\&V=\pi R^3/_3(1-cos\beta)^2(2+cos\beta)\end{aligned} \qquad 2.13$$

Eqs. (2.13) can be considered as Eq. (2.12)'s boundary conditions if cosβ is about to be calculated. As a result,

$$cos\beta=cos\theta'_{CB}=r_f\,.\,\varphi_S\,.\,cos\theta+\varphi_S-1 \qquad 2.14$$

This proves that β should spontaneously and finally achieve the CB apparent contact angle θ', as the form of Eq. (2.14) looks exactly the CB same to CB equation; Similarly, for a homogeneous wetting state, the contact areas of liquid–vapor and solid–liquid interfaces are:

$$\begin{aligned}&A'_{LV}=2\pi R^2(1-cos\beta)\\&A'_{SL}=\pi R^2 r\sin^2\beta\end{aligned} \qquad 2.15$$

The energy required to get its homogeneous equilibrium state is:

$$G=A'_{LV}.\gamma_{LV}-cos\theta\,.\,A'_{SL}.\gamma_{LV} \qquad 2.16$$

and consequently we get:

$$cos\beta = cos\theta'_W = rcos\theta \qquad 2.17$$

Thus, in a homogeneous wetting state, the liquid drop will spontaneously form a Wenzel contact angle to minimize the energy. We now have theoretically proved that, from an energetic point of view, the contact angle should form either the Wenzel contact angle θ'W or the CB contact angle θ'CB to minimize its energy state. Substituting β by θ'CB and θ'W, the energy required for a drop in heterogeneous equilibrium and homogeneous equilibrium should be GCB and GW respectively:

$$G_{CB} = \pi R^2 (1 - cos\theta'_{CB})^2 (2 + cos\theta'_{CB}) \gamma_{LV} = \pi^{(1/3)} (3V)^{(2/3)} (1 - cos\theta'_{CB}) (2 + cos\theta'_{CB})^{(1/3)} \gamma_{CB} \qquad 2.18$$

$$G_W = \pi R^2 (1 - cos\theta'_W)^2 (2 + cos\theta'_W) \gamma_{LV} = \pi^{(1/3)} (3V)^{(2/3)} (1 - cos\theta'_W) (2 + cos\theta'_W)^{(1/3)} \gamma_W \qquad 2.19$$

By combining Eqs. (2.18) and (2.19), we finally get:

$$G = \pi^{(1/3)} (3V)^{(2/3)} (1 - cos\theta')^{(2/3)} (2 + cos\theta')^{(1/3)} \gamma_{LV} \qquad 2.20$$

This is consistent with previous research reports. The surface roughness ratio and the fraction of the projected areas are included. Thus, the corresponding equations to both homogeneous and heterogeneous fashions are improved, and Eq. (2.20) can be rear-ranged to a dimensionless form as:

$$\frac{G}{((3V)^{(2/3)} \gamma_{LV})} = \pi^{(1/3)} (1 - cos\theta')^{(2/3)} (2 + cos\theta')^{(1/3)} \qquad 2.21$$

Therefore, it is understood that the energy change from the initial state to the eventual state is a monotonic increasing quantity of θ' (90°<θ'<180°) for a given volume V. As the transition happens, the shape of the drop may change between CB and Wenzel states. The energy difference ΔG between the CB and Wenzel states is:

$$\Delta G = |(G_{CB} - G_W)| \qquad 2.22$$

Also, because of the CAH, the energy change should consider the maximum and minimum values of contact angles. To trigger the transition between the wetting states, the energy added onto the drop must overcome this energy difference. If we define an energy barrier GB between the wetting states, it should include many issues that might not be measurable or controllable, particularly in small scale. Although the transition between those two wetting states is not fully understood yet, this energy barrier GB should be higher than either G_W or G_{CB}. Based on the discussion, it is noted that working on the detail of surface structure is important to precisely prompt the wetting state of a liquid droplet. Therefore, the approaches that have been applied to create and modify the micro- and nanoscaled patterns for superhydrophobic surfaces will be discussed in the following section.

3. Super-hydrophobic surfaces [3][6][7][8][9][10][13][14][15][16][18]

As explained by Wenzel and CB equations, surface roughness and its structure play a very important role in promoting extremely high contact angles. Also, thanks to the findings related to the surface of lotus leaves, people have started the bio-inspired research to understand and design those water repelling surfaces. The effort includes exploring natural surfaces which have complex roughness and significant hydrophobicity. This type of research work is extended in not only plants but also animals at the moment (see the following sections). Also, with the knowledge and technologies being developed, it is possible to artificially produce superhydrophobic surfaces based on biomimetic approaches, which refer to learning from nature. The research work considers both the strategies of designing surface patterns and the methodologies of processing materials. In this section, we will review the recent achievement that has been made to investigate natural and manmade surfaces with super- hydrophobic properties.

3.1. Superhydrophobic surfaces in nature

The lotus flower is considered as a symbol of purity in a few religions. Its leaves can be kept from contamination or pollution without being folded even when the lotus is around with muddy water. This phenomenon illustrates that nature can protect itself from omnipresent dirt and pathogenic organisms. And ideally, if this property is applied to functional surfaces, self-cleaning effect can be prompted in almost any materials in the open air by rain water. As mostly accepted, Barthlott and Neinhuis' early work has started the recent research of superhydrophobic surfaces inspired by nature. Surface roughness has then been recalled to explain the surface's extreme repellence against liquid droplets, as shown in Fig. 12(a). Subsequent and further research has indicated that the plant cuticle is technically a composite material mainly built up by a network of cutin and hydrophobic waxes, where surface structuring arises at different hierarchical levels. The composite or hierarchical surface structure, formed by a combination of two (or even more) layers in different sizes, is built by convex cells and a much smaller superimposed layer of hydrophobic three-dimensional wax tubules, as shown in Fig. 12(b and c) with different magnifications. It has been argued that wetting of such surfaces is minimized, because air is enclosed in the cavities of convex cell sculptures.

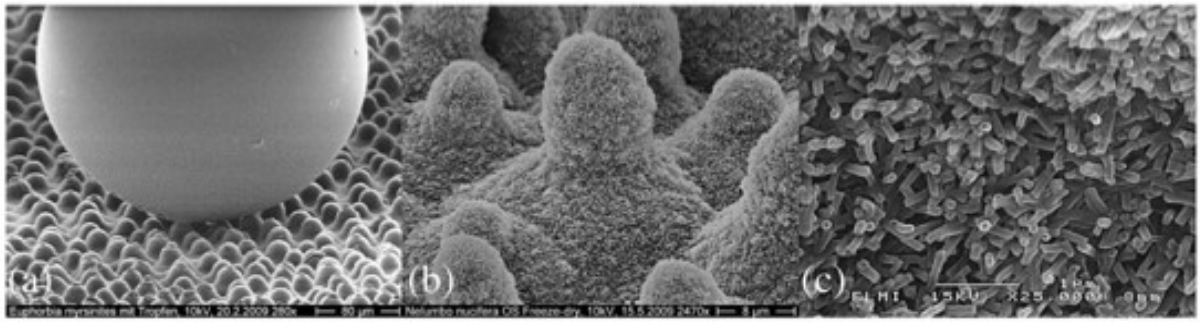

Fig. 12. (a) A glycerol drop on Euphorbia myrsinites, which is a robust specimen and well suited to show the surface's repellence against the liquid droplet. Scale bar = 80 μm. (b) The upper side surface of the lotus leaf without the shrinkage artifact. Scale bar = 8 μm. (c) The wax tubules from the upper side of the lotus leaf. Scale bar = 1 μm. [3]

Along with the lotus leaves, there are other natural superhydrophobic surfaces in the plant kingdom. For example, taro (Colocasia esculenta) leaves have been used to demonstrate the self-cleaning effect in the original paper. It has been observed that the elliptic protrusions with an average diameter of about 10 μm form the microstructure on the taro leaf, and the nanoscaled pins form the hierarchical structure with the microstructure, which is however similar to the lotus leaf, as shown in Fig. 13(a–c). Our SEM images of taro leaves shown in Fig. 13(b' and c') have avoided the shrinkage by using critical-point-drying techniques. They are more conformal to the real structure on the taro leaves. Similarly, India canna (Canna generalis bailey) leaves and the rice leaves (whatever the kind of rice) have been reported to be superhydrophobic and have binary structures (micro- and nanostructures) on the surface, as shown in Fig. 13[(d–f) and (g–i)]. These multi-layers have positive importance to make up the wax crystals. The dimensions of wax structures range from a few nanometers to several micrometers, and are responsible for the maintenance of wettability. Lotus leaves, India canna leaves and taro leaves form tubule-like and platelet-like wax crystals, which are the ‘most prominent types’ of wax structures. Also, the arrangement of surface structure can have great influence on wettability of solid materials. It is pointed out that the water droplets can roll off a rice leaf easily along the direction of the arrow, shown in Fig. 13(g), at a sliding angle of 4°, but move much harder along the perpendicular direction at a sliding angle of 12°. Thus, it is clear that the anisotropic arrangement of the protrusions influences a rice leaf very much. However, due to the homogeneous arrangement of surface protrusions, the sliding angle of a lotus leaf can be down to below 2°. Also, as recently realized, a colocasia leaf shows superhydrophobic characteristics but has different structure from the lotus leaf . The surface structure of a colocasia leaf has similar bumps to lotus, but the bumps are separated by the surrounding ridges. The bump and ridge both contribute to the hydrophobic nature of colocasia since they might create air pockets between the water droplet and the surface. At this point, it is necessary to emphasize that the surface cuticle and its waxes are important to surface wettability by folding the cuticle or by forming three-dimensional wax crystals on the plant surface.

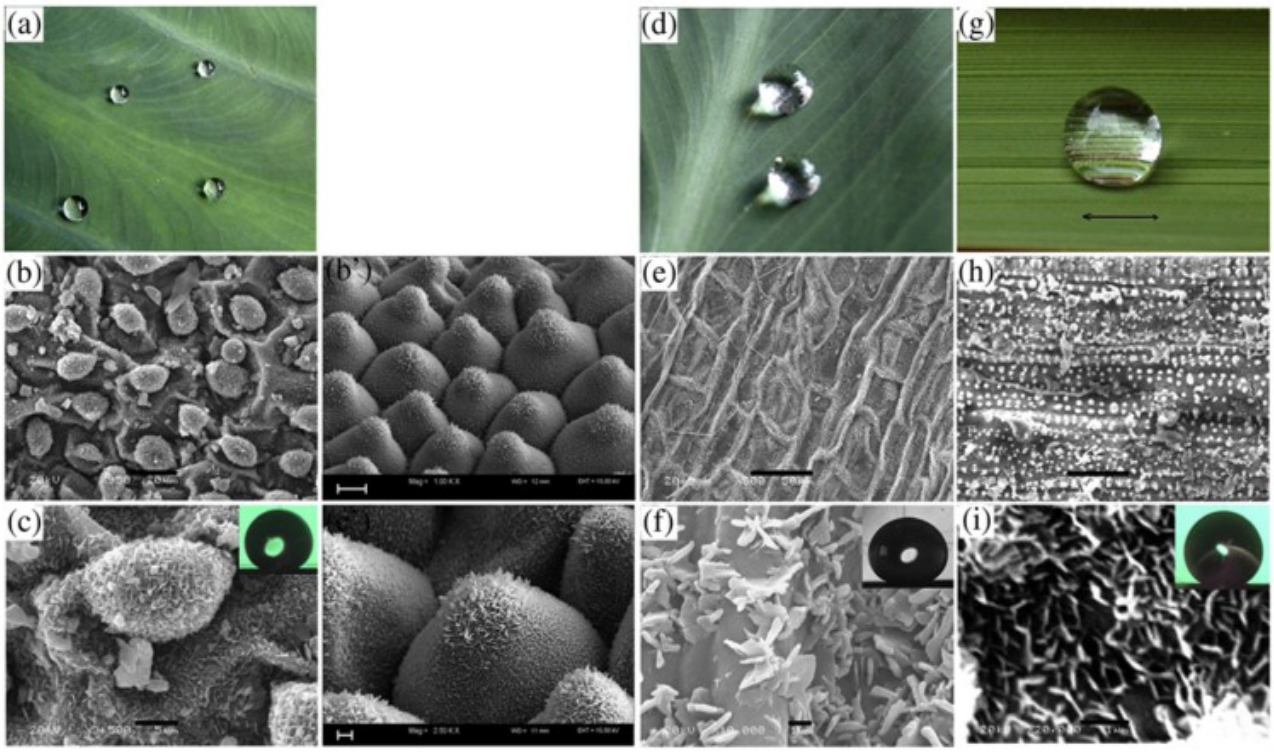

Fig. 13. (a) A few water droplets on a taro leaf. (b) and (c) show the SEM images of a taro leaf with different magni fications. The inset of (c) is a water droplet on a taro leaf, with a contact angle of 159 ± 2°. The scale bars of (b) and (c) are 20 μm and 5 μm, respectively. (b') and (c') correspond to our SEM images using critical-point-drying techniques on observing taro leaves when shrinkage is avoided. The scale bars of (b') and (c') are 10 μm and 2 μm, respectively. (d) Water droplets floating on an India canna leaf. (e) and (f) show the SEM images of an India canna leaf with different magni fications. The inset of (f) is a water droplet on an India canna leaf, with a contact angle of 165±2°. The scale bars of (e) and (f) are 50 μm and 1 μm, respectively. (g) A water droplet floating on a rice leaf (Oryza sativa L.). (h) and (i) show the SEM images of the rice leaf with different magnifications. The inset of (i) is a water droplet on a rice leaf with a contact angle of 157 ± 2°. The scale bars of (h) and (i) are 50 μm and 1 μm, respectively. [3]

Thus, it has been brought into consideration that some natural surfaces with hierarchical structure and roughness can produce significant superhydrophobicity, not only from plants but also animals. It has been revealed that the leg of a water strider [Fig. 14(a)] has numerous oriented needle-shaped setae [Fig. 14(b)] with their diameters ranging from 3 μm down to several hundred nanometers. Many elaborate nanoscaled grooves are noticeable on each microseta [Fig. 14(c)], forming a hierarchical structure, which origins the superhydrophobicity of the water strider's legs with assistance of the hydrophobic secreted wax. On the other hand, the scales on the wing surfaces of some butterflies have regularly arranged edges which are overlapping like roof tiles, as shown in Fig. 14(d–f). The lengths and widths of each individual scales are roughly ranged 50–150 μm and 35–70 μm, respectively, while the primary distance between the middle points on the long axis of two adjacent scales is within 100 μm. However, not every hierarchical surface in nature has been found with superhydrophobic behaviors. A gecko has hundreds of thousands of keratinous hairs or setae on its foot, as shown in Fig. 14(g–i); each seta is around 30–130 μm long and contains hundreds of submicron spatulae, forming hierarchical morphologies. This type of hierarchical structure does not necessarily have superhydrophobic properties, although it is still employable as a model for comparison. This indicates again the importance of the pattern of surface structures in wettability. But the investigation into superhydrophobicity by means of biomimetics has not been

discouraged. Phenomenally, Byun et al. selected 10 orders and 24 species of insects to characterize the functions of natural structures by focusing on both lower and upper surfaces of the wings. They argued that the hierarchical architectures which included micro- and nanoscaled layers on the upper surfaces of insect wings (Fig. 15) promoted hydrophobicity, thereby enabling water droplets to roll off the wings and remove the dirt particles.

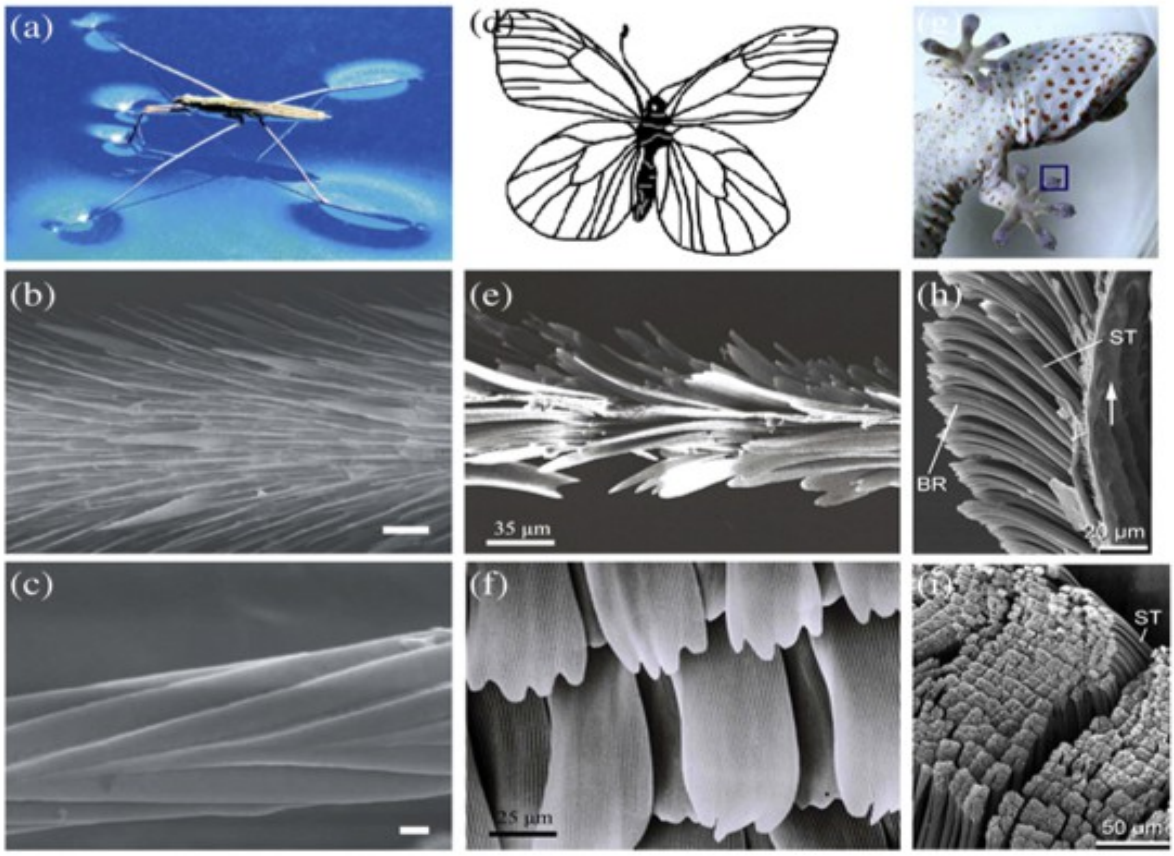

Fig. 14. Natural hierarchical surfaces. (a) A water strider (Gerris remigis) standing on the water surface. Scanning electron microscope (SEM) images of a strider leg showing numerous oriented spindly microsetae (b) and the fine nanogrooved structures on a seta (c). Scale bars: 20 μm (b), and 200 nm (c); (d): schematic of a butterfly (Pontia daplidice). SEM images show the transection (e) of the butterfly wing surface and its flat arranging (f); (g): A gecko (Gekko gecko) with emphasis on its toe. A toe of gecko contains hundreds of thousands of setae and each seta contains hundreds of spatulae. (h) and (i): SEM images of rows of setae at different magnifications. ST: seta; BR: branch. [3]

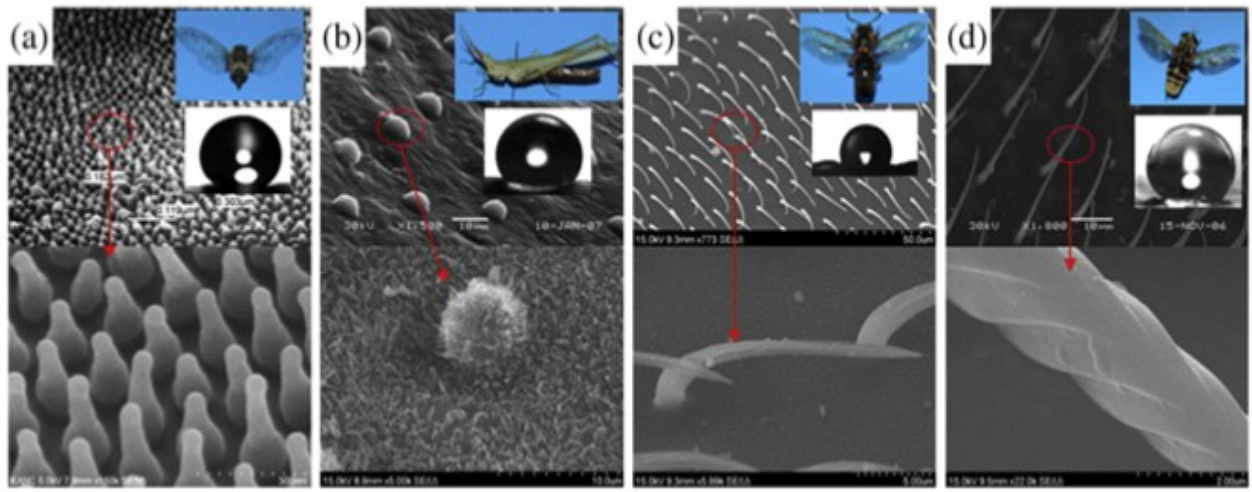

Fig. 15. SEM images of the micro/nano structures and measured contact angles on upper wing surfaces of insects. (a) Homoptera Meimuna opalifera (Walker), showing contact angle of 165°; (b) Orthoptera Acrida cinerea cinerea (Thunberg), showing contact angle of 151°; (c) Hymenoptera Vespa dybowskii (Andre), showing contact angle 126°; (d) Diptera Tabanus chrysurus (Loew), showing contact angle of 156°. Vespa dybowskii, Acrida cinerea cinerea, and Tabanus chrysurus show micro- and nanoscaled hierarchical structures. Al- though Homoptera Meimuna opalifera (Walker) does not have such hierarchical structures, the wing shows superhydrophobicity due to its very fine nanoscaled structure. [3]

It is already becoming vivid from the discussions mentioned previously that the mechanisms of individual superhydrophobic surfaces are not necessarily the same with each other in every aspect. Different from the lotus effect, the so-called petal effect describes the phenomenon that a water droplet on the petal surface of a red rose (rosea Rehd) forms a spherical shape, but does not roll off even when the petal is turned upside down, as shown in Fig. 16. The diverse design in surface microstructure on rose petal results in different dynamic wetting from lotus leaves. When a small water drop wets the petal surface, the liquid film impregnates the textured regime. How- ever, the liquid only wets the grooves between the projected pillars, leaving the “plateaus” dry, which forms the Cassie impregnating state, as shown in Fig. 17. For the petal surfaces, the dimensions of hierarchical micro- and nanostructures both are found larger than those related to the lotus leaf. In the Cassie impregnating wetting regime, water droplets enter into the “large” grooves of the petal but not into the “small” ones. This indicates why small water drops sealed in micropapillae would be clinched to the petal's surface, showing a high CAH even if the surface was turned upside down. Thus, the mechanisms for different natural superhydrophobic surfaces and their wetting states might seem vague to follow. However, the common characteristic of superhydrophobic surfaces rests on the congenially periodical structures that are hierarchically organized in micro- and nanoscale. In particular, the natural models that are related or similar to lotus effect have been mostly used due to their prominent features.

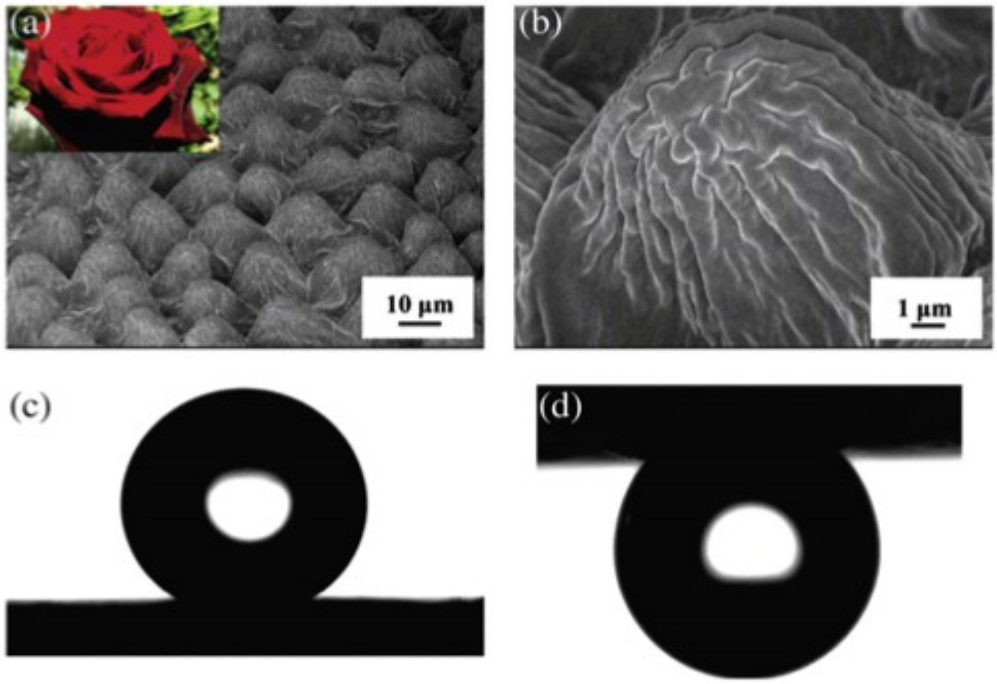

Fig. 16. SEM images (a, b) of the surface of a red rose petal, showing a periodic array of micropapillae and nanofolds on each papillae top. (c) A water droplet on the petal's surface, indicating its superhydrophobicity with a contact angle of 152.4°. (d) Profile of a water droplet on the petal surface when turned upside down. [3]

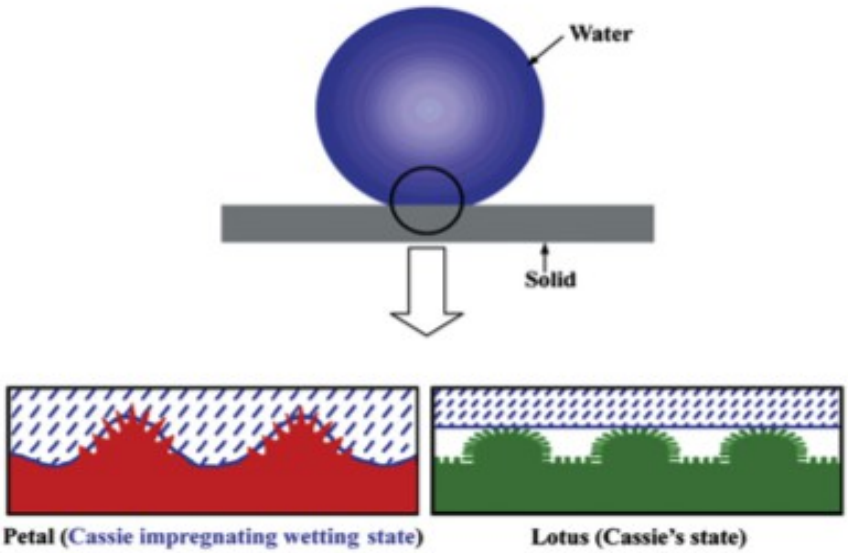

Fig. 17. Schematic illustrations of a drop of water in contact with the petal of a red rose (the Cassie impregnating wetting state) and a lotus leaf (the Cassie's state). [3]

3.2. Artificial superhydrophobic surfaces

It is noticeable that many of those natural superhydrophobic surfaces discussed above have intense roughness and complex structure in micro- and nanoscales. Some symbolic surfaces have been utilized as the primary models for researchers to mimic superhydrophobicity. For example, a combination of poly(vinyl chloride) (PVC) and ethanol has been used to form superhydrophobic films, as shown in Fig. 18. The formed PVC surfaces become rougher with the increase of ethanol content (under 50%) in the PVC solution, and more pores and nanocomposites are formed. These superhydrophobic surfaces form lotus-leaf-like structures consisting of many nanoparticles with the sizes ranging from 100 nm to 300 nm. Also, as pointed out previously, typical superhydrophobic surfaces discovered in the nature have shown multiscaled roughness consisting of nanometer sized flakes on top of micrometer sized protrusions. This type of morphology for superhydrophobic surfaces can be achieved using lithographic methods, template-based techniques, plasma treatment, self-assembly and self-organization, chemical deposition, layer-by-layer (LBL) deposition, colloidal assembly, phase separation, and electrospinning. Most of these methods are in accordance with the theoretical and natural models discussed in previous sections, and one strategy commonly used to invoke superhydrophobicity for many processes is producing rough surfaces with hierarchical structure and low surface energy. The following section will discuss those methods as well as the manmade superhydrophobic surfaces.

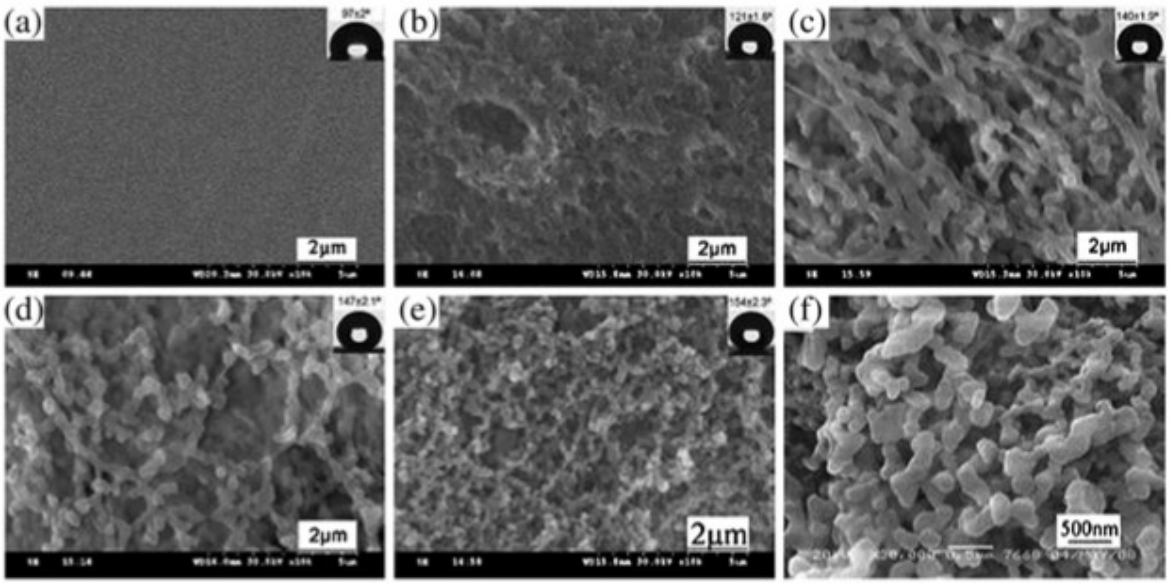

Fig. 18. SEM images of PVC surfaces obtained with the different ethanol content in the PVC solution: (a) 0% (v/v); (b) 16.7% (v/v); (c) 37.5% (v/v); (d) 44.4% (v/v); (e) 50% (v/v); (f) is the higher magnification SEM image of (e). Insets are the water contact angles on the as-prepared PVC surfaces. [3]

3.3. Methods to prepare superhydrophobic surfaces

The imprinting techniques to produce superhydrophobic surfaces usually involve lithography, templating, and plasma treatment. The common feature of lithography and templating is embodied that they usually need a master piece and a replica substrate, while a plasma treatment is somehow related to surface etching. Those technologies are not necessarily independent on each other, but to the contrary, can be used as a combination to realize a superhydrophobic surface. Theoretically, a surface processed by lithography can be treated further by plasma etching to achieve complex roughness with multilayers and then used as a featured template to produce replicas. However, the main principle is to make the process as uncomplicated as possible for the creation of a superhydrophobic surface. We herein will investigate the technical principles and characteristics of those methods, respectively.

3.3.1. Lithography

The lithographic process is a well-established technique and its sub- techniques used in making superhydrophobic surfaces include optical lithography (photolithography), soft lithography nanoimprint lithography, electron beam lithography, X-ray lithography, and colloidal lithography. On a general level, this sort of method prepares superhydrophobic surfaces by copying the information from a master, which can be either rigid or soft, and then transferring it to a replica in an opposite form. It should be noted that these branches of lithography are not rigidly or definitely distinguished. For instance, the superhydrophobic surfaces obtained by using nanolithography also utilized the optical technique in processing the master piece. The colloidal lithography and optical lithography may involve nanolithography as well. And this applies to the soft lithography too.

Conventional lithography normally uses a flat plate as the master surface. Now the lithography is often referred to as photolithography, which transfers the entire geometric pattern from an optical mask to a thin film of photoresist sensitive to light (mostly ultraviolet), for its powerful effect and common usage. For the soft lithography, the key elements include elastomeric stamps, molds, and/or mask, which are utilized to generate patterns and structures in micro- and nanoscaled size. And recently, this type of lithography has been advanced rapidly. The whole process can also involve self-assembling as well as the replica molding. The photo reactive film is not essential for the soft lithography to create the micro- and nanostructures, although it can still be adopted. The electron beam lithography uses focused electron beams rather than scattered light to create the surface patterns, and the mask is not necessarily used any more. X-ray beam lithography also needs mask and resist, which means it is similar to photolithography in terms of working procedures, while the main difference rests on the source of radiation. X-ray radiation is selectively absorbed by the mask and thus a pattern can be formed. The so-called colloidal lithography for making superhydrophobic surfaces is relatively new and still under development. One of the applications has used a monolayer of silica colloidal spheres as the mask, which is followed by reactive ion etching (RIE) to fabricate superhydrophobic surfaces.

The optical lithography is a frequently used technique, and it is always coupled with other lithographic methods to create surface patterns. Micro- and nanoscaled hierarchical structures were fabricated using UV-assisted capillary force lithography, which was based on the sequential application of engraved polymer molds followed by a surface treatment. The fabrication procedures

of the ‘dual- scale’ structure were to generate microstructures first by using microscaled poly(urethane acrylate) (PUA) or poly(dimethyl siloxane) (PDMS) mold and then nanostructures on the top by using nanoscaled PUA mold, respectively. Partial ultraviolet (UV) curing was used in the first step to form micropillars (microposts), while complete UV curing was used in the second step to form nanopillars. To induce surface hydrophobicity, the fabricated hierarchical surface was treated with a trichloro (1H,1H,2H,2H-perfluorooctyl) silane in vapor phase. Fig. 19 shows the SEM images of representative hierarchical structures. The substrates made of poly(ethylene terephthalate) (PET), silicon or glass could be equally used during the process.

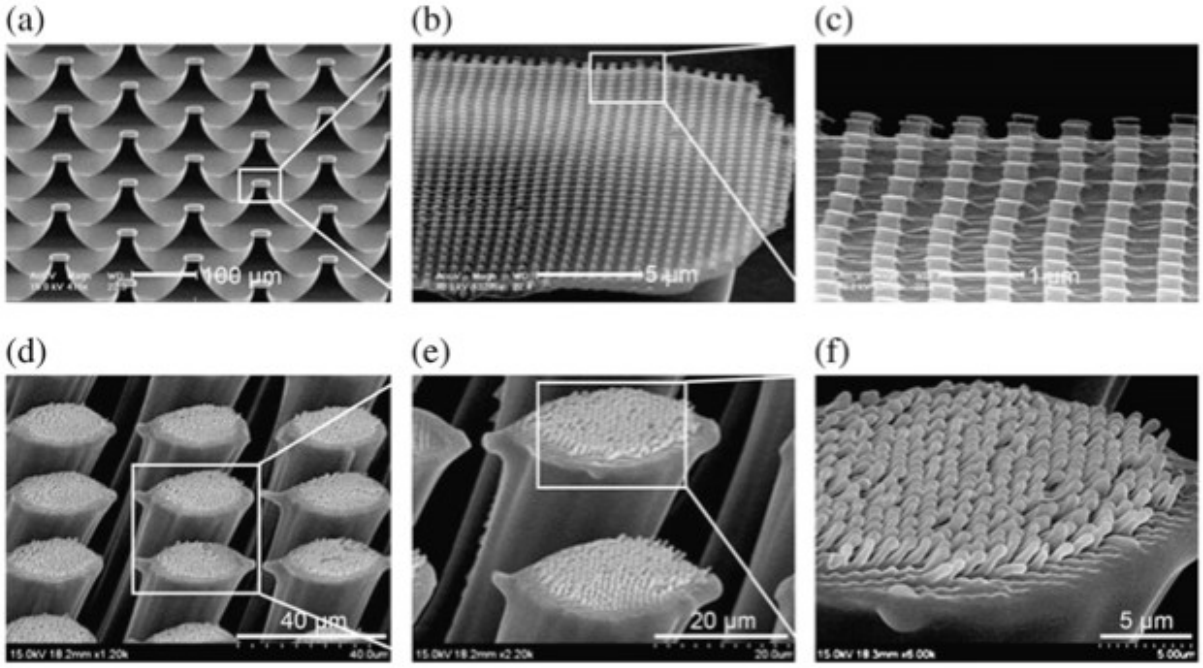

Fig. 19. Tilted SEM images of typical dual-scale hierarchical structures. (a–c) For microstructures, 30 µm posts of 40 µm in spacing and 50 µm in height were used. Magnified images in (b and c) show well-defined 400 nm dots (spacing of 800 nm, height of 500 nm) formed on the microposts. (d–f) For microstructures, high aspect ratio micropillars (diameter of 20 µm, height of 100 µm and spacing of 20 µm) were used. Magnified images in (e and f) show the formation of 400 nm pillars (spacing of 400 nm, height of 2.5 µm) on top of the as- formed micropillars. [3]

As a recently developed combination of nanoprocessing and lithography, the nanoimprint lithography (NIL) can create patterns more precisely down to nanoscale. Lee and Kwon's team conducted a series of experiments to fabricate superhydrophobic surfaces by using nanoimprint lithography. They designed a set of UV- NIL equipment and fabricated photopolymer replicas. The whole replication was performed in a clean environment and composed of two processing steps, making nickel mold by electroforming [Fig. 20(a)] and making replication by polymer casting [Fig. 20(b)] or UV-NIL [Fig. 20(c)]. The nickel mold was directly patterned upon a lotus leaf, and therefore the topographic feature and contact angle of produced replicas from polymer casting and UV-NIL both showed close similarity to the original lotus leaf.

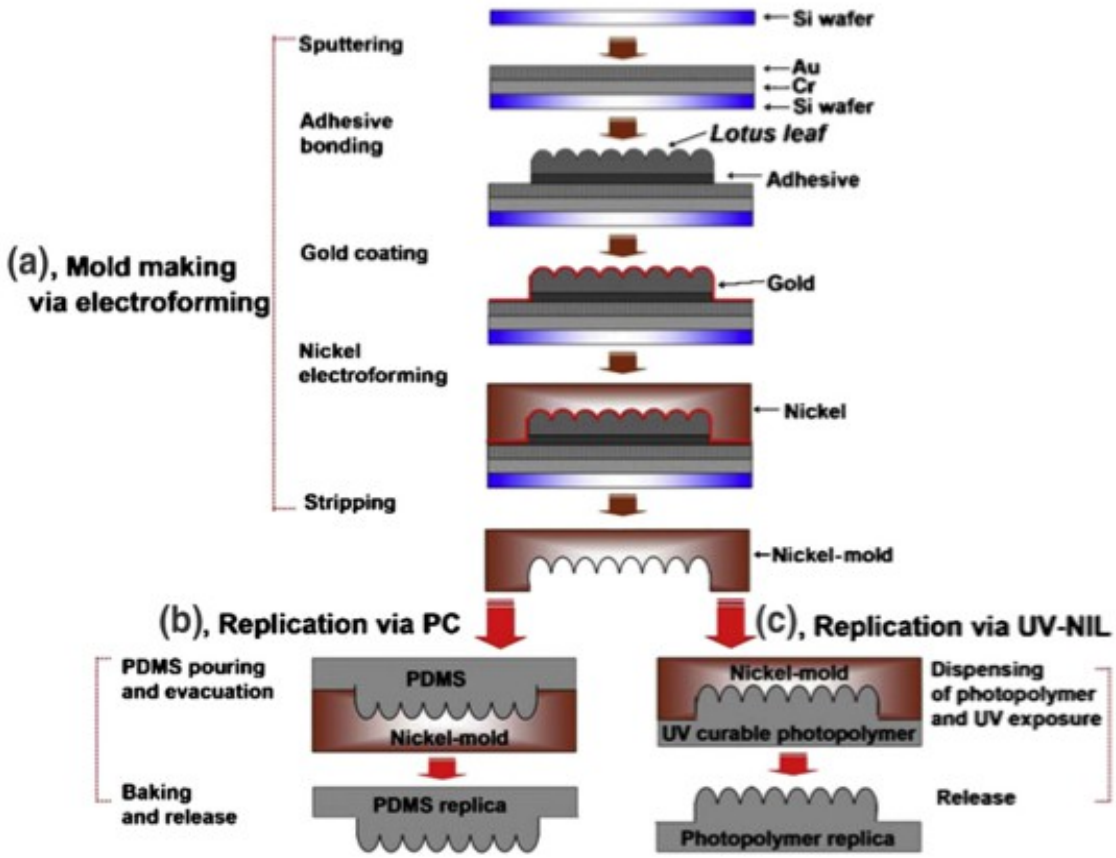

Fig. 20. Schematic representation of the fabrication process of superhydrophobic surfaces composed of two steps. Nickel mold making (a), followed by replication using polymer casting (b) or UV-NIL (c). [3]

The nanoimprint lithography discussed above was based on a combination of nano-replication and optical lithography. The photo- polymer performed as a photoresist and there was no photo mask used during the lithographic process. This decreased the number of processing steps and still secured the superhydrophobicity caused by optics-aided NIL. It was an example that nano-techniques and lithography were involved in the same process of making superhydrophobic surfaces. In modern times, the subdivisions of lithography are not completely isolated with each other anymore. It is possible to combine the advantages of those lithographic techniques to make superhydrophobic surfaces.

3.3.2. *Templating*

Template-based methods are another imprint-related way to pre- pare superhydrophobic surfaces. To develop the superhydrophobic surface pattern, templating can be involved with lithography. Thus it is plausible that the templates can be fabricated by using lithography. Also, templating is used to assist other methods preparing superhydrophobic surfaces. The original prototypes of the templates can be filter paper, insect wings, reptile skins, and plant leaves. From a chemical and morphological point of view, the template can even be molecules and polymers.

Generally speaking, the templating process includes preparing a featured template master,

then molding the replica and finally re- moving the templates. One typical process was the fabrication of superhydrophobic surfaces by mimicking the hairy structure of gecko's feet. The gecko-mimetic nanopillar structures of hard-PDMS were fabricated by using nanoporous anodic aluminum oxide (AAO) membranes as templates. The aluminum plate was initially anodized to remove electrically oxidized aluminum layer, and further anodized to produce the nanoporous AAO template with cylindrical pore channels. Afterwards, h-PDMS precursors were spin- coated on the fabricated AAO template. The sample was cured after conformal contact with the vinyl-terminated glass, and the molded h-PDMS film was peeled off from the AAO template. The general process is shown in Fig. 21. The length of cylindrical pore channels of AAO templates was controlled by varying anodization time at the second anodization step, and was optimized to make the super-hydrophobic h-PDMS surface, as shown in Fig. 22.

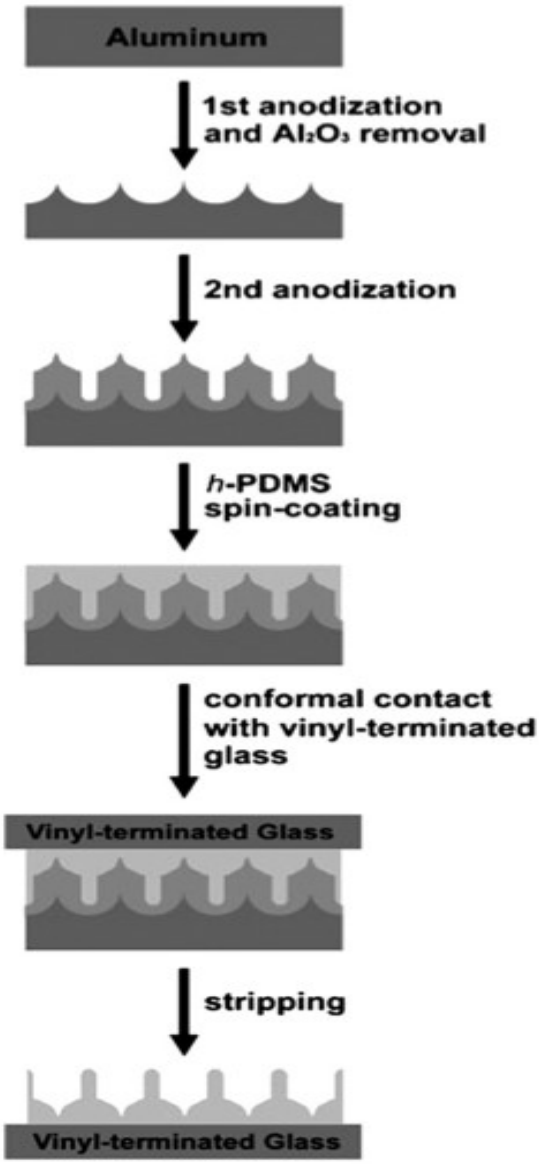

Fig. 21. Procedure for the fabrication of gecko-mimetic h-PDMS nanopillar films on the vinyl-terminated glass substrate. [3]

Thus, it is not arduous to notice that the templating-based methods are effective in creating regular surface patterns, even though the structures need to be relatively complex. A high-quality template can be repeatedly used to make a large number of samples. However, when it comes to micro- and nanoscaled structures, the operators are required to be essentially careful to avoid damaging both the samples and the templates. Also, the templating methods might not be fit to produce irregular surface patterns with excessively complex structure, due to the peeling off procedure.

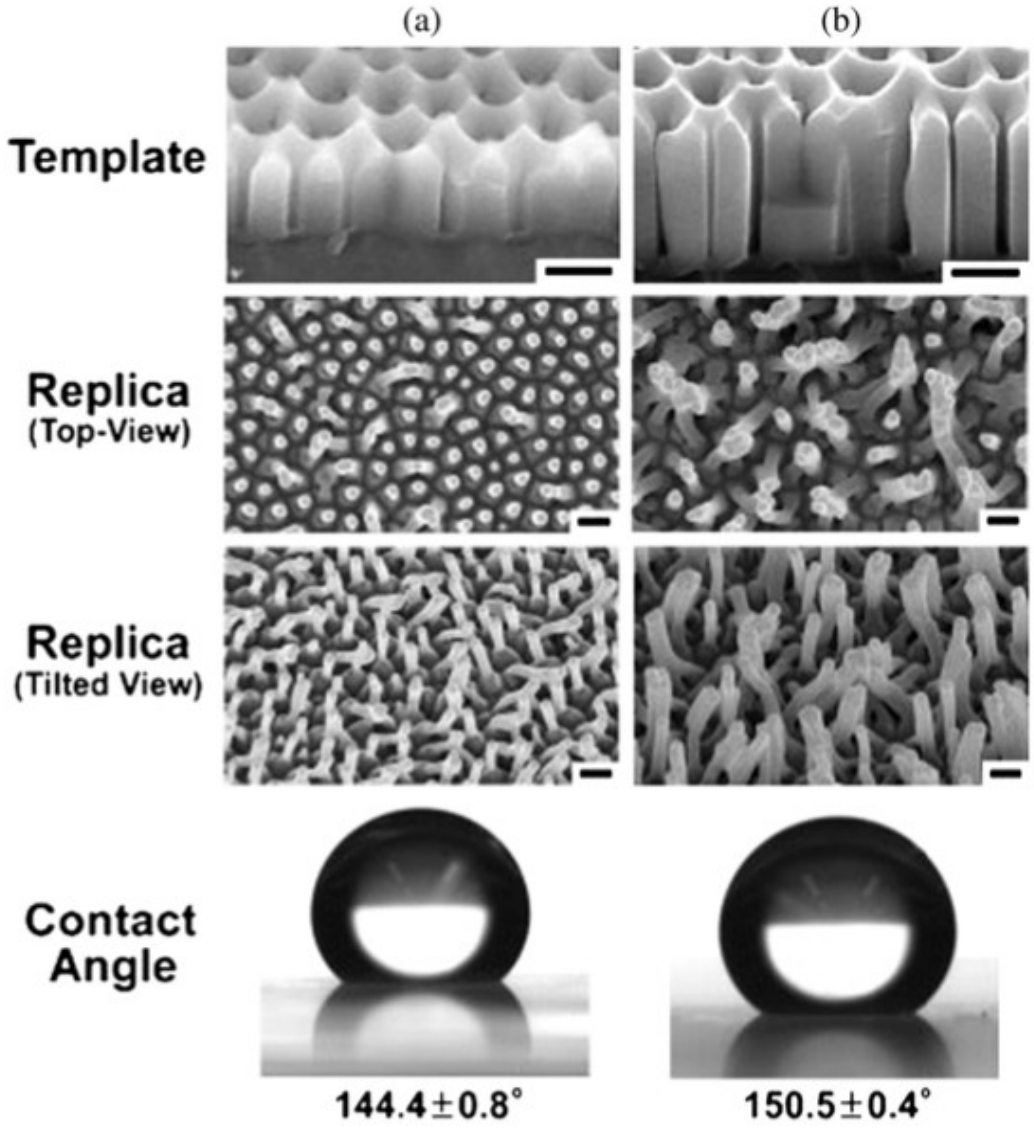

Fig. 22. FE-SEM images of AAO templates anodized at the second anodization for 10 min (a) and 20 min (b), and their h-PDMS replicas. The bottom shows a static water contact angle on each replica surface. The scale bar is 500 nm. The h-PDMS nanopillars stretch out from the hexagon-like arrangements of hemispherical convexes. The nanopillar structure is con firmed by the tilted view of FE-SEM. [3]

3.3.3. *Plasma treatment (etching)*

In quite a few cases, the surface pattern has been formed by the plasma treatment after lithography or templating methods. However, the plasma treatment can also be used before lithography or templating, and sometimes the plasma treatment and lithography can even alternate with each other during the surface processing. Moreover, as mentioned earlier, the plasma treatment is somehow connected to etching techniques for preparing superhydrophobic surfaces. Kim et al. fabricated superhydrophobic surfaces which had sharp tips at nanoscale by using deep reactive ion etching (DRIE), which was a developed form of the RIE (Reactive-ion etching). A typical RIE process for prompting superhydrophobicity uses chemically reactive ions from the plasma which is generated by an electromagnetic field. It creates surface patterns by removing material from the wafer surface, while the DRIE gives 'deep' features to the surfaces. Kwon et al. formed microscaled textures on a silicon surface using deep reactive etching and nanoscaled textures on the microscaled textures using XeF2 etching, as shown in Fig. 23. The XeF_2 etching could provide uniform roughness at nanoscale on the surface, but the etching time should be carefully controlled to avoid over-etching. The etched surface was coated with a heptadecafluoro-1,1,2,2-tetrahydrodecyl trichlorosilane (HDFS) self-assembled monolayer (SAM) to prompt large intrinsic contact angles and therefore the CB superhydrophobicity. In the droplet bouncing test, the droplet that landed on the surface with double-layered roughness would always find the CB state energetically favorable, and it could bounce back from the surface (Fig. 24), showing great superhydrophobicity.

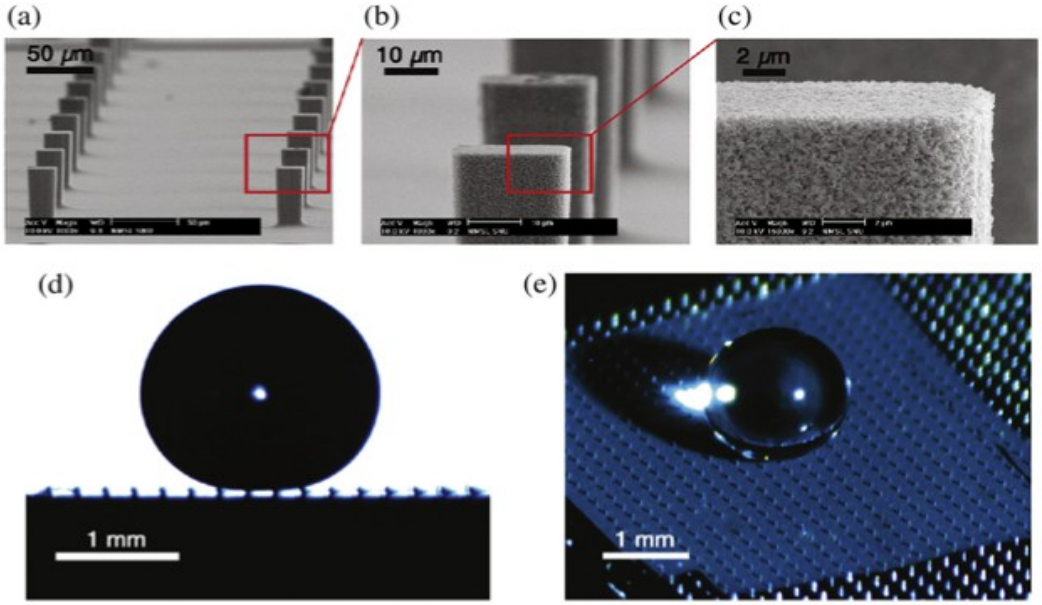

Fig. 23. Droplet on the fabricated nano-microroughened hierarchical surface. (a–c) Nanoscaled roughness etched by XeF2 gas that conformally covers the microscale array of pillars fabricated through deep reactive etching. (d–e) Droplet sitting on the double roughness with the value of the pillar spacing to width ratio at 7.5, supported by only several pillars. The contact angle at this state is 173° (+6,–3). [3]

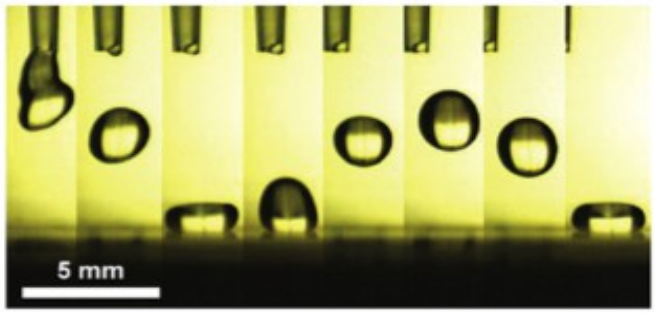

Fig. 24. Droplet (liquid volume=10μL) bouncing on the double-roughness surface. This figure was a sequential shot of the droplet bouncing on the superhydrophobic surface. A high-speed camera (MotionPro HS-4) was used to take the video image at a rate of 5000 frames per second. [3]

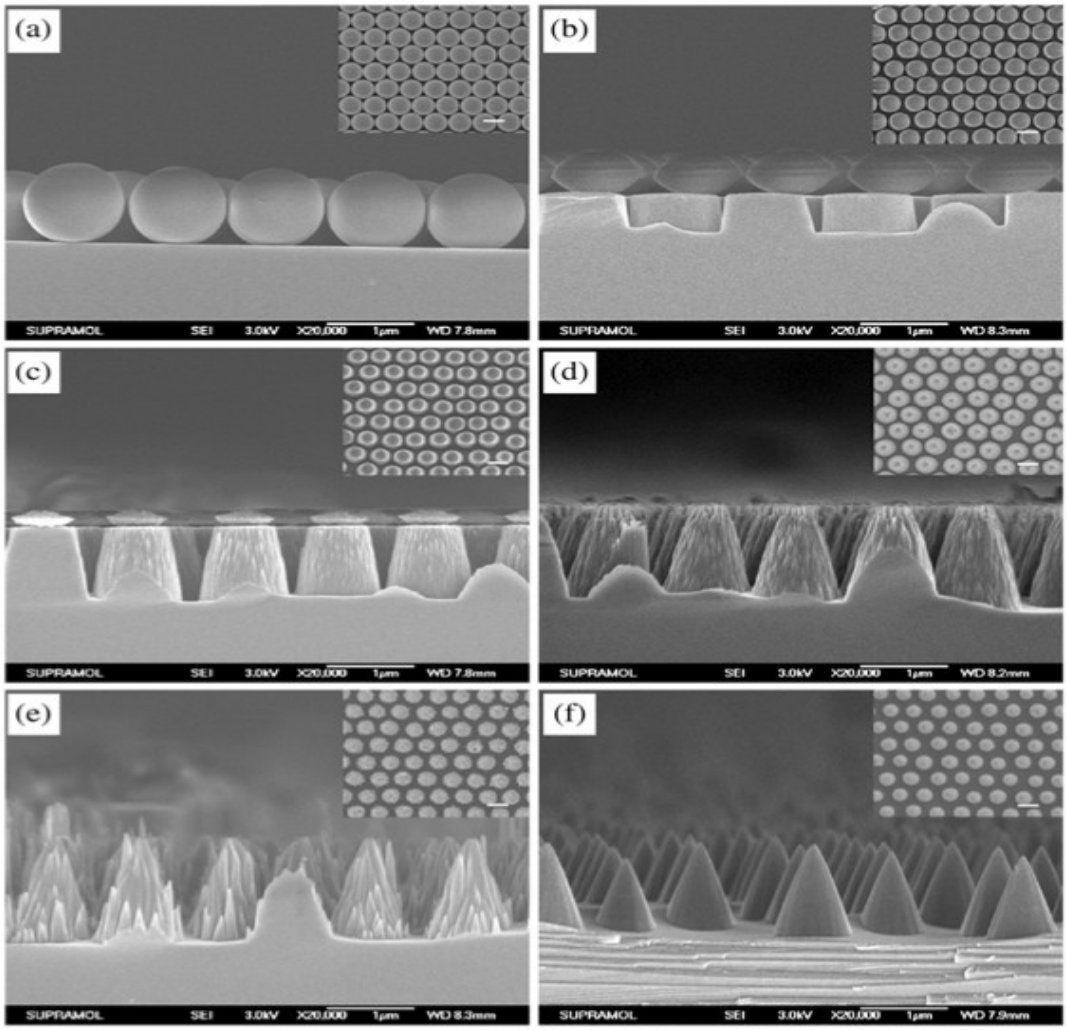

Fig. 25. Cross sectional SEM images of morphologies of silicon microstructure arrays obtained after etching for 0 s (a), 70 s (b), 140 s (c), 175 s (d), 210 s (e), and 300 s (f). Insets are the top-view SEM images of the relevant ordered structure arrays. The average diameter of silica sphere used as mask is 1115 nm. The structure height from b–f is approximately 575, 1075, 1351, 1431, and 1086 nm, respectively. Scale bars are 1 μm. [3]

CF_4 RIE was used to fabricate polymeric superhydrophobic surfaces which were three-dimensionally featured by prism holographic lithography in advance . The adhesion force for water on superhydrophobic surfaces originated from gecko surfaces was normalized to be 0.01 N/cm2, which was claimed as the highest yet reported for an artificial superhydrophobic surface at that moment. A superhydrophobic hierarchical surface (Fig. 26) consisting of nanopillars super- posed on microbumps was prepared by using a combination of photolithography and RIE . The static contact angle of a water droplet could reach up to 160° on the artificial surface. Argon plasma treatment on a superhydrophobic biodegradable polyester substrate was used to control the wettability and to produce films with gradient of wettability. A high-density microwave plasma system was used as a dry etching technique on PDMS to prepare superhydrophobic surfaces. Other plasma treatments that were involved to create superhydrophobic surfaces also include plasma polymerization, plasma electrospray, plasma-enhanced chemical vapor deposition or its combination with plasma etching , and plasma immersion ion implantation (PIII) . From the discussion above, it can be seen that plasma treatment is applicable to the production of regular superhydrophobic surfaces on a variety of substrates and materials. It can either be adopted as the only technique or coupled with other techniques as a combination to create surface patterns. The source gasses are required to react well with the mate- rials, otherwise the surface patterns would not be realized properly. Therefore, the reaction conditions have to be controlled strictly, which means it requires a lot of physical effort to produce surface pat- terns with extremely complex roughness on large scaled surfaces via plasma treatment.

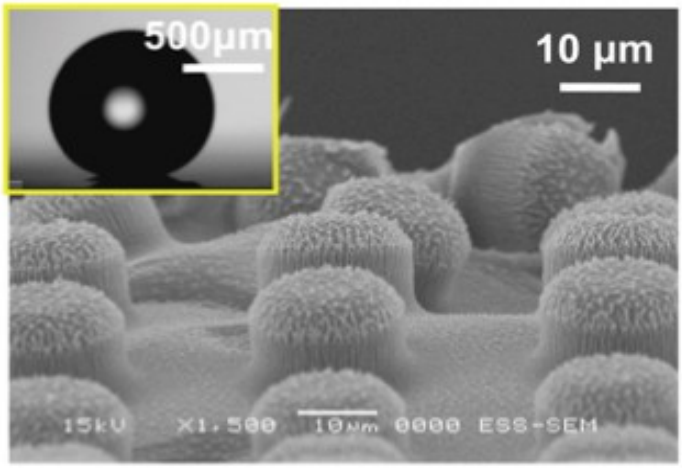

Fig. 26. SEM photo of a hierarchical surface made by lithography and RIE. The inset photo shows a water droplet with a static contact angle of 160° on this artificial surface. [3]

3.3.4. *Chemical deposition*

Superhydrophobic surfaces can also be produced by chemically depositing a thin film on the selected substrates. Typical chemical deposition methods include chemical vapor deposition (CVD), electro- chemical deposition, and LBL deposition. A CVD process normally refers to exposing the selected substrate to a gaseous precursor to deposit the desired film or powder, and chemical reactions are involved during this process. The electrochemical deposition process however can be used to deposit films of solid metal or its oxide onto electrically conductive substrates. LBL deposition is another versatile way to pre- pare superhydrophobic surfaces with multilayered films. In the following section, we will review several typical cases of preparing superhydrophobic surfaces based on chemically depositing methods.

CVD-based surface treatment

The plasma-enhanced chemical vapor deposition (PECVD) has recently received more attention and already been used to fabricate superhydrophobic surfaces. Phenomenally, superhydrophobic surfaces with supported Ag/TiO_2 core-shell nanofibers were prepared at low temperature by PECVD [145]. The fibers were formed by an inner nanocrystalline silver thread covered by a TiO_2 overlayer. Water contact angles depended on both the width of the fibers and their surface concentrations, and a maximum contact angle close to 180° was reached. As materials for reference, TiO2 was simultaneous- ly deposited on flat Si substrates. Fig. 27 shows a series of planar view SEM images corresponding to Ag/TiO2 and TiO2 surfaces, respectively. The water contact angles' varying with the width of the fibers was attributed to Wenzel's theory that surface roughness would have an obvious effect on contact angles. When irradiated with UV light, the superhydrophobic surfaces became superhydrophilic. The decrease rate of contact angles depended on both the crystalline state of the ti- tania and the size of the individual TiO_2 domains. This was one example that a superhydrophobic surface could transform reversibly into a superhydrophilic one triggered by light irradiation.

Multiwalled carbon nanotubes (CNTs) with considerable mechanical strength were fabricated by using catalyst-assisted chemical vapor deposition (CCVD). The multiwalled CNT composites were deposited on microstructured Si surface with pillars using soft lithography. And the flat epoxy resin was deposited using a spraying method. After spraying the CNTs on the surfaces, the CNT composite structures (Fig. 28) were then annealed in order to improve the mechanical properties. For comparison's sake, hierarchical structures at nanoscale were also created by depositing self-assembled lotus waxes. After introducing CNT nanostructure on top of the micropatterned Si replica, the hierarchical structure with CNTs showed a static contact angle of 170° and a CAH of 2°. On the other hand, the highest static contact angle of 173° and lowest CAH of 1° were found on hierarchical structure with lotus wax. This meant that the CNT hierarchical structure and lotus wax hierarchical structure had more or less similar superhydrophobicity. But the waterfall/jet tests showed that CNT composite structures had a good stability of wetting properties not only from long-term exposure to water but also high water pressure. The nanostructure with lotus wax, however, could be damaged by water with high pressure, resulting in the loss of superhydrophobicity.

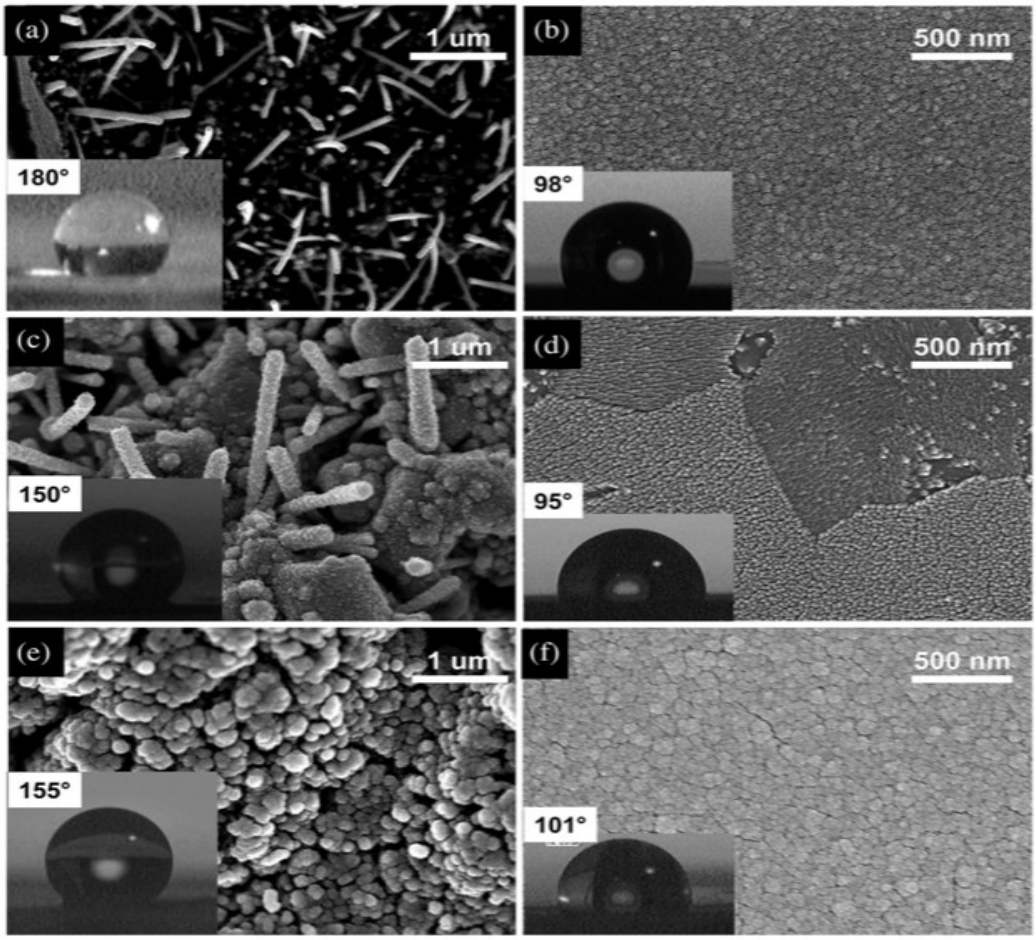

Fig. 27. SEM micrographs of the Ag/TiO2 composites (left) and TiO2 (right) surfaces prepared by PECVD on respectively a silver membrane and a flat Si substrate. (a) and (b), de- position at 403 K, fibers are now formed. (c) and (d), deposition at 523 K. (e) and (f), deposition at 298 K, no fibers are formed. The insets show the images of the water droplets that formed on the surfaces of different samples during water contact angle measurements. [3]

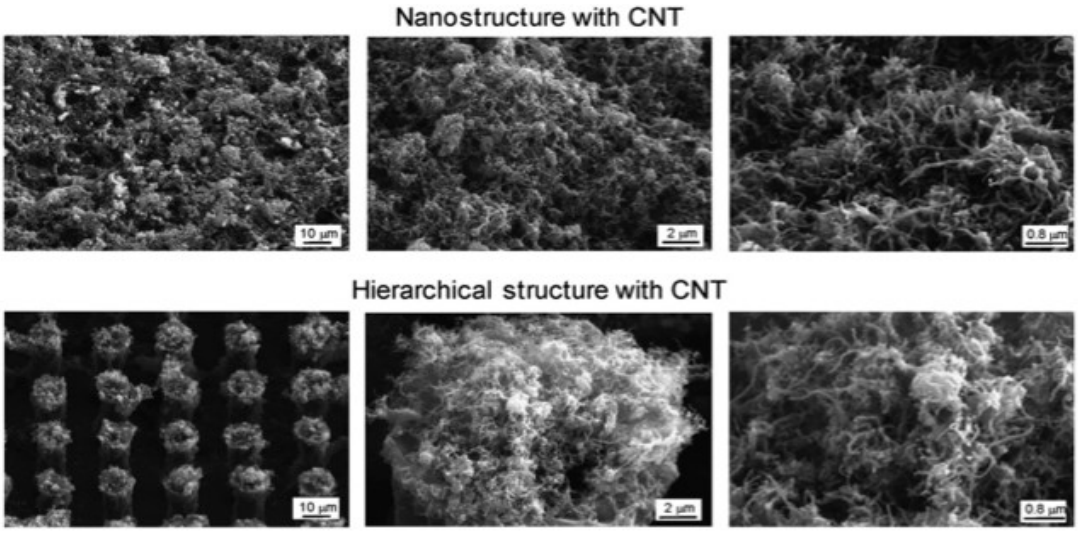

Fig. 28. SEM micrographs taken at 45° tilt angle, show three magnifications of nano- and hierarchical structures fabricated with CNTs after 3 h at 120 °C. [3]

Besides, similar approaches in the production of the surface patterns with complex roughness were reported a lot. Superhydrophobic CNT forests were obtained using PECVD. Superhydrophobic properties were induced on paper surfaces via a combination of selective etching by an oxygen plasma and deposition of a fluorocarbon film from pentafluoroethane (PFE) via PECVD. Microwave-plasma enhanced chemical vapor deposition (MPECVD) from trimethyl-methoxysilane was carried out to produce superhydrophobic micropatterns. A superhydrophobic film with high hardness and transparency was created through MPECVD. PECVD of ribbon- like fluorocarbon films from modulated C2F4 was used to induce nano- structured superhydrophobic surfaces. As a matter of fact, the CVD-based methods were often used to produce superhydrophobic surfaces based on their feasibility in maintaining and enhancing the mechanical strength of the formed structure. These methods are able to create complex surface structures at nanoscale, which means extreme wettability can thus be induced. However, due to the relatively extensive operation procedures, it is difficult to control precisely the detail at each individual spot of the surface.

Layer-by-layer (LBL) deposition

The fundamental principle of the LBL deposition rests on changing the charge of a substrate, and this allows the construction of multilayered films. The process normally involves the assembling of layers with spontaneous adsorptions, while the size of the substrate can be in a wide range. It does not necessarily need to prepare the master for replication like imprinting methods or provide a particular environmental chamber like plasma treatment and CVD. Therefore, this type of method is relatively facile and potentially economical. To achieve the surface roughness for a superhydrophobic state, nano- particles are often added into the deposition. This, however, will put more perplexities for the precise control of surface patterns.

Cohen and Rubner's team performed a series of research work using the LBL method to produce functional surfaces.Typically, they utilized LBL processing schemes to create transparent superhydrophobic films containing SiO2 nanoparticles with various sizes. The deposition process consisted of immersing the substrates repetitively into different aqueous solutions to form three main parts of the film, which were adhesion, body and top layers, as shown in Fig. 29. Briefly, the LBL procedures were firstly dipping the substrate into the cationic solution and then dipping the substrate into the anionic solution with proper assistant operation. Poly(allylamine hydrochloride) (PAH) was used to create the cationic solution and poly(sodium 4-styrenesulfonate) (SPS) to create the anionic solution for the adhesion layers, which could enhance the binding of the polymer–nano-particle system. PAH was used to create the cationic solution and two differently sized silica nanoparticles (50 and 20 nm) were respectively used to create the anionic solution for the body layers. The cationic solution used for the top layers was PAH and the anionic solution was distilled water solution containing 20-nm silica particles. Advancing contact angles up to 160° with the CAH as small as 10° were obtained on the optimized multilayered thin film, and the optical transmission levels were preserved above 90%.

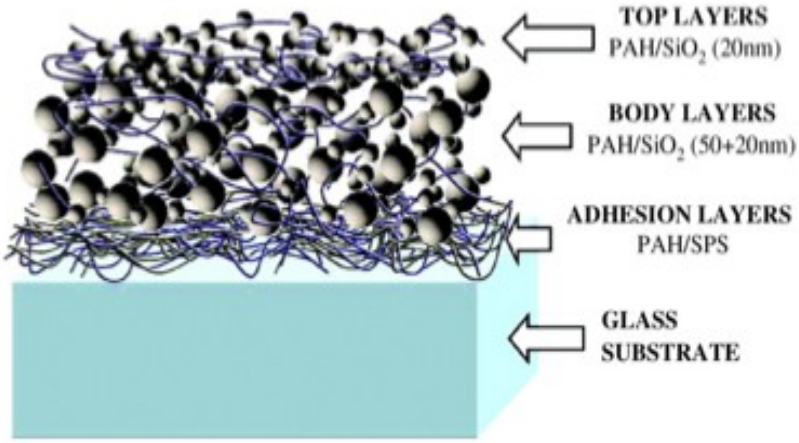

Fig. 29. Simplified schematic of the multilayer film showing the three main assembly blocks. [3]

On the other hand, Zhai's group fabricated a switchable superhydrophobic/superhydrophilic surface by using similar LBL techniques. Uniform and conformal multilayered films of PAH and silica nanoparticles were built upon the surface with a precise control over film thickness and roughness. The surface was further functionalized with poly(N-isopropylacryamide) (PNIPAAm), which was a thermoresponsive polymer exhibiting low critical solution temperature in an aqueous solution, and a low surface energy material- (1H,1H,2H,2H-perfluorooctyl) silane (perfluorosilane). The combination of surface roughness and chemical composition created switchable superhydrophobic/superhydrophilic surfaces, which could be potentially applied as hydrophobic valves into microfluidic channels. Jindasuwan et al. reported another example of producing superhydrophobic surfaces by mimicking the structure features of the lotus leaf. In their work, superhydrophobic films were dip- coated onto glass substrates using a LBL deposition of polyelectrolyte. Afterwards, SiO_2 nanoparticles were deposited to modify the surface roughness, and finally a semifluorinated silane was applied to lower down the surface energy.

Colloidal assembling and aggregation

The assembling or aggregation of colloidal particles can be used to assist chemical deposition, sol–gel process, and lithography to make the micro- or nanostructures for superhydrophobic surfaces. The colloidal assembly itself is the process based on forming assemblies of monodispersed particles through chemical bonding or van der Waals forces. If the sizes of the assembling particles are well controlled and have different scales, multilayered roughness can be obtained [161]. The multilayer is normally formed by immersing the substrate into the solution of particles or spin-coating the solution onto the substrate. For instance, Min et al. Synthesized monodispersed silica particles (~ 70 nm) which could be spin-coated over a large area. Fig. 30(a) shows a typical transmission electron microscope (TEM) image of the as-made nanoparticles. The diameter of the spheres was calculated to be 72 ± 6 nm using the image analysis software (Scion Image). Fig. 30(b) shows a top- view SEM image of the multilayered crystal structure prepared by spin-coating at

10,000 rpm for 10 min. Fig. 30(c) shows the spin-coated colloidal crystal which was “non-close-packed”. The spheres of the top layer filled in the triangularly arranged crevices made by the spheres of the second layer. On this occasion, the spheres were separately distributed in the same single layer. The thickness of the colloidal crystals could be controlled by adjusting speed and time of spin-coating.

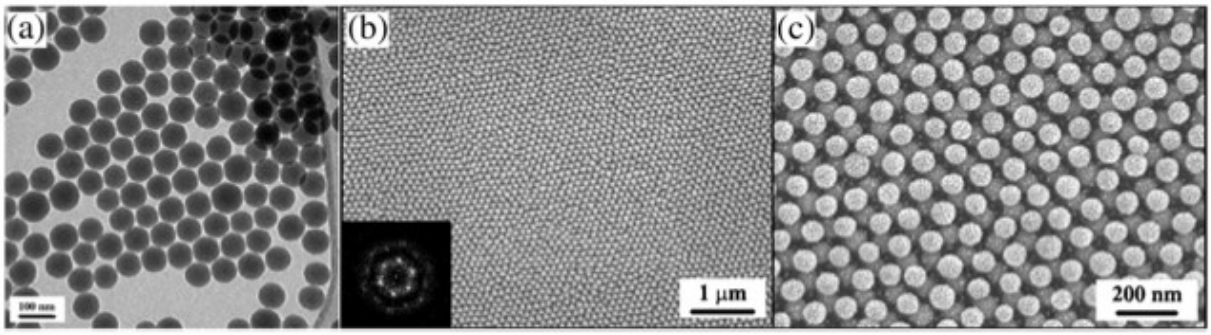

Fig. 30. (a) TEM image of synthesized silica nanoparticles. (b) SEM image of a multilayer colloidal crystal prepared by spin-coating. (c) Higher-magnification SEM image of the sample in (b). [3]

The case of achieving superhydrophobic states discussed right above actually had much to do with multilayered colloidal crystals based on the self-assembly techniques. Directed by internal interactions or forces among the colloidal particles, a self-assembly method forms the patterns on superhydrophobic surfaces. The use of self-assembled monolayers (SAMs) requires that a stable monolayer film, which has specific and favorable interaction with the selected solid substrate, should be formed. As a result, the formed film must remain attached firmly onto the substrate because of the interaction, even after the substrate is taken off from the solution which originates the SAMs. And the multilayered structure can be created by repeatedly conducting the SAMs.

The process based on colloidal assembly and aggregation is very effective in modifying surface energy and promoting surface roughness (structure) to create extreme surface wettability. The chemical reactions which are often accompanied with the process can produce fairly considerable connection between the colloidal aggregates and the substrates, and thus maintain the durability of the formed structure. It does not necessarily need complicated production equipment or operation procedures.

Therefore, the colloidal assembling and aggregation is relatively more economical and efficient than traditional imprinting methods and even some CVD methods. It has the potential to produce both sufficient surface coverage and precise order of structure. Nonetheless, the prima- ry underlying task to widely apply the process is resting on grafting the desired properties into the colloidal solutions as well as keeping the system stable and uniform.

Sol–gel process

The sol–gel methods have been utilized to create superhydrophobic surfaces in accordance

with Wenzel or Cassie–Baxter's theories since the very early stage of mimicking lotus leaves' surface structure. It involves a chemical solution deposition, during which the chemical solution or sol is utilized as a precursor on the selected substrate to form a gel-like network. Material of low surface energy and micro- or nanoparticles can be added into the network to create superhydrophobic surfaces. For its compatibility with glass, this type of method is particularly favored in creating transparent and superhydrophobic films on glass surfaces. To provide generally regular surface pattern to the network, extra control over the process like spin-coating is always needed.

One of the recently reported examples was based on the use of a eutectic liquid in a sol–gel process to form silica films with optical transparency and superhydrophobicity. The involved eutectic liquid (composite of urea and choline chloride) had an extremely low vapor pressure relative to a common sol–gel solvent (for example of ethanol). The eutectic liquid remained in the film throughout the process under ambient conditions, which contributed to the control over film thickness and surface roughness. Porous silica thin films with asperities were formed after gelation in the presence of a base catalyst, which was composed of tetraethoxysilane, ethanol, HCl and H2O, and subsequent extraction of the eutectic liquid. Proper fluoroalkylsilane (PFOS) treatment imparted the superhydrophobicity with a contact angle of 170° and a hysteresis of 2–3°. To further pro- mote transparency of the superhydrophobic films, the sol solution was diluted with ethanol and then spin-coated on substrates. Fig. 31 shows SEM images of surfaces spin-coated with sol dilutions with the ratios of ethanol against sol being 1:1, 3:1, 5:1 and 7:1, respectively. The surface roughness and film thickness of spin-coated films decreased continuously with dilution, while the superhydrophobicity of the surface was maintained at a certain level. As a result, the transparency of the films was improved.

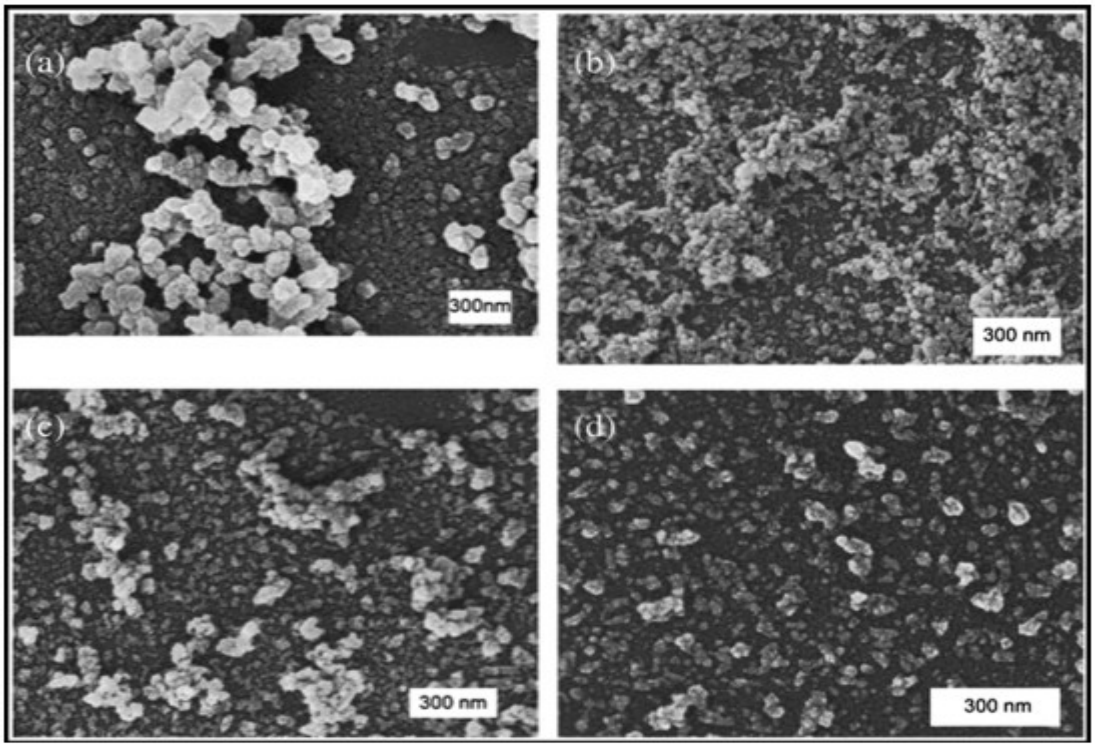

Fig. 31. SEM surface images of dilute-sol-coated glass slides. The ratios of ethanol:sol are 1:1(a), 3:1(b), 5:1(c), and 7:1(d).[3]

Electrospinning and electrospraying

Strictly speaking, electrospraying and electrospinning are two similar but different techniques which can both be used to fabricate micro- or nanostructures. But when it comes down to fabricating superhydrophobic surfaces, those two methods are very easy to be garbled. Electrospinning is a simple and versatile method to produce continuous polymer fibers in micro- and nanoscale. It is an effective way to create superhydrophobic surfaces by prompting the roughness. To form uniform fibers, the molecular weight of the polymer and the concentration of the solution should be properly prepared. On the other hand, electrospraying is not necessarily restricted in fibers only. The polymer films deposited by electrospraying can range from spheres to fibers. But on a general level, it is considered that fibers are produced during electrospinning process, and beads are produced during electrospraying process.

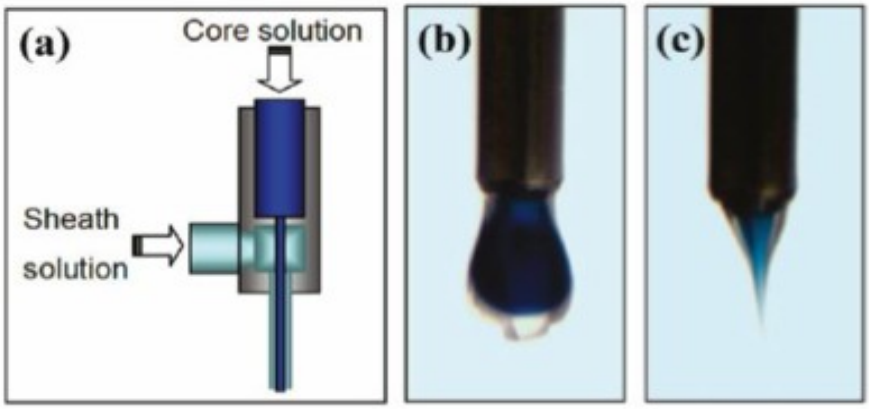

Fig. 32. Coaxial electrospinning operation. (a) Diagram of the coaxial nozzle; (b) core- sheath droplet without bias; (c) Taylor cone and coaxial jet formation at 12.5 kV. [3]

Electrospinning is a versatile technique for producing micro/nanofibers from many kinds of polymers. In a laboratory environment, electrospinning requires a high- power supply, a conducting substrate, and a syringe pump. The electrospinning process is initiated by a high electric field between the syringe (containing viscous polymer solution) and the conducting substrate. Because of the high electrical potential, a charged liquid jet is ejected from the tip of a distorted droplet, the so-called Taylor cone. The liquid jet experiences whipping and bending instabilities within a sufficient distance to evaporate its solvent thoroughly and, consequently, becomes a solid nonwoven micro/ nanofiber membrane on the substrate. Oriented polymer nanofibers can also be produced by modifying the ground electrode geometry and/or rotating it and by using a microfluidic chip to deliver the solution to the ejection tip. Electrospinning has been used to make membranes with rough surfaces, followed by the deposition of hydrophobic material, and to produce superhydrophobic membranes in a single-step process. In the former case, rough membranes are electrospun first and then coated with hydrophobic material by deposition techniques such as CVD and the layer-by-layer technique. In the latter case, the electrospun fiber itself can provide superhydrophobicity by electrospinning a blend of polymer and hydrophobic material and/or by introducing secondary structures such as pores and beads. Nanoparticles have also been introduced to increase roughness and to produce superhydrophobicity.

Phase separation

Colloidal aggregation methods can also involve phase separation, which separates the solid phase from a metastable mixture of sub- stances by changing surrounding conditions, for example of temperature and pressure, to fabricate patterned surface structures. The surface structure and roughness formed through phase separation can be macroscopic, microscopic, and even nanoscopic . Due to its working mechanism, this method is often related to the sol–gel process for creating controllable surface patterns. However, phase separation, is not necessarily utilized by sol–gel methods only, but also can assist other techniques, including plasma treatment, electrospinning, and self-aggregation, to make superhydrophobic surfaces. Note that the phase separation processes involved in these various methods are more or less connected to colloidal polymerization.

TiO2 and ZnO induced wettability

TiO2 is known as an efficient and stable photocatalyst . TiO2 surfaces with proper treatment can be light (UV irradiation) induced into an amphiphilic (both hydrophilic and oleophilic) state, and the water contact angle on the induced surfaces can be close to 0°. However, it is also found that, for surfaces coated with thin films which mainly consist of TiO2 nanoparticles, the water contact angle goes up and gets restored in a dark place. Moreover, the effect of adding other nanoparticles into the TiO2 thin films can change the surface wettability. For instance, SiO2 nanoparticles are found constructively helpful to maintain the superhydrophilicity relatively long after UV irradiation. Also, adding TiO2 nanoparticles into other films can do the job as well.

It has been argued that TiO2 coated surfaces can well lead to self- cleaning effect , but the mechanism is quite different from the self-cleaning effect corresponding to the lotus effect. Upon UV illumination on TiO2, electron-hole pairs are generated and they produce hydroxyl and superoxide radicals which can oxidize and decompose organic compounds absorbed on the TiO2 coated surfaces. For those surfaces mainly functioned by light-induced TiO2, the self-cleaning effect can be enhanced by sunlight and rainfall, as shown in Fig. 33. The light-induced characteristic of TiO2 provides a novel way to prepare surfaces with superhydrophilic and superhydrophobic properties both. It should be noted that the superhydrophilicity of TiO2 coated surfaces rests not only on the intrinsic property of TiO2, of which the mechanism has been proposed to be the reconstruction of surface hydroxyl groups under UV illumination, but also on the surface morphology. As stated previously, surface roughness can be utilized to increase the contact angle on hydrophobic surfaces, but decrease the contact angle on hydrophilic surfaces.

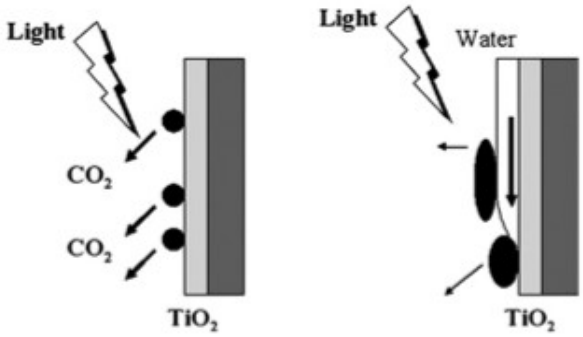

Fig. 33. Schematic diagram of the decontamination process occurred on the superhydrophilic self-cleaning surface. [3]

It has also been found that, from the comparative studies, the con- version reactions of photo-induced wettability on the ZnO thin films follow a similar mechanism with TiO2, which means superhydrophilicity can also be light-induced on surfaces mainly functionalized by ZnO. Thus it is feasible to fabricate superhydrophobic/superhydrophilic surfaces by taking advantage of either ZnO or TiO2. Actually the light-induced mechanism corresponding to the wettability of ZnO coatings lies in the electron–hole pairs as well. The electron and hole generated by ZnO upon UV illumination react with the lattice oxygen and then form oxygen vacancies . Water molecules on the ZnO surfaces may coordinate into the oxygen vacancy sites, leading to adsorption of the water molecules on the surface; the induced superhydrophilicity can go back to superhydrophobicity if the surface is placed in the dark. Therefore, the wettability is convertible from being superhydrophilic to being superhydrophobic on ZnO surfaces, and this point is useful to control wetting states of surfaces.

4. Functions for biomimetic superhydrophobic surfaces [3][10][11][18][22]

Although the biomimetic superhydrophobic surfaces have been fabricated by various methods as referred above, more and more scientists have transferred their focus on their functions and applications from the fabrications in recent years, especially in the last four years, since many other important functions besides superhydrophobicity, such as surface mechanics, surface electrics, anti-icing, and super-oil-repellent, must be considered for their practical applications in industry ultimately.

4.1. Anti-icing

Ice buildup on solid materials, especially on overhead transmission and distribution lines in some cold regions, may lead to mechanical line failure or insulator flashovers. As a matter of fact, the ice storm that hit East China in the winter 2007 caused billions of dollars in damage to the power networks, also resulting in the serious traffic disruption in some main high-ways and railway lines. It is still a challenge to construct solid surfaces with anti- icing properties. In past years, the biomimetic superhydrophobic surfaces have shown their speculated capability to reduce accumulation of snow and ice and to even completely prevent formation of ice on solid surfaces .

The adhesion strength of artificially created glaze ice (similar to accreted in nature) on rough fluoropolymer-based superhydrophobic surface with different CA and wetting hysteresis, showing the ice adhesion strength on rough hydrophobic surface has no correlation with values of water CA, but good correlation with wetting hysteresis, which is believed to be related to the ice-solid contact area. Gao et al. prepared an anti-icing superhydrophobic coating by means of using nano- particle–polymer composites, first demonstrating the anti-icing capability of superhydrophobic surfaces, which are able to prevent ice formation upon impact of supercooled water both in laboratory conditions and in natural environments. They found that the anti- icing capability of these composites depends not only on their superhydrophobicity but also on the size of the particles exposed on the surface.

In fact, icing of supercooled water on superhydrophobic surfaces is a complex phenomenon, which can be affected by a lot of factors, such as temperature, the real contact area, surface chemistry, surface roughness, and hydrodynamic conditions. Accordingly, studying the anti-icing of superhydrophobic surfaces is just beginning. Further research is needed to understand the effect of these factors on icing.

Deicing:

➔ Aircraft Deicing: **$5.000 per aircraft**

Figure : Aircraft Deicing

➔ Power Lines : **One winter storm -$5 billion**

Figure : Power Lines Deicing

4.2. Super oil-repellent

Although enormous efforts focused on making superhydrophobic surfaces now, surfaces with super-oil-repellent and low adhesion, that resist wetting to liquids with much lower surface tension,such as decane or octane are extremely rare. The case is changed in recent four years. Several different textured surfaces showing CAs greater than 160°, even with octane. They explained this observed super oil-repellency by considering local surface curvature as the third parameter that affects both the apparent contact angle and hysteresis on any surface. Meanwhile they demonstrated that it is possible to engineer textured surface that repel a range of polar and nonpolar liquid through appropriate combination of local surface curvature and suitable alteration of the solid surface energy, shown in Fig. 34. Liu et al. employed a high field anodization to achieve super oil-repellency towards a broad range of liquid, such as water, hexadecane, silicone oil and crude oil. Steckl et al. investigated coaxial electrospinning to produce core-sheath-structured nano/microfibers, which are superhydrophobic and super oil-repellent. Chemical adsorption technique is also employed to make the superhydrophobic and oleophobic surfaces.
All these results above can provide a new idea in wettability of solid materials and enlarge their applications in industry. Which allow us to develop some kinds of surfaces that can support both an extremely robust interface and high contact angles with any liquid.

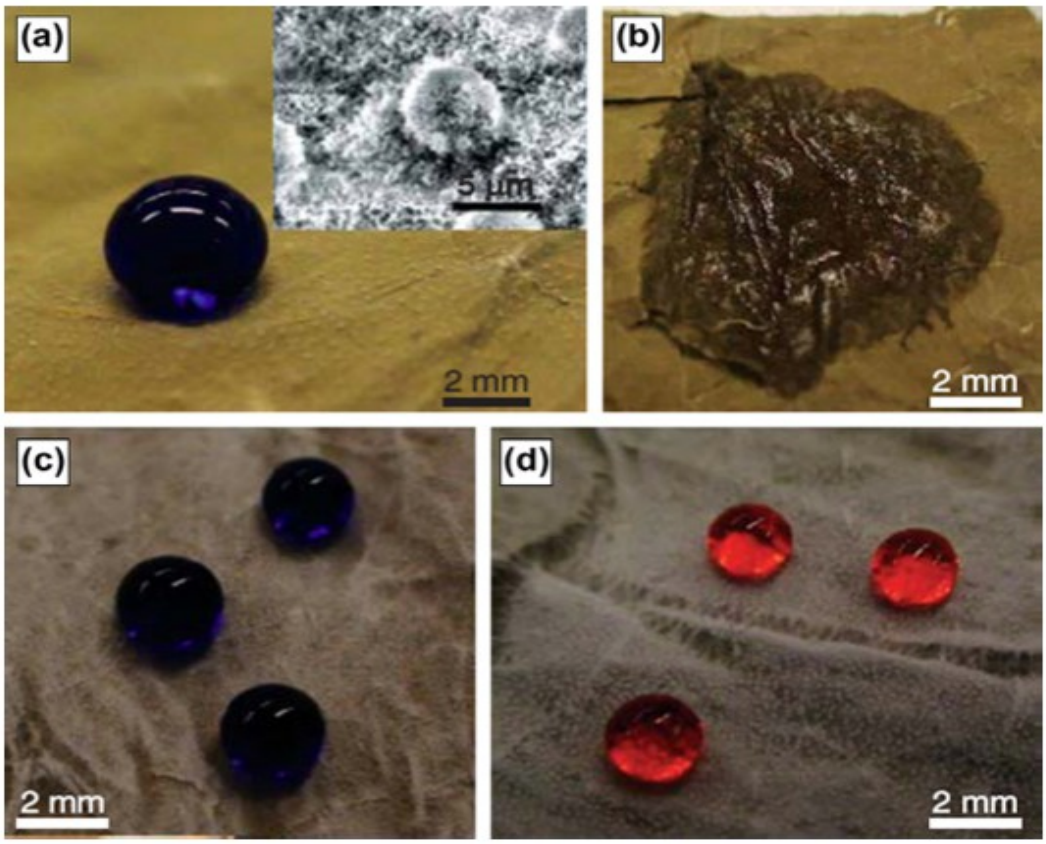

Fig. 34. (a) Droplet of water (colored with methylene blue) on a lotus leaf surface. (b) Wetted surface of the lotus leaf after contact with a droplet of hexadecane. (c) and (d) Droplets of (c) water (colored with methylene blue) and (d) hexadecane (colored with Oil Red O) on a lotus leaf surface covered with electrospun fibers of poly(methyl methacrylate) (PMMA) 44 wt. % fluoroPOSS (fluorinated polyhedral oligomeric silsesquioxane) [6]

4.3. Self-cleaning and transparency

Similar to lotus leaf, the most apparent advantage of biomimetic superhydrophobic surfaces is self-cleaning. Up to now, most of biomimetic superhydrophobic surfaces can not be applied into industry due to their weak surface mechanical properties, which are mainly depended surface structures. At the same time, it is delightful for us that more and more scientists paid their attentions on the applications of biomimetic superhydrophobic surfaces in recent years, especially in the last four years. For instance, Seeger et al. reported the results of extensive studies on the environmental durability of a transparent superhydrophobic silicon nanofilament coating, showing that the coating retains its superhydrophobic and anti-reflective properties for at least one year of outdoor weathering (Fig. 35a and b). Zuburtikudis et al. investigated the effect of artificially induced roughness on the water repellency of mineral substrates coated with protective polymer films, which processes superhydrophobicity after the introduction of nanoparticles into the coatings. This result indicates that the nanoscale binary composition film scheme, which is characterized by its simplicity and low cost, is a suitable candidate for the water protection of stone-based monuments on large scale.

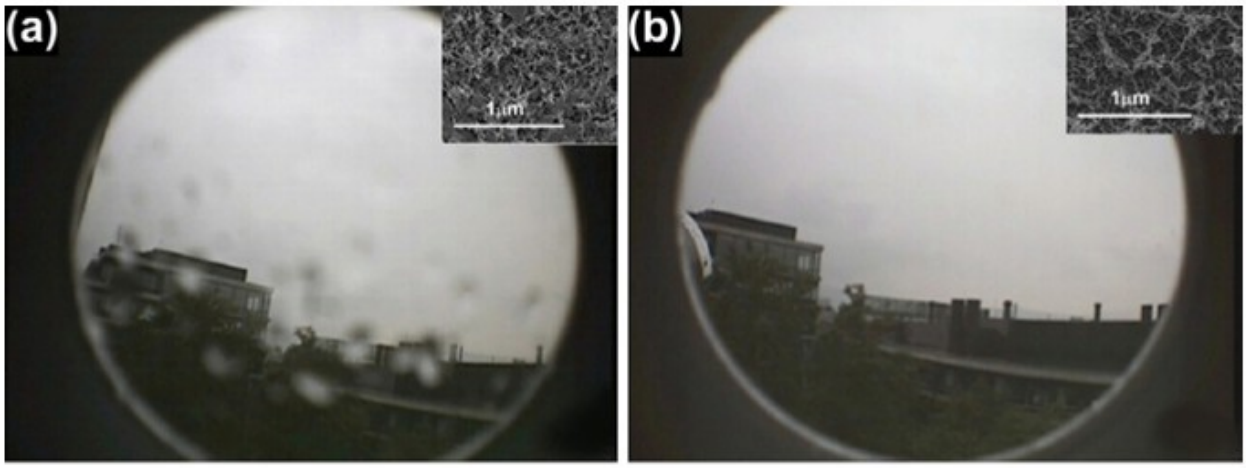

Fig. 35. The application examples of biomimetic superhydrophobic surfaces. (a) and (b):Webcam images taken through an uncoated (a) and coated (b) glass slide during rainfall after 12 months of outdoor exposure, showing different self-cleaning abilities [16]

For many devices, such as the car windscreen and the glasses, the optical transparency is a very special and important property. Preparing the transparent superhydrophobic surface has aroused considerable interest for many materials researchers. Hydrophobicity and transparency, however, are two contradictory properties of the surface. Increasing the surface roughness is beneficial for the hydrophobicity, while the transparency decreases due to the light-scattering losses. Therefore, controlling of surface roughness to an appropriate position is to meet the requirements for both the two key factor. Watanabe and coworkers reported a sol–gel method for producing transparent boehmite films on glass substrates. The surface roughness could be precisely controlled

in the range between 20 and 50 nm . This method, however, requires as high as 500 °C heating process (500 °C), which is incompatible with many optical devices. To solve this problem, a microwave plasma-enhanced chemical vapor deposition process was adapted to prepare transparent superhydrophobic films at temperatures as low as 100 °C (. Jiang and coworkers prepared multifunctional ZnO nanorod films with visible-light transparency and superhydrophobic properties through controlling the diameter and length of nanorods using a low-temperature solution approach. The diameter and the spacing between the nanorods are both less than 100 nm. Such surface nanostructures are small enough not to give rise to visible light scattering. Cohen, Rubner and coworkers demonstrate a Layer-by-Layer processing scheme that can be utilized to create transparent superhydrophobic films from SiO2 nanoparticles of various sizes (Fig. 36). By controlling the placement and level of aggregation of differently sized nanoparticles within the resultant multilayer thin film, it is possible to optimize the level of surface roughness to achieve superhydrophobic behaviour with limited light scattering .

Fig. 36. Image of a glass slide coated with a transparent, superhydrophobic multilayer with antireflection properties [16]

4.4. Anti-corrosion and Anti-fouling

Besides of the above, Suzuki et al. employed a superhydrophobic surface to concentrate a droplet of sample solution evaporatively for the stripping analysis of heavy metal ions and a superhydrophobic surface was formed with polytetrafluoroethylene beads. With this method, there is an accompanying advantage, namely, that both the heavy metal ions and the supporting electrolyte are concentrated. Therefore, it is not necessary to add a large amount of supporting electrolyte to the sample solution. At the same time, they believed that the detection limit would be improved further if the method for the formation of a superhydrophobic layer is optimized. Yin et al. investigated the corrosion resistance of bare and the superhydrophobic copper in seawater by cyclic voltammograms and electrochemical impedance specroscopy. The results showed that the corrosion rate of Cu with superhydrophobicity decreased dramatically due to its special microstructure. Brinker et al. presented an experimental study of a low-Reynolds number shear flow between a regular grooved texture augmented with a superhydrophobic coating and water, showing the patterned superhydrophobic surface have apparent drag-reduction ability.

The pure water (pH value is 7) was commonly used for the contact angle measurements. Recently, the measurements for contact angel in whole pH range have aroused considerable interest from many researchers because of the wide application environments of this kind of superhydrophobic materials. For the engineering materials, undoubtedly, the resistance to the water or corrosive liquid will greatly enhance their anticorrosive ability, broaden its application environment and extend their service life. The superhydrophobic surfaces are able to withstand salt solutions in a wide range of concentrations, which may open a new avenue in applications especially for the marine engineering materials where salt resistance is required. Liu's group and our group reported the superhydrophobic engineering materials such as the, steel, copper, aluminium and its alloy. These superhydrophobic engineering materials showed superhydrophobicity in nearly the entire pH range, so they can be used in strongly corrosive environments. Furthermore, graphite carbon has intrinsic thermal and chemical resistance. Jiang and coworkers reported a nanostructured carbon films by pyrolyzing nanostructured polyacrylontrile films. The films also showed superhydrophobicity in nearly the entire pH range.

i. **Biofouling**:

- → Adds **330 lbs/meter^2** in just **6 months**
- → **$70.000** – cost to clean a ship hull
- → **40 –50%** increased fuel cost
- → **$2,1 billion** –annual cost to US Navy

Figure : Biofouling problem on the hulls of ship

ii. **Corrosion**:

i. *Pipe Corrosion and Fouling*:

➔ **$6 –8 billion** –transmission pipelines

➔ **$276 billion** –residential plumbing costs

Figure : Pipe Corrosion and Fouling

ii. *Bridge Corrosion*:

➔ Annual cost of US Bridges: **$7 billion**

Figure : Bridge Corrosion

5 Experimental Procedure

5.1. Introduction

The objective of this project is twofold. Firstly, to study the parameters that create and optimize the super-hydrophobic film through chemical deposition and secondly, to study how the film effects the corrosion behavior of copper.

A CSD (Chemical Solution Deposition) method was used to fabricate the superhydrophobic film on copper specimens. One of the purposes of this review was to find and study the parameters that play significant role to the fabrication of the film and through understanding them, to optimize the procedure and film. Such parameters are the temperature,the angle of the specimens, the elapsed time and the percentage of n-tetradecanoic acid in the ethanol solution.

The main objective however, is to prove through some potentiodynamic polarization curves the superiority in corrosion of copper specimens with super- hydrophobic film than these without. We also studied the difference in corrosion behaviour between a fully grown and optimized super-hydrophobic film, a semi grown and bare copper.

For better understanding of super-hydrophobic film we make some extra measurements. We take contact angle measurements with optical tensiometry and we used a Scanning Electron Microscope (SEM) to study in detail the copper's structure in every occasion.

The following pages of this section describe the experimental procedure that had been followed step by step, as well as describe the principles of experimental methods.

5.2. Raw Material

Cu substrates were obtained from a commercial wafer fabrication plant. They were two bars of Electrolytic Tough Pitch Copper. The dimension of each bar was: L=15.0cm B=4,0cm T=0,4cm
Nominal chemical composition % by weight: Copper 99.90%, Oxygen 0.05%
Mohs Hardness: 3 (=369MPa Vickers hardness)

General properties	
Name, Symbol, Number	Copper, Cu, 29
Element category	transition meta
Group, Period, Block	11, 4, d
Standard atomic weight	63.546 (3)

Physical properties	
Phase	Solid
Density (near r.t.)	8.96 g·cm^{-3}
Liquid density at m.p.	8.02 g·cm^{-3}
Melting point	1084.6 °C
Boiling point	2562 °C
Heat of fusion	13.26 kJ·mol^{-1}
Heat of vaporization	300.4 kJ·mol−1
Molar heat capacity	24.440 J·mol^{-1}·K^{-1}

Atomic properties	
Electronegativity	1.90 (Pauling scale)
Atomic radius	128 pm
Covalent radius	132±4 pm
Van der Waals radius	140 pm

5.3. Cutting off Process

The next step was the cutting. The purpose of cutting is to section a representative, yet manageable sample from a large or irregular piece of a given material, or to obtain sections in specific angles, for example cross sections. The bars were cut in sections using the Struers Discotom 50 (Fig.37)

Fig. 37. Struers Discotom 50

Section dimensions were 2 cm x 1,85 cm. (Fig. 38)

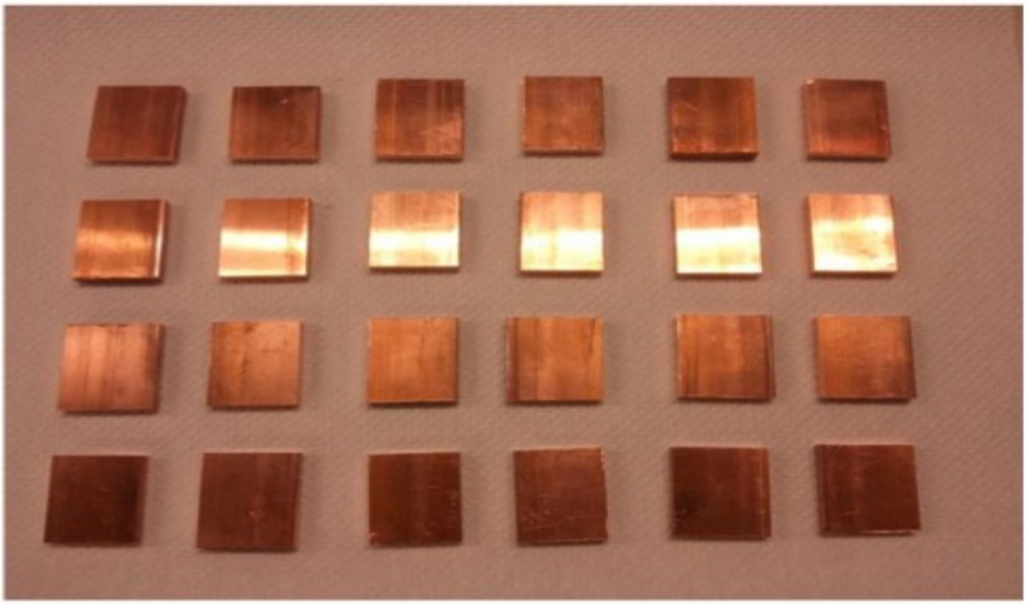

Fig. 38. Copper specimens

5.4. Cold Mounting Process

After finishing with the cutting off process, coming up next was the cold mounting process. Mounting also allows for a safer, more convenient handling of small, sharp or irregularly shaped specimens or when the protection of layers is imperative. Cold mounting is especially suited for mounting specimens that are sensitive to heat or pressure. Additionally, cold mounting does not require an investment in a mounting press and is therefore good for infrequent mounting tasks. The resin, a mixture of two or three components, is poured over the specimen after it has been placed in a mounting cup. After curing for 24 hours, the specimen can be taken out of the cup and processed. Samples were mounted using the EpoFix Kit (Fig. 39) from Struers before experiment, leaving an exposed area of 20 mm × 18.5 mm on the material surface.

Fig. 39. Epofix Kit: Resin, Hardener, Mounting cup, Mixing cup

5.5. Grinding Process

Grinding is the next stage in mechanical material removal. Proper grinding removes damaged or deformed surface material while introducing as little new deformation as possible, thus preparing the sample surface for polishing if necessary. Grinding is divided into two processes: Plane Grinding and Fine Grinding.

Plane Grinding

The grinding process always begins with plane grinding. Plane grinding ensures that the surfaces of all specimens are in the same condition before the preparation continues, and that the surfaces of all specimens in a specimen holder are at exactly the same level.

Fine Grinding

Single specimen preparation is usually started with fine grinding. Fine grinding must remove the deformation existing from cutting or plane grinding and produce a surface that is ready for experimentation. Choosing the correct fine grinding materials is vitally important to ensure fast and economical preparation.

The equipment we use for the process was:

i. Struers LaboPol – 5 (Fig.40)
ii. Struers MD-Fuga Silicon Carbide Papers: 80 grade- 180 grade - 320 grade – 800 grade – 1000 grade - 1200 grade – 1500 grade (Fig.41)

Fig. 40. Struers Laboforce -5

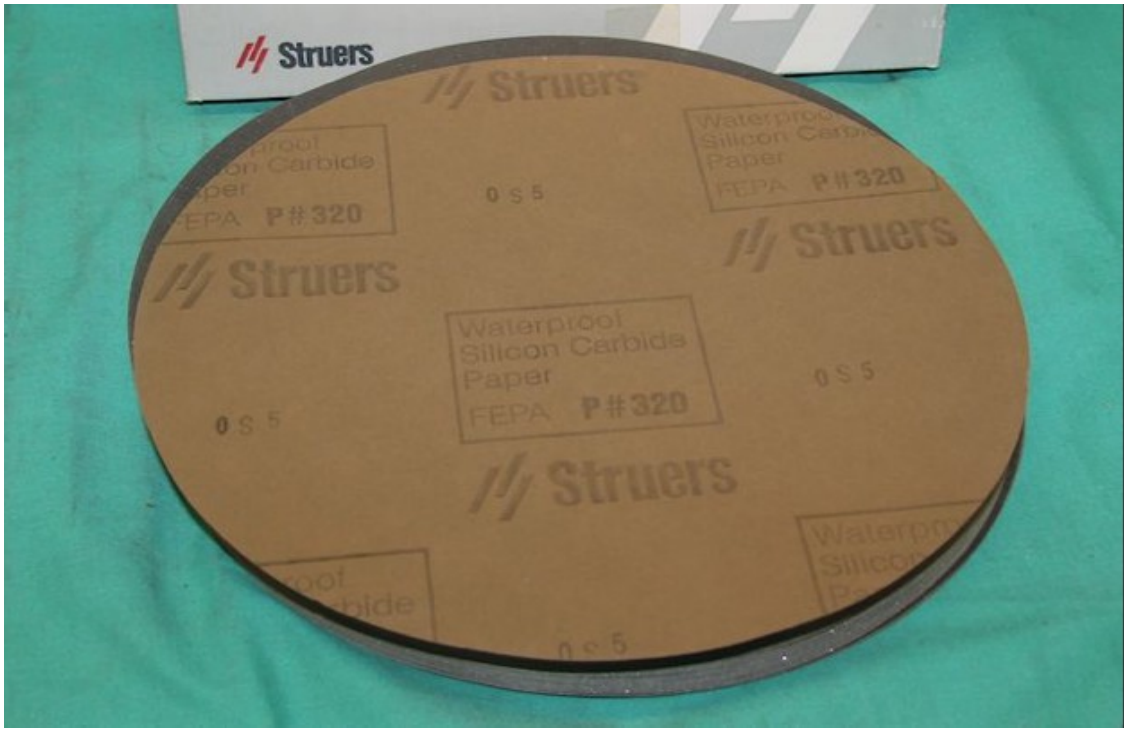

Fig. 41. Struers Silicon Carbide Paper – 320 grade

5.6. Preparation of Super-hydrophobic Surfaces

The front surface of the copper specimens was polished using silicon carbide papers from 80 to 1500 grade, then degreased with acetone, washed with distilled water and dried . Cu substrates were etched in 70% HNO_3 for 10 s to remove surface oxides. The etching provided a fresh and active surface. The etched substrates were rapidly rinsed with deionized water followed by pure ethanol. They were subsequently immersed in an ethanol solution of n- tetradecanoic acid (myristic acid, $CH_3(CH_2)_{12}COOH$) at room temperature. The immersed Cu substrates were rinsed with deionized water and ethanol thoroughly, and then dried in air.

Myristic acid is commonly added co-translationally to the penultimate, nitrogen-terminus, glycine in receptor-associated kinases to confer the membrane localization of the enzyme. The myristic acid has a sufficiently high hydrophobicity to become incorporated into the fatty acyl core of the phospholipid bilayer of the plasma membrane of the eukaryotic cell. In this way, myristic acid acts as a lipid anchor in biomembranes.

The above procedure is a CSD method to fabricate super-hydrophobic film on copper substrates. For the needs of the review we picked a series of parameters, which we altered through the process, in order to find the ideal rates and values of the parameters that optimize the super-hydrophobic film.

The parameters are: *Angle, Molarity of myristic acid in the solution, Days of Immersion*

Angle: We switched the angles in which the copper specimens were placed in the ethanol solution of myristic acid. 0° , 30° , 60° , 180° are the angles we placed the specimens, in order to see the impact, angle has to the fabrication of a superhydrophilic film through chemical solution deposition.

Molarity of myristic acid in the solution: We made ethanol solution of n-tetradecanoic acid of different molarities. The solution we tested had molarities varying from 0.03M to 0.09M. The latest surveys on the field pointed out that the right molarity of n-tetradecanoic acid for the ethanol solution is 0.05-0.06M and thats the reason we chose the range 0.03M to 0.09M, so we can have a clearer answer to which is the ideal molarity of the solution that optimizes the super-hydrophobic film and what happens in lower and higher molarities.

Days of Immersion: The last parameter we chose to alter was the days we left the copper specimens in the solution. At the experiment we immersed copper for 3 days, 6 days, 10 days and 15 days, so we could see the fabrication progress of the film at the above stages of immersion and have our conclusions.

Image. Nitric acid, Electric Scale, Myristic acid, Ethanol

5.7. Experimental Equipment

In the following section we will introduce the equipment we used at the experiment. A stereo microscope and a scanning electron microscope helped us have a closer look at the super-hydrophobic film and the flowerlike structure of the treated surface. In order to have a precise measurement of the contact angle, we visited the Dimokritos research center and used their optical tensiometer. Finally, for our electrochemical measurements we used a three electrode cell to investigate the corrosion properties of the treated copper substrates, calculate the corrosion rate and make the comparison with the bare copper substrates.

5.7.1. Stereo Microscope

The stereo or dissecting microscope is an optical microscope variant designed for low magnification observation of a sample using incident light illumination rather than transillumination. It uses two separate optical paths with two objectives and two eyepieces to provide slightly different viewing angles to the left and right eyes. In this way it produces a three-dimensional visualization of the sample being examined. Stereomicroscopy overlaps macrophotography for recording and examining solid samples with complex surface topography, where a three-dimensional view is essential for analyzing the detail.

The stereo microscope is often used to study the surfaces of solid specimens or to carry out close work such as dissection, microsurgery, watch-making, circuit board manufacture or inspection, and fracture surfaces as in fractography and forensic engineering. They are thus widely used in large numbers in manufacturing industry, both for manufacture, inspection and quality control. It tends to make them of lower cost compared with conventional microscopes.

The stereo microscope should not be confused with a compound microscope equipped with double eyepieces and a binoviewer. In such a microscope both eyes see the same image, but the binocular eyepieces provide greater viewing comfort. However, the image in such a microscope is no different from that obtained with a single monocular eyepiece.

We used the Stereo microscope of our lab a Leica MZ6 (Fig. 42)to got a first look at flowerlike structure of the Super-hydrophobic surfaces that had been obtained after the immersion time in the ethanol solution of n-tetradecanoic acid.

Fig. 42. Leica MZ6 Stereomicroscope

5.7.2. Scanning Electron Microscope

The most versatile electron microscope is the SEM. Thus, the SEM is used to observe and characterize surface features over large (or small) areas of the specimen. The primary electron beam interacts with the specimen surface to produce secondary electrons, backscattered electrons, and x-rays. With detectors mounted just above the specimen, these electrons and x-rays can be collected and analyzed to provide important information about the specimen surface. Subsequently, we look at each interaction.

The backscattered electrons are those electrons that are scattered from the specimen surface and can be collected as the primary beam scans the specimen surface. The collected backscattered electron image of the specimen surface is displayed on a cathode ray tube (CRT) and can be photographed. There is some electron energy loss during the backscattering process. The higher the atomic number of the elements in the sample, the greater the degree of backscattering (less energy loss). This means that elements with higher atomic numbers, such as iron with an atomic number of 26, will appear brighter on the backscattered electron image on the CRT than elements with lower atomic numbers, such as oxygen with an atomic number of only 8.

Secondary electrons, on the other hand, are the result of the interaction of primary (beam) electrons with those electrons contained within the atoms in the sample. The primary electrons can actually knock the loosely held orbital electrons from atoms. These displaced electrons are called secondary electrons. The secondary electrons have much lower energy than the backscattered electrons described previously. This means that secondary electrons are only detected from the surface and near-surface regions of the specimen, because those from deeper regions are easily absorbed by the sample. Thus, secondary electrons yield a secondary electron image on the cathode ray tube that reveals surface topography and produces an image with enhanced depth of field. It is this depth of field that makes the SEM one of the most useful of all electron microscopes. Note the tremendous depth of field that is obtained. This capability is what makes the SEM a popular instrument for studying surface features. The remarkable advantage is that the images can be obtained at magnifications varying from 10 to 30,000x. As an example, a small copper support grid for viewing surface replicas and thin foils is examined in the SEM. The grid viewed in the SEM shows a secondary electron image at 1000x in Fig. 43a and a backscattered electron image in Fig. 43b. The grid openings are produced by a punching process.

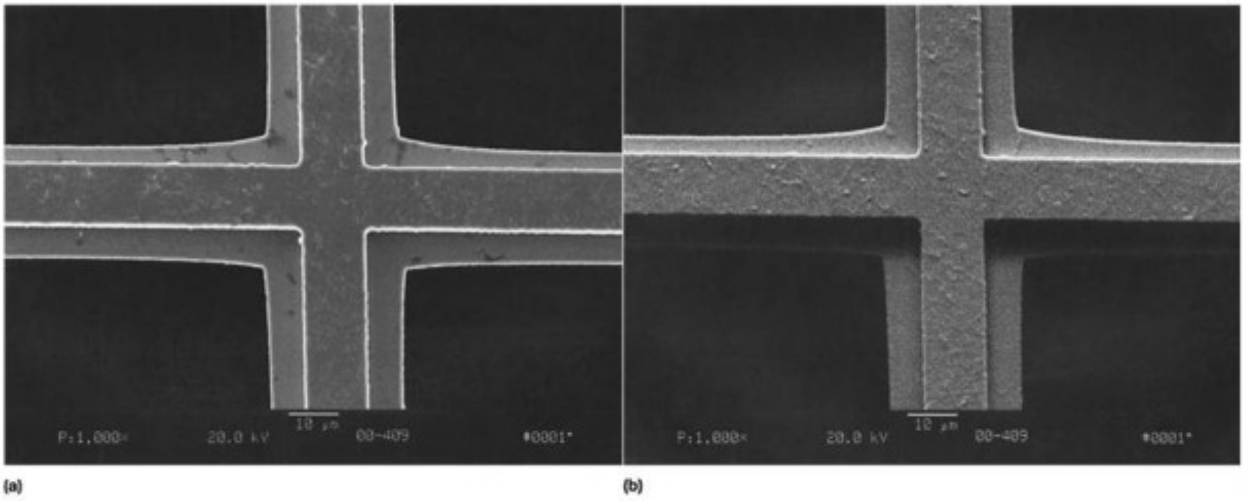

Fig. 43. A copper grid made by the punching process, as seen in the scanning electron microscope. (a) Secondary electron image (760x) and (b) backscattered electron image

X-rays are also emitted from the sample, because of the interaction of the primary and backscattered electrons with the inner shell electrons of atoms in the sample.The primary/backscattered electrons have sufficient energy to knock inner shell electrons (the shell closest to the atom nucleus) out of orbit. Where an electron is knocked out of a particular inner electron shell, an x-ray is emitted when an electron (from an electron shell further out from the nucleus) moves into its place. These x-rays have a characteristic energy (and wavelength) for the particular atomic species present. Because of this, they are called characteristic x-rays. This means that every x-ray that is collected has an energy and wavelength that is unique to the particular element present in the sample. The importance of collecting these x-rays is that compositional information can be thus obtained. Generally, in a SEM, only the x-ray energy is analyzed. The technique is called energy dispersive spectroscopy, or EDS. An example of an EDS analysis is shown in Fig. 44. The energy spectrum of the x-rays collected from the inclusion is shown in Fig. 44. The intensity, or number of x-rays, is plotted on the vertical axis, and the x- ray energy is plotted on the horizontal axis. In this particular case, the peaks in the energy spectrum indicate that calcium, aluminum, and sulfur are present (there are traces of manganese, silicon, and potassium; the iron is from the specimen itself). This analysis indicates the elements present but does not reveal the distribution of elements within the inclusion.

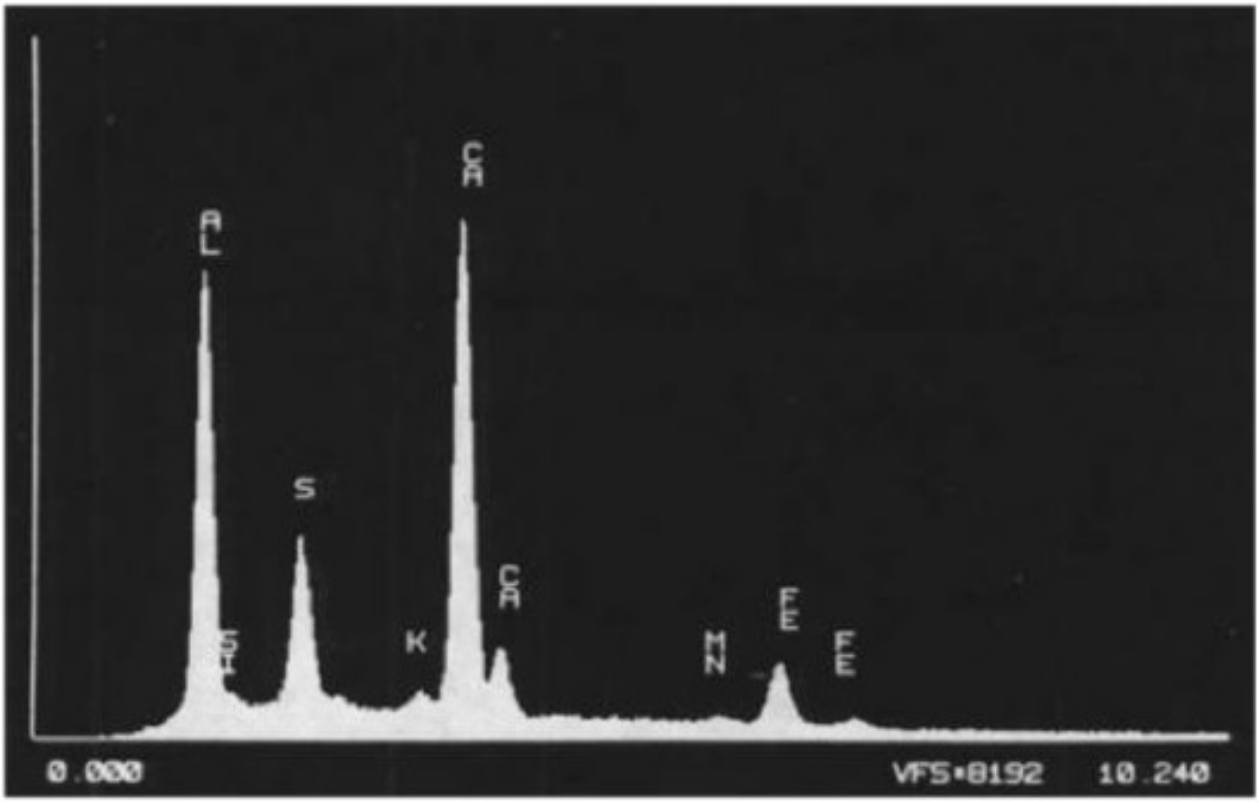

Fig. 44. An EDS spectrum of the elements contained in the nonmetallic inclusion. This EDS spectrum was photographed from the cathode ray tube of the EDS unit.

We used a JEOL JSM-6390 Scanning Electron Microscope Fig.45, with Resolution: 3.0 nm(30kV), Accelerating voltage: 0.5 to 30 kV, Magnification: x5 to 300,000, Filament: Pre-centered W hairpin filament (with continuous auto bias), Objective lens: Super conical lens, Objective lens apertures: Three position, controllable in X/Y directions. With SEM we succeeded to study the flowerlike structure of the Super- hydrophobic surfaces in a very close range.

Fig. 45. JEOL JSM-6390 Scanning Electron Microscope

5.7.3. Optical tensiometry contact angle measurements

Analysis of the shape of a drop of test liquid placed on a solid is the basis for optical tensiometry (goniometry). The basic elements of an optical tensiometer (also called contact angle meter) include light source, sample stage, lens and image capture. Contact angle can be assessed directly by measuring the angle formed between the solid and the tangent to the drop surface.

The production of drops with advanced and receded edges involves one of two strategies. Drops can be made to have advanced edges by addition of liquid. Receded edges may be produced by allowing sufficient evaporation or by withdrawing liquid from the drop. Alternately, both advanced and receded edges are produced when the stage on which the solid is held is tilted to the point of incipient motion. Using an instrument with high speed image capture capabilities shapes of drops in motion may be analyzed.

To measure the contact angle of the treated copper specimens we visited the Dimokritos research facilities and used their optical tensiometer Fig. 46.

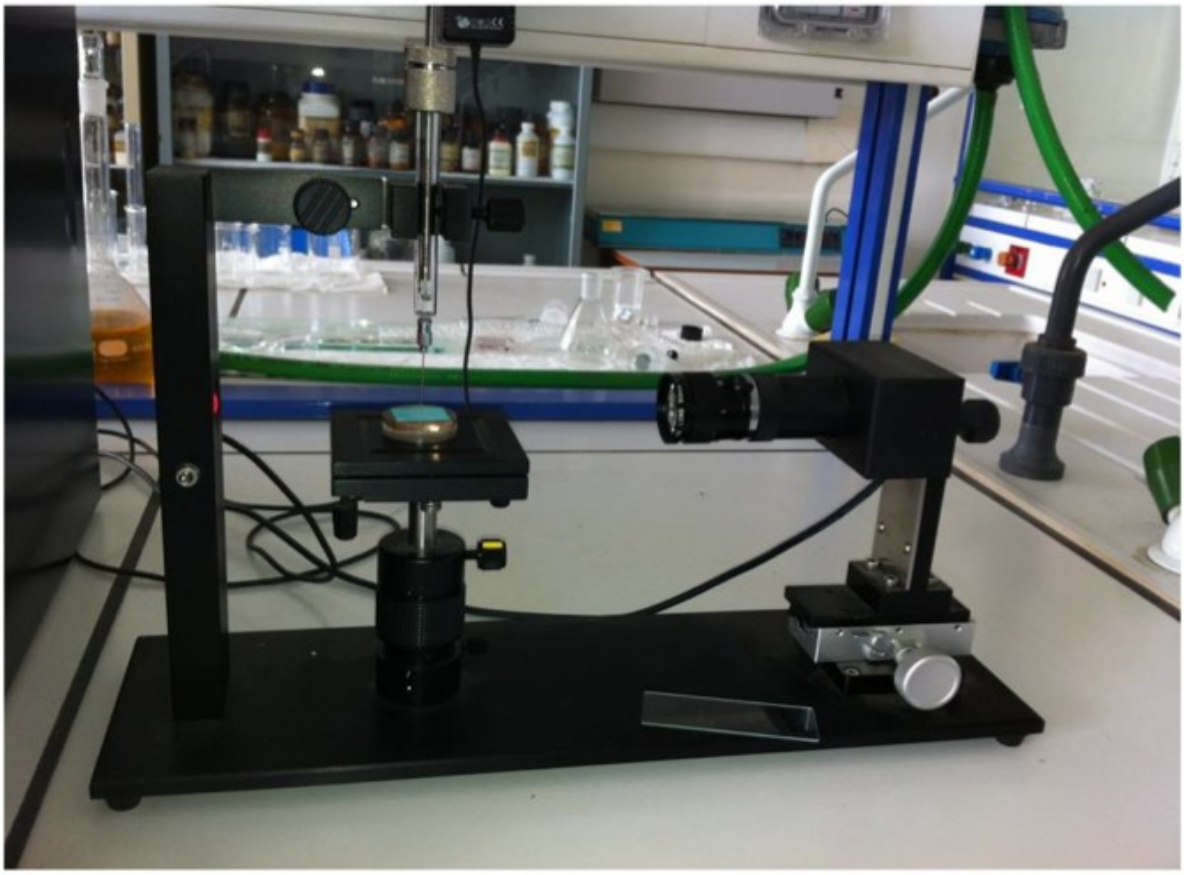

Fig. 46. The experimental setup we used at Dimokritos research center

5.7.4. Electrochemical Measurements

5.7.4.1. Three-electrode cell

The three-electrode cell is the standard laboratory apparatus for the quantitative investigation of the corrosion properties of materials.It can be used in many different types of corrosion experiments. It is a refined version of the basic wet corrosion cell and a typical example is illustrated in Fig. 47. For our electrochemical measurements we used the three-electrode cell of our lab in Fig.48, Model K0235 Flat Cell. First we shall examine the components in more detail.

Fig 48. The three-electrode cell of our lab, Model K0235 Flat Cell

The working electrode

The working electrode is the name given to the electrode being investigated. It is useful, though not essential, the electrode is designed to have a surface area of 100 mm^2 (1 cm^2), current measurements can then be more readily converted into current densities, which should be used in calculations. We use the term 'working electrode' rather than `anode' because we are not limited to investigations of anodic behaviour alone; cathodic behaviour can also be examined.

Electrical connection must be made to the specimen, and this can be done with solder or spot weld on the reverse side before mounting. After mounting, specimens are often ground and polished, as for metallographic examination. If this technique is used, the surface will be activated, in other words, passive films may have been either removed entirely or just changed from the as-received condition. This should always be borne in mind. Obviously, if the original passive film is part of the corrosion investigation, no pretreatment should be used. In fact, this is the biggest single

reason for discrepancies between lab and field data. Surfaces in real engineering systems are most often as received from manufacture and are not similar to specimens prepared for metallography.

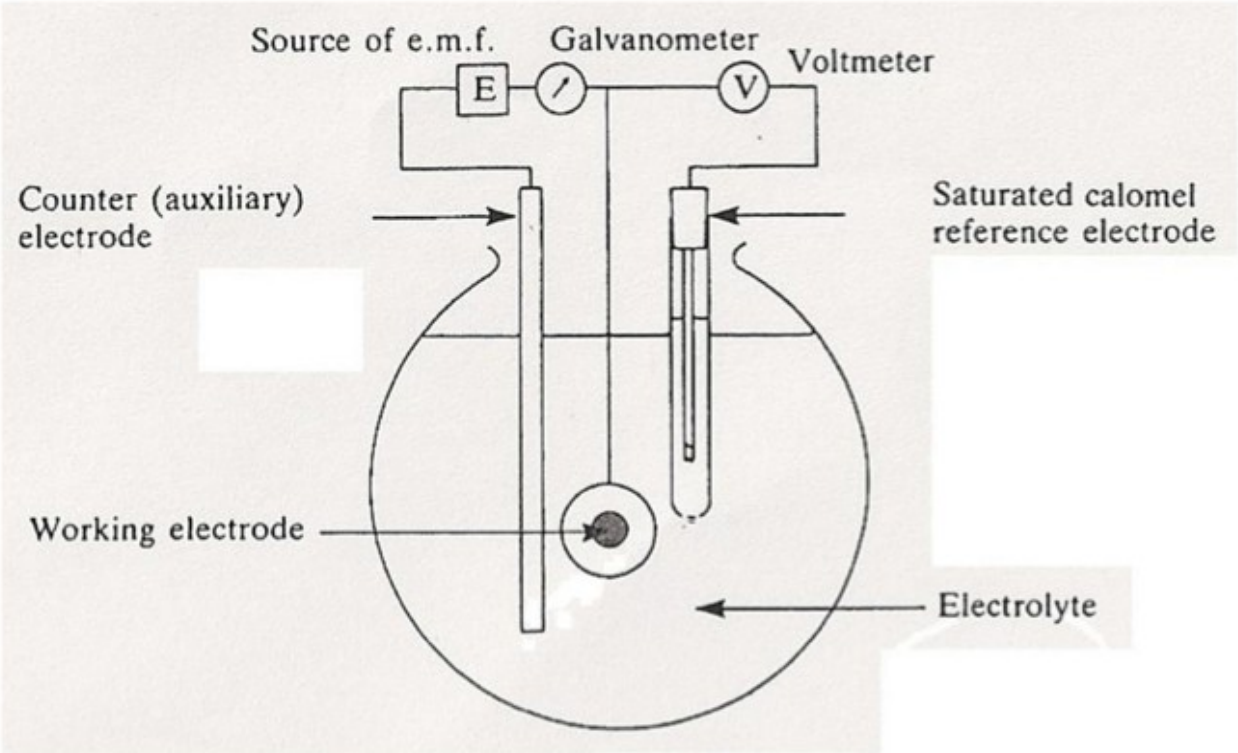

Fig. 47. The experimental apparatus of our labs three-electrode cell, Model K0235 Flat Cell

The Counter Electrode

The counter (auxiliary) electrode: is the name given to the second electrode. The counter electrode is present specifically to carry the current created in the circuit by the investigation, it is not required for measurements of potential. Usually, a carbon rod is used, but it can be any material that will not introduce contaminating ions into the electrolyte. Platinum or gold can also be used with success, especially if space is at a premium, when smaller electrodes can be used, titanium is also suitable. In our experimental setup the counter electrode is made of platinum.

The Reference electrode

The reference electrode: is present to provide a very stable datum against which the potential of the working electrode can be measured. It cannot itself carry any more than the most negligible current. If it did, it would participate in the cell reactions and its potential would no longer be constant, hence the requirement for the counter electrode. By far the most convenient reference electrode to use in such an experiment is a saturated calomel electrode (SCE).

The external circuit can be varied considerably. The essential components are a current-measuring device, a potential-measuring device and a source of potential. The current-measuring device should

be capable of reading microAmps, at least. The potential-measuring device should draw no current during the act of measurement, traditionally potentiometers have been used for this purpose. The modern digital meter, however, can have an impedance of the order of gigohms, and may be used with as good an accuracy as a potentiometer.

The Source of Potential

The source of potential 'drive' the working electrode to produce the desired cell reactions. Typical potentiostats are readily available commercially and have been used extensively by corrosion scientists. Potentiostats apply predetermined potentials to the working electrode so that measurement of the cell current can be made. This is done by altering the current at the counter electrode to maintain the set value of working-to-reference potential. A simple constant voltage source is not suitable. We used a VersaSTAT 4 Fig. 49 The three electrodes are placed in a suitable glass vessel of capacity about 1 liter containing the chosen electrolyte Fig. 47

Fig. 49. Potentiostat VersaSTAT 4

The Electrolyte

Electrolyte is a fundamental part of the whole corrosion process. It is extremely important to consider the conductivity of the electrolyte, since by carrying the ionic current, it plays such an important role in corrosion reactions. The use of a reference electrode is to enable the potential of a working electrode to be measured and it should be placed as close to the electrode surface as possible. This is because the measured potential will always include the potential difference across the electrolyte occupying the space between the working electrode surface and the reference electrode. Most corrosion measurements involve the use of direct currents, so Ohm's Law applies and the potential difference across the electrolyte can be estimated, i.e. V=IR. Not surprisingly, this

potential is often referred to as the Ohmic or IR drop, and may be large if either the current or the resistance of the electrolyte is large. It is usually preferable to make the IR drop as small as possible, otherwise its contribution to the overall cell potential may be difficult to quantify. When using a high conductivity electrolyte, such as 3.5% sodium chloride solution or sea-water, the effect will be small, so the experimental apparatus described in Fig. 47 is adequate for most investigations.

5.7.4.2. *Potentiodynamic Polarization Curve*

The E/log(i) plot, or potentiodynamic polarization curve, is one of the most common methods of examining the corrosion behaviour of materials. It has become common practice in E/log(i)plots for all current densities to be treated as positive. This is really just a convenience for it reduces the size of the graphs and gives a much clearer indication of the value of potential when the current density changes from negative to positive. The portion of the graph for which you measured negative currents that is from -0.400 V to about -0.240 V, represents the copper behaving as a cathode. From - 0.240 V to more positive values of potential, the copper is behaving as an anode and it is during this part of the scan that you will have observed visible changes to the specimen because of the numerous reactions which occurred as the copper corroded. At potentials in the region of -0.050 to -0.080 V, a marked reduction in the corrosion current is observed. This represents partial passivation of the metal because of the presence of the corrosion products, in this case quite small, as evidenced by the relatively small reduction in current. (Fig. 50)

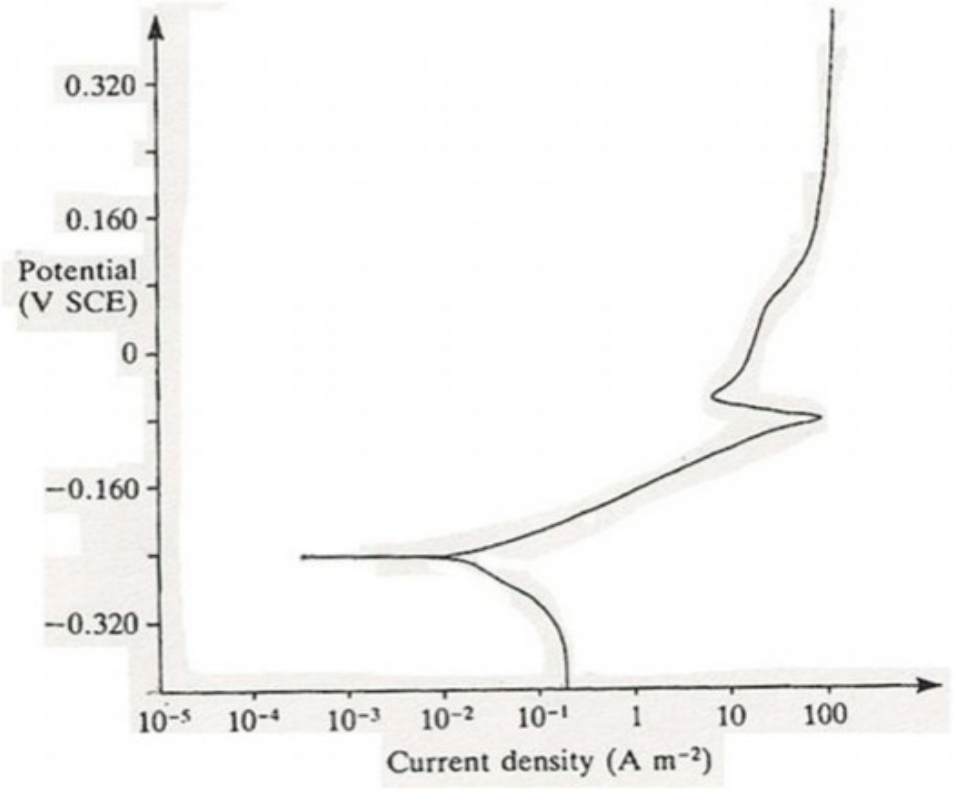

Fig. 50. Potentiodynamic scan for copper in 3.5 % sodium chloride solution

The significance of the changeover from negative to positive currents

In practical terms it represents the state the metal assumes under freely corroding conditions. The value of potential is commonly called the free corrosion potential and the symbol used is E_{corr}. In your experiment you should have, measured E_{corr} at about -0.24 V SCE. At this potential the specimen could be described as being in a steady- state condition, equivalent to the condition it would have achieved with the potentiostat switched off. Remember that the purpose of the instrument is to perturb the potential of the with the potentiostat rest potential. In practice, equilibrium conditions are impossible to achieve, the metal surface acts as an assembly of many tiny anodes and cathodes, and corrosion occurs at a rate given by the theoretical anode current density, i_a. At the free corrosion potential i_a is replaced by i_{corr}, the corrosion current density. This is the simplest way of quantifying the actual corrosion rate under freely corroding conditions, and it emphasizes the importance of carrying out polarisation scans and Tafel plots of the data obtained.

The corrosion rate

Corrosion rate is always equivalent to i_a at the prevailing potential for a metal dissolution reaction. When only a single reversible metal redox reaction is being considered and is at equilibrium, $i_0 = i_a = i_c$. When more than one redox reaction occurs, as in this case, there is a separate exchange current density for each redox process, and the corrosion rate is now symbolised by i_{corr} (still equal to i_a for the metal dissolution).There is no theoretical method for calculating i_0.

One way is to perform E/log(i) measurements very carefully for each metal, both anodically and cathodically polarised under conditions in which the free corrosion potential is a result of only the metal redox pair of reactions.

When the copper is in the region of potential from -0.24 to -0.40 V, it is acting as a cathode in the aqueous corrosion cell. What is the anode and what corrodes in this cell at these potentials?

The auxiliary electrode, in this case the carbon rod, becomes the anode. There is no corrosion, because the auxiliary electrode is chosen so that it will not contaminate the solution with ions which are not part of the investigation. Other electron-producing reactions must take place at the electrode surface if the electrons required by the copper cathode are to be produced. A common reaction in the electrolyte is the generation of oxygen gas by the oxidation of water:

$$2H_2 0 \rightarrow 0_2 + 4H^{+,} + 4e^{-,}$$

Another possibility, again in the chloride-containing electrolyte, is the generation of chlorine gas:

$$2Cl^{-,} \rightarrow Cl_2 + 2e^{-,}$$

6. Results and Discussion [1][2][4][5][11][12][19][20][22]

6.1. Introduction

In this section are given all the results that had been taken from the study of electrolytic tough pitch copper substrates and the study of the Super-hydrophobic specimens of electrolytic tough pitch copper. That results concern the fabrication of super-hydrophobic film, the scanning electron microscope (SEM) and stereo microscope measurements, the contact angle measurements, and the electrochemical measurements. We are going to discuss all that results so we can derive some useful conclusions from this work.

6.2. Fabrication of the Super-hydrophobic Film

We used a chemical solution deposition method to fabricate a valid super-hydrophobic film on our copper specimens. The principles of the specific chemical deposition method are well-known and the results on the fabrication of the film very successful. After the mounting and grinding (80–1500) process, the specimens were chemically modified in an ethanol solution of n-tetradecanoic acid at room temperature, in order to form a Super-hydrophobic film on the fresh copper surface. The above CSD method is very easy to prepare and has a rapid development on the formation of the film.

Our goal was to optimize the CSD procedure by altering various parameters of the method. The parameters we altered and examined were: *the angle of the copper surfaces in the solution, the molarity of the myristic acid in the ethanol solution and the days of immersion*. The results are the following:

Angle:

0°

- The starting-points of the film appear all over the immersed surface
- Successful completion and growing of the super-hydrophobic film
- The film is homogeneously distributed through the whole immersed surface
- The thickness of the film is the same all over the immersed surface
- Duration of the method 9-10 days

30°

The same exact features with 0°

- The starting-points of the film appear all over the immersed surface
- Successful completion and growing of the super-hydrophobic film
- The film is homogeneously distributed through the whole immersed surface
- The thickness of the film is the same all over the immersed surface
- Duration of the method 9-10 days

60°

- The starting-points of the film appear first at the lower levels of the immersed surfaces and then expand to the higher levels
- Semi-Successful completion and growing of the film, at almost the half (lower half of the copper specimen) we see a fully grown super-hydrophobic film, but at the second half (the higher half) we don't have a fully grown film
- The film isn't homogeneously/equally distributed to the copper surface, it is exponentially distributed, with the lower parts having the most distribution and as moving higher it is gradually reducing
- The thickness of the film isn't the the same all over the surface, it is linear and ascending from the lower levels to the higher of the immersed surface
- Duration of the method (semi-successful) 10-11 days

180°

- Very few, almost none starting-points of the super-hydrophobic film
- Unsuccessful method, no fabrication of the super-hydrophobic film
- No progress of the film all over the surface, ergo no distribution, no thickness
- We left the immersed copper specimens with 180° angle for over a month, in order to be sure for the failure the method

Molarity of Myristic acid in the ethanol Solution:

0.03M

- The starting-points of the film appear the 4^{th} - 5^{th} day of immersion
- Slow progress of the film
- very low thickness of the super-hydrophobic film
- Uncompleted film
- Days of immersion 12-13

0.06M

- The starting-points of the film appear the first days, after about 15 – 16 hours
- Quick and satisfying progress of the film
- Normal thickness and homogeneous distribution
- Successful completion of the super-hydrophobic film
- Days of immersion 10 full days

0.09M

- The starting-points of the film appear early at the first day, 9-10 hours after the immersion
- Rapid progress of the film, much quicker than anticipated
- Homogeneous distribution but extreme thickness of the film
- Unsuccessful completion of the film, washed away when rinsed with deionized water or film detachment in the solution
- Days of immersion 8, then we have abruption of the film from the copper surface

Days of Immersion: (we used an ethanol solution of 0.06M myristic acid)

Immersion

- The starting-points appear about 15 – 16 hours after the immersion of the copper specimens
- Slim formation of film

3 days have passed

- The thickness is increasing nicely
- We have homogeneous distribution already

6 days have passed

- Satisfying full grown super-hydrophobic film with hierarchical structure, micro- and nano-structure
- Completion of the CSD method after 10 full days

10 days have passed

- The development of the film continues, it grows thicker and thicker, parts start to detach from the surface due to extreme development and thickness of the film
- Detachment / Abruption of the whole film, either while in the solution or when we rinsed the substrates with deionized water

15 days have passed

Formation mechanism of super-hydrophobic film

Self-assembled monolayers of n-alkanoic acid ($CH_3(CH2)_m$ COOH, m= 2–18, 22) are formed on the native oxide surfaces of Cu easily. We presume Cu^{2+} ions are continuously released from Cu, into the n-tetradecanoic acid solution, while O_2 is reduced according to Eq. (1). The released copper ions are captured by coordination with n-tetradecanoic acid molecules, forming copper carboxylate (copper tetradecanoate) according to Eq. (2).

$$2Cu + O_2 + 4H^+ \rightarrow 2Cu^{2+} + 2H_2O \quad (1)$$

$$Cu^{2+} + 2CH_3(CH_2)_{12}COOH \rightarrow Cu[CH_3(CH_2)_{12}COO]_2 + 2H^+ \quad (2)$$

As the above reaction (2) proceeds, a concentration gradient of copper tetradecanoate is developed, starting from the copper electrode towards the bulk solution. The concentration of copper tetradecanoate surrounding the copper electrode is the highest in the solution, resulting to copper tetradecanoate precipitation in the electrode surface.

Conclusions

All three of the parameters we chose to examine, so that we can optimize the CSD method of fabricating a super-hydrophobic film on copper surfaces, played significant role to the process. Reading the results we can see clearly that by altering the angle of the immersed copper surface, the molarity of myristic acid in the ethanol solution and the days of immersion, we affect greatly the fabrication and influence the progress and quality of the results.

By changing the angle, we observe that both distribution and thickness of the film are influenced. The more we increase the surface angle, the less homogeneous is the distribution and the less satisfying is the thickness values. Moreover, when the angle reaches 180° (specimen is upside down) the method doesn't work at all, we don't see the flowerlike structure that we anticipate, nor the light blue characteristic color of the film.

The molarity of myristic acid in the ethanol solution appeared to be of extreme importance. The molarity rate that was the most efficient and had the best results was 0.06M myristic acid. By increasing the molarity of myristic acid in the solution, we saw that the rapid progress of the film led to an unstable super-hydrophobic surface and abruption of the film from the copper surface. By decreasing the molarity rate, the film formation appeared to be incomplete, only a slim film was fabricated.

Finally, the days of immersion played a very significant role to the fabrication as well. We used an ethanol solution of 0.06M myristic acid, which we concluded that is the most efficient, and observes the progress of the CSD method during the days. The formation of the hierarchical structure of the super-hydrophobic film was complete after 10 full days after the immersion of the copper specimens. Earlier of the 10 days, we observed the appearance of the starting-points and the progress of the film formation. After the 10 days the film appeared to fade in quality, due to extreme thickness and rapid generation of the film, and eventually was detached from the copper surface.

Taking in consideration all of the above, we chose the rates and values of the 3 parameters that optimize the CSD fabrication of super-hydrophobic surfaces method. The optimized CSD method is:

"The front surface of the copper specimens have to be polished using silicon carbide papers from 80 to 1500 grade, then degreased with acetone, washed with distilled water and dried . Cu substrates should be etched in 70% HNO_3 for 10 s to remove surface oxides. The etching is providing a fresh and active surface. The etched substrates must rapidly be rinsed with deionized water followed by pure ethanol. Subsequently they have to be immersed in an ethanol solution of ***0.06M*** *n- tetradecanoic acid (myristic acid, $CH_3(CH_2)_{12}COOH$), in an angle* ***not bigger than 30°****, for* ***10 full days*** *at room temperature. The immersed Cu substrates should be rinsed with deionized water and ethanol thoroughly, and then dried in air."*

Fig. 51. Image of specimens treated in 0.09M myristic acid, unsuccessful CSD method, abruption of the Super-hydrophobic film

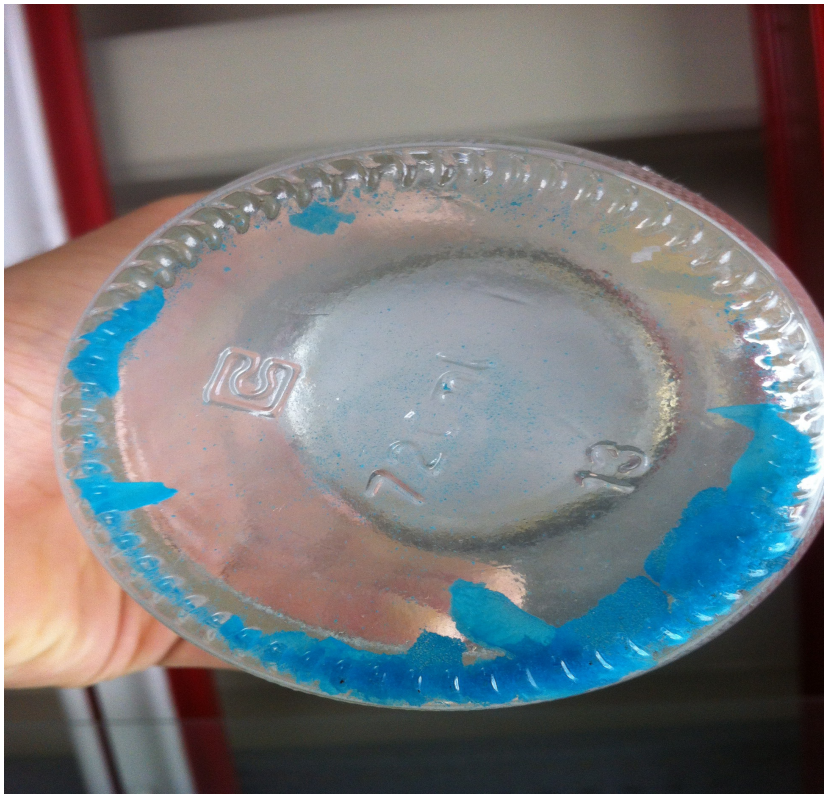

Fig. 52. Image of the super-hydrophobic film remains at the bottom of the solution

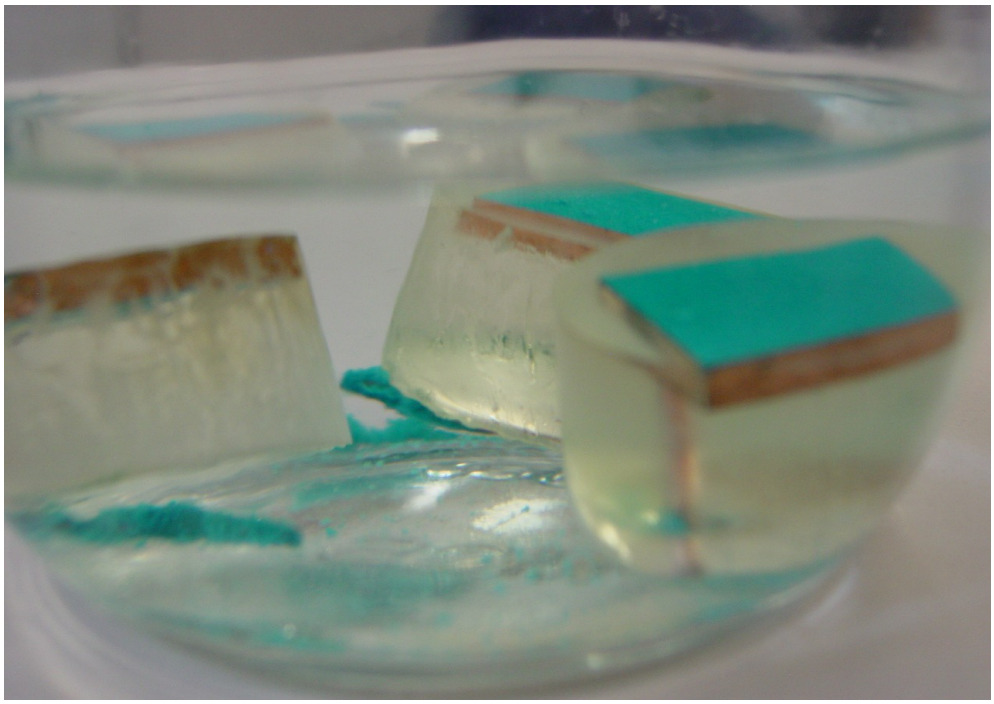

Fig. 53. Image of specimens in the solution with 30°

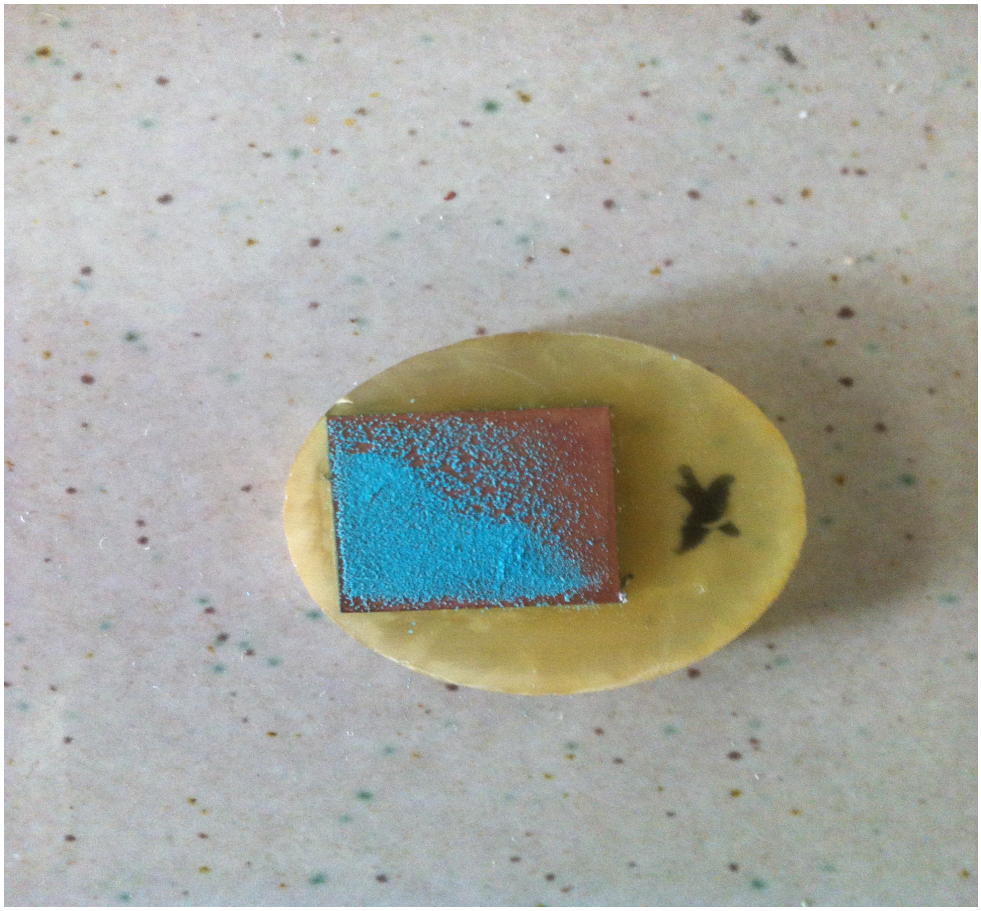

Fig. 54. Image of the super-hydrophobic film produced, specimen treated in 60° angle

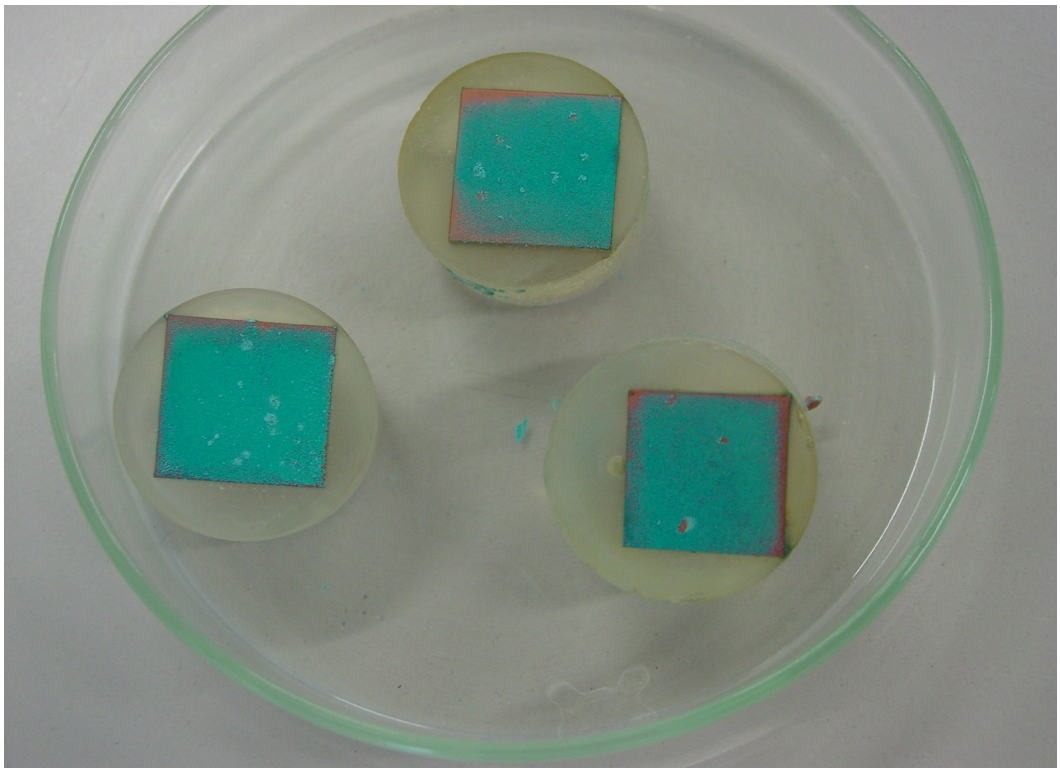

Fig. 55. Image of film produced after 3 days immersion time in 0.06M

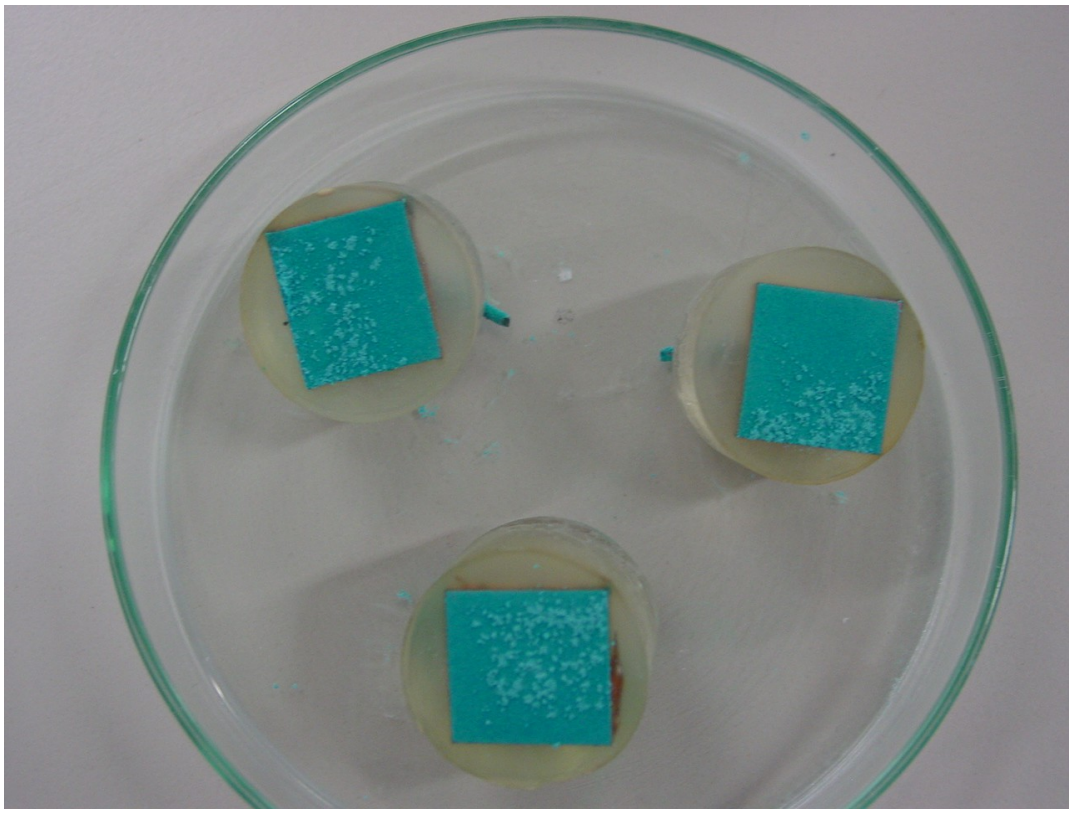

Fig. 55. Image of film produced after 6 days immersion time in 0.06M

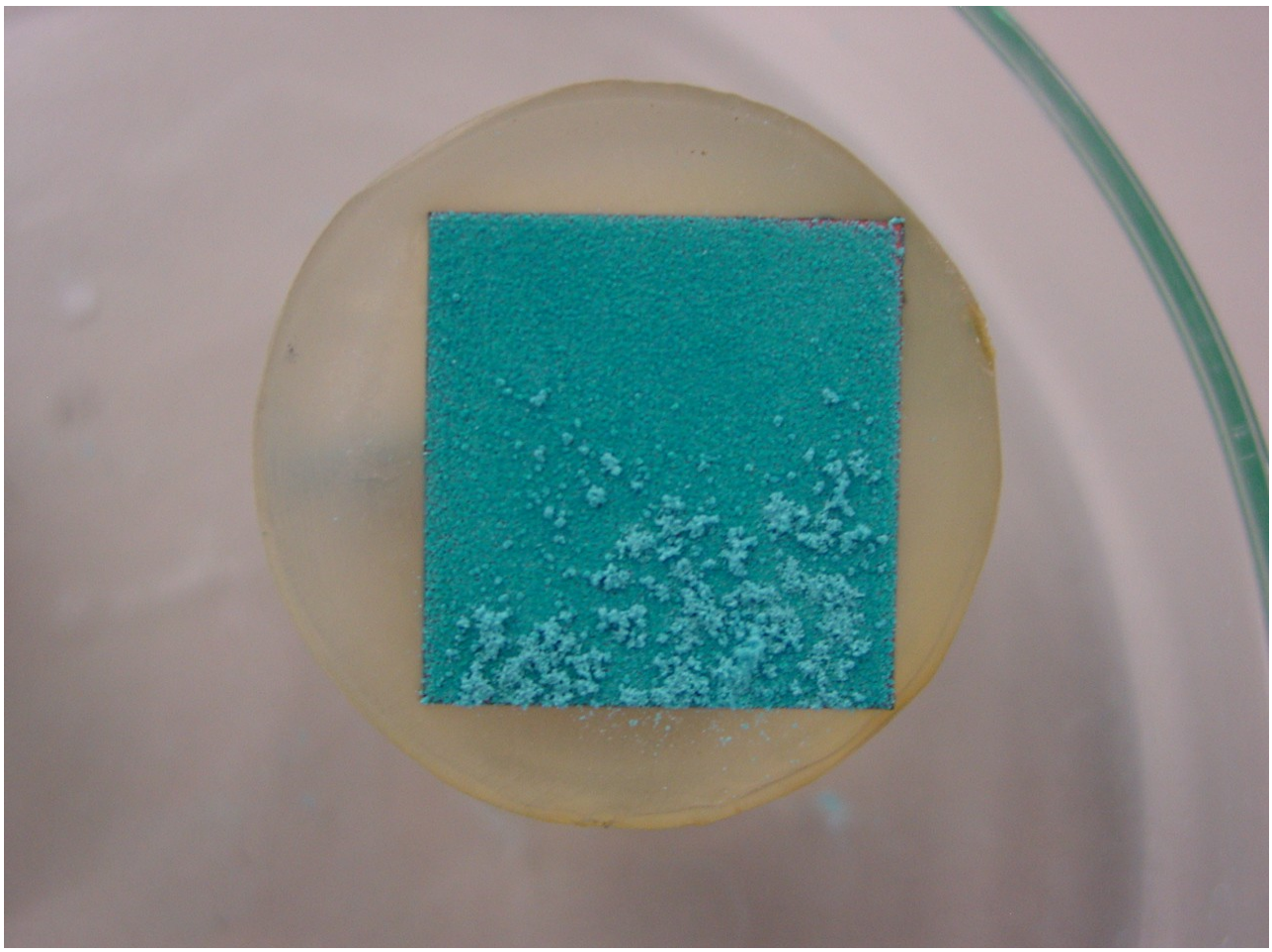

Fig. 55. Image of super-hydrophobic f ilm fabricated by the optimized CSD method, meaning after 10 days immersion time in 0.06M

6.3. Contact Angle Measurements

Below are presented the Contact Angle measurements. We measured five different types of specimens:

- clean copper specimen
- copper specimen with 3 days immersion time in an ethanol solution of 0.06M n- tetradecanoic acid
- copper specimen with 6 days immersion time in an ethanol solution of 0.06M n-tetradecanoic acid
- copper specimen with 10 days immersion time in an ethanol solution of 0.06M n-tetradecanoic acid
- copper specimen where the Super-hydrophobic treatment had been manually removed

The measurement on the treated specimen, were very difficult to obtain, since the droplets did not stand still on the surface and roll off the surface immediately. We had to create droplets, bigger than usual and also to reduce the distance between the stage and the needle. The results of the measurements are presented in the following Table 1 and were extremely encouraging and of great success.

	Left Contact angle	**Right Contact angle**	**Mean Contact angle**
Bare Copper	*62.37*	*58.33*	***60.85***
3 days Treatment	*127.01*	*128.44*	***127.73***
6 days Treatment	*151.63*	*154.38*	***153.00***
10days Treatment	*176.52*	*176.51*	***176.51***
Removed Super-hydrophobic treatment	*101.84*	*102.64*	***102.24***

Table. 1. Contact Angle Measurements

It is obvious that the difference between the treated and the clean surface is significantly large, more than two time Fig. 56-59. The measurements obtained for the clean copper are typical, and in accordance to the literature for super-hydrophobic treatments. For the 10 day immersed specimen the contact angle achieved was extreme, nearly 180°, meaning the water droplet is almost hovering on the surface, the contact between the surface and the water droplet is the minimum. For the 6 day immersed specimen the contact angle is still super-hydrophobic (> 150°) but not that extreme, the 3 day is not super-hydrophobic, but hydrophobic (> 90° and < 150°). When the coating was removed, the measured contact is still high, more than 100 Fig. 60. , implying that may be there is another layer, which still provides hydrophobic properties to the surface.

Moreover, we captured some very interesting images Fig. 61-63 of droplets on the super-hydrophobic surfaces with the Stereo Microscope . We examined how the droplet merely stands on the surface, it is almost hovering on the surface, especially as the contact angle grows wider. We

also came upon the discovery that the size and volume of the droplet is strongly lessened Fig. 64., due to the compression caused to the droplet because of the super-hydrophobic properties of the surface and specifically the extreme contact angle achieved. The super-hydrophobic surface composed of mountains (solid portion of the surface) can easily trap gas within the 'valleys' between the mountains. Therefore, the Cl^- can hardly reach the bare surface for the obstructive effect of 'air valleys'. Another important reason why the modified surface can improve the anticorrosion of copper is 'capillarity'. As we know, when a vertical cylindrical tube is placed in liquid, the liquid rises and forms a concave surface, called a meniscus if the tube is hydrophilic. Otherwise the liquid is depressed, if the tube is hydrophobic and then water transport against gravity is easy in such porous structure. As a result, the seawater can be pushed out from the pores of the superhydrophobic film by the Laplace pressure and be depressed. Then the specimen could be protected perfectly in the seawater.

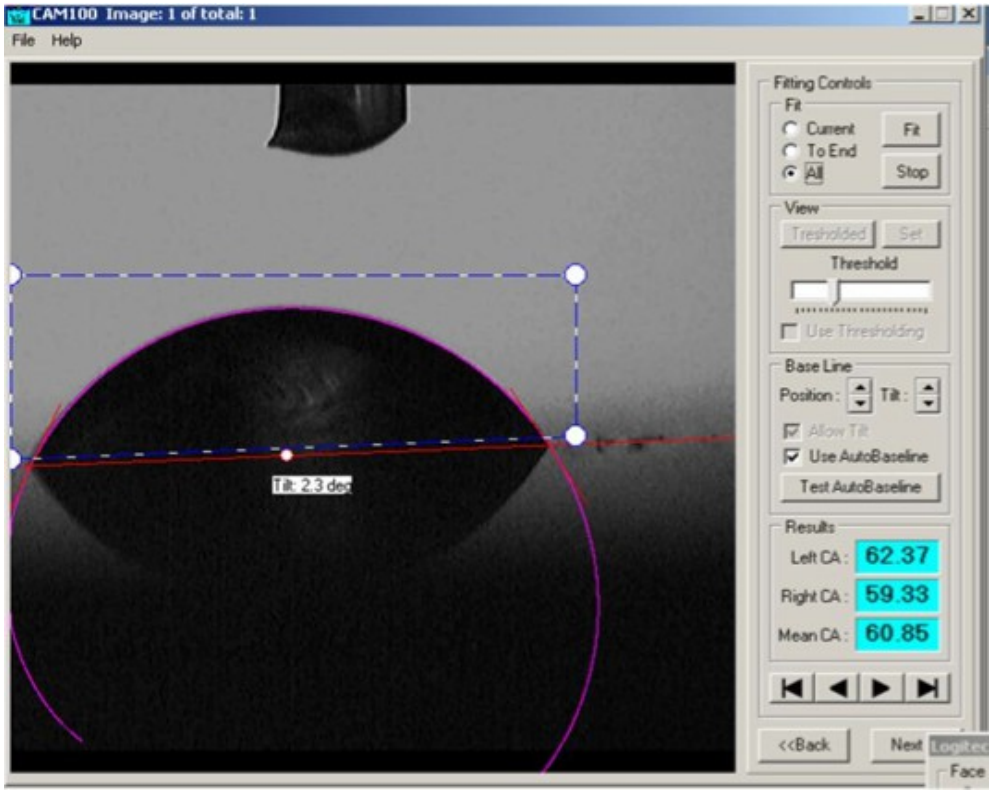

Fig. 56. Copper specimen polished (400 to 1500)

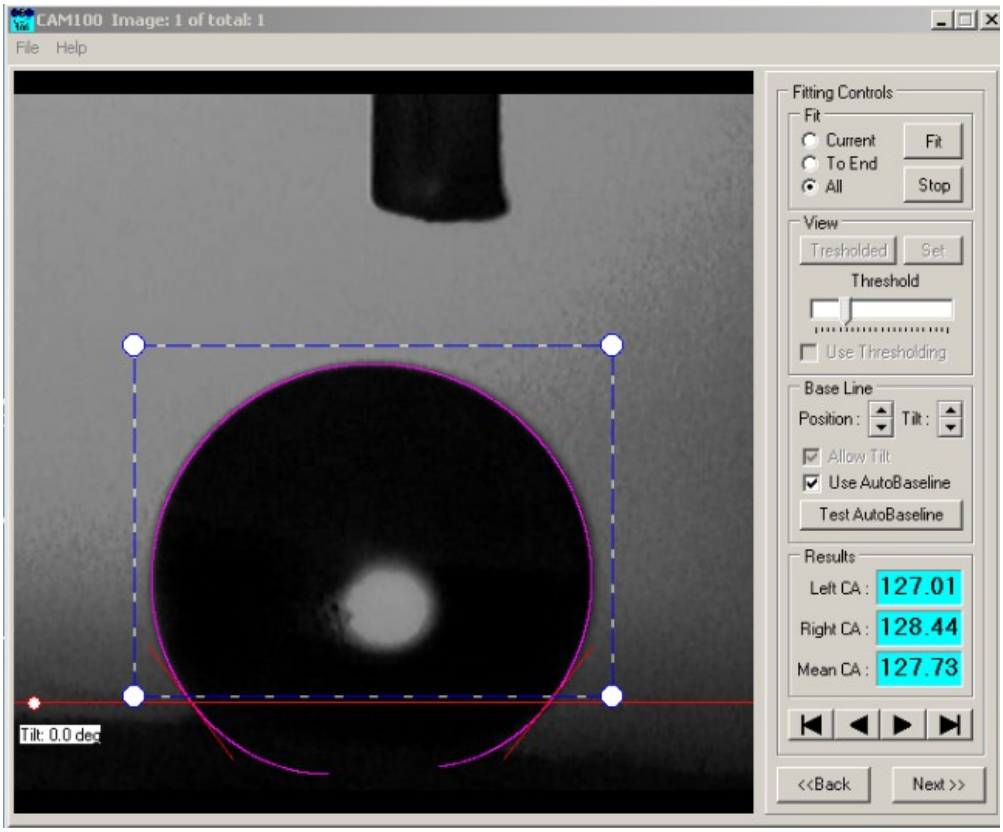

Fig. 57. Copper specimen with super-hydrophobic treatment for 3 days

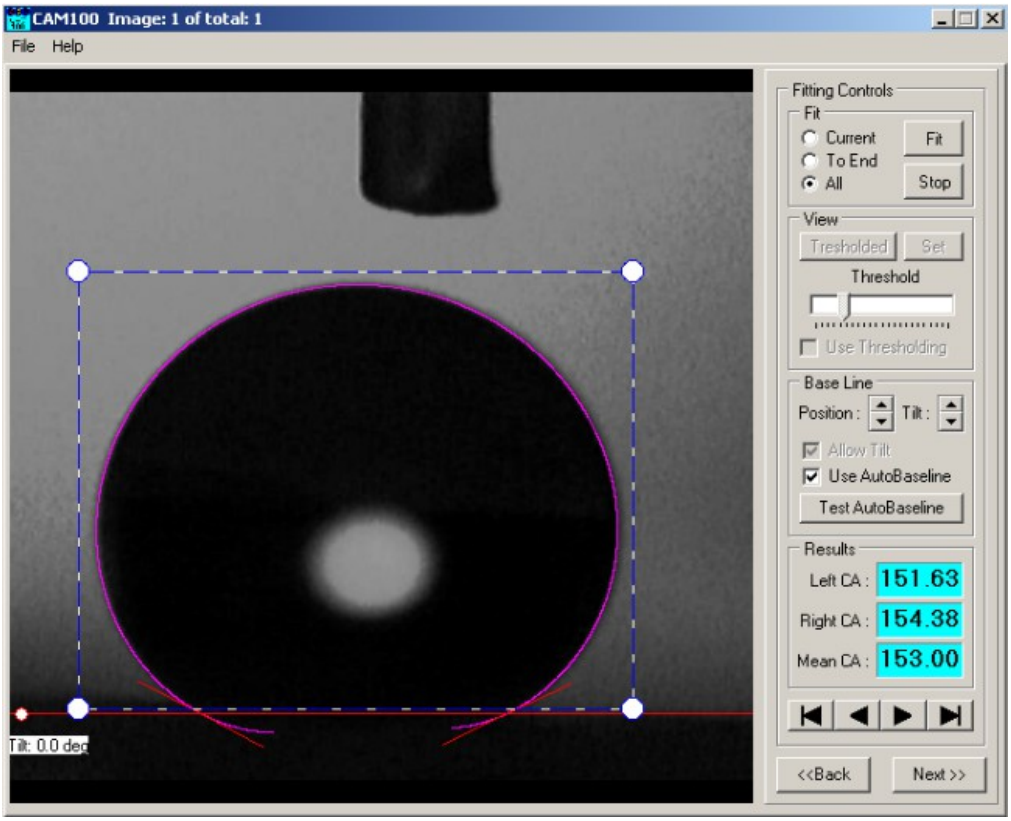

Fig. 58. Copper specimen with super-hydrophobic treatment for 6 days

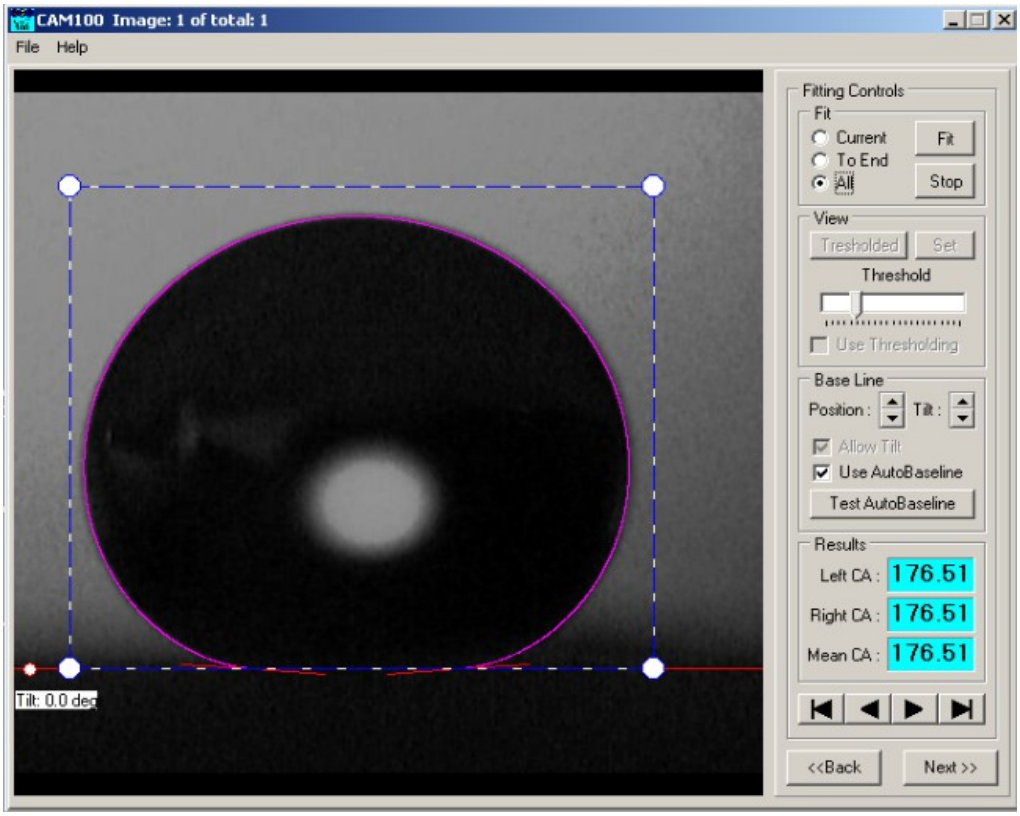

Fig. 59. Copper specimen with super-hydrophobic treatment for 10 days

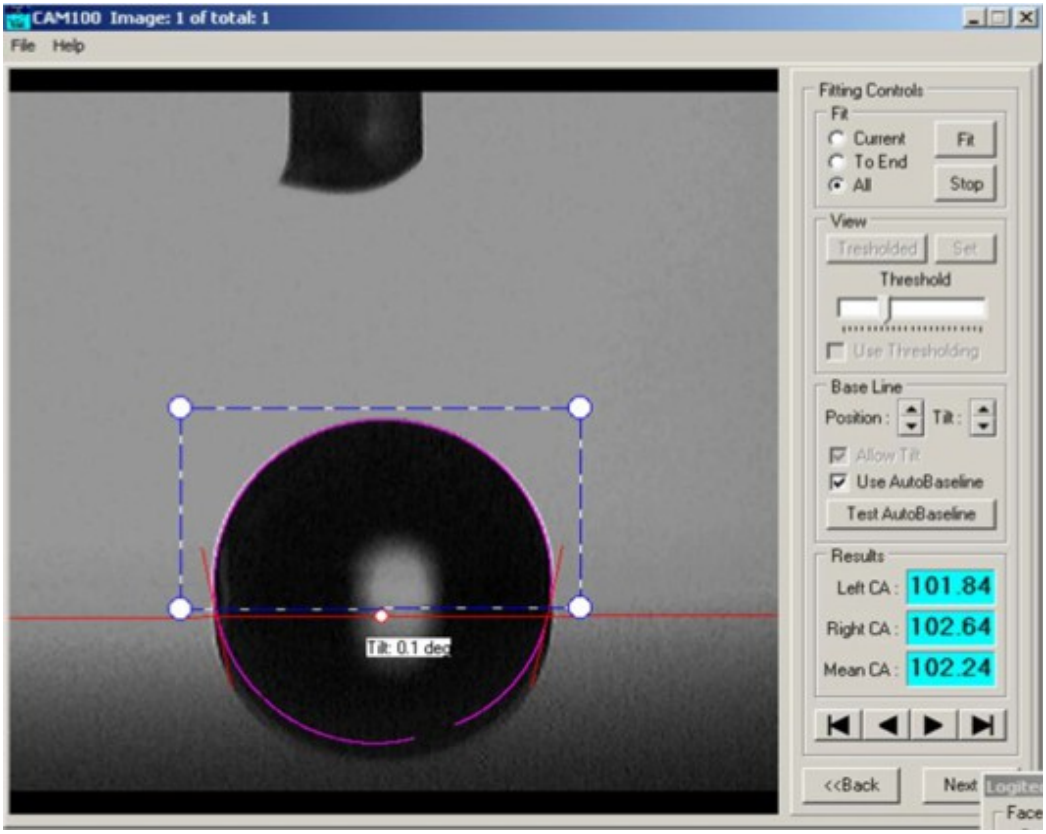

Fig. 60. Copper specimen with removed Super-hydrophobic coating

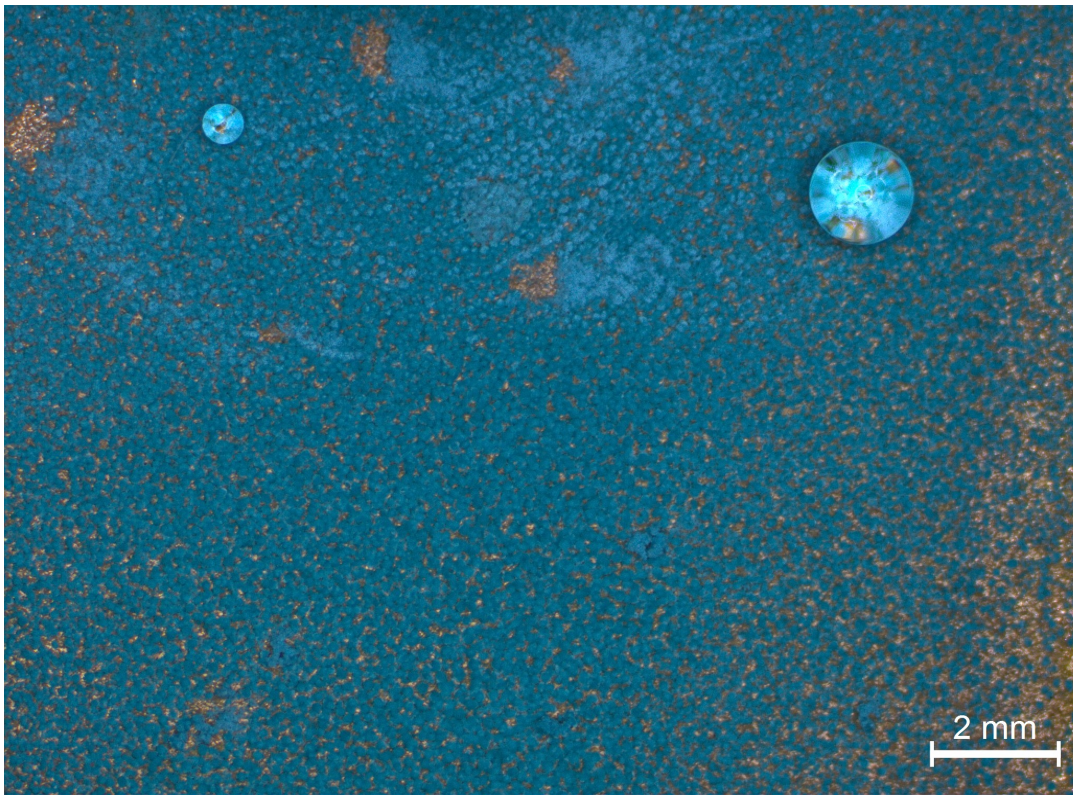

Fig. 61. Water droplets standing on the hydrophobic surface of the 3 days treated sample

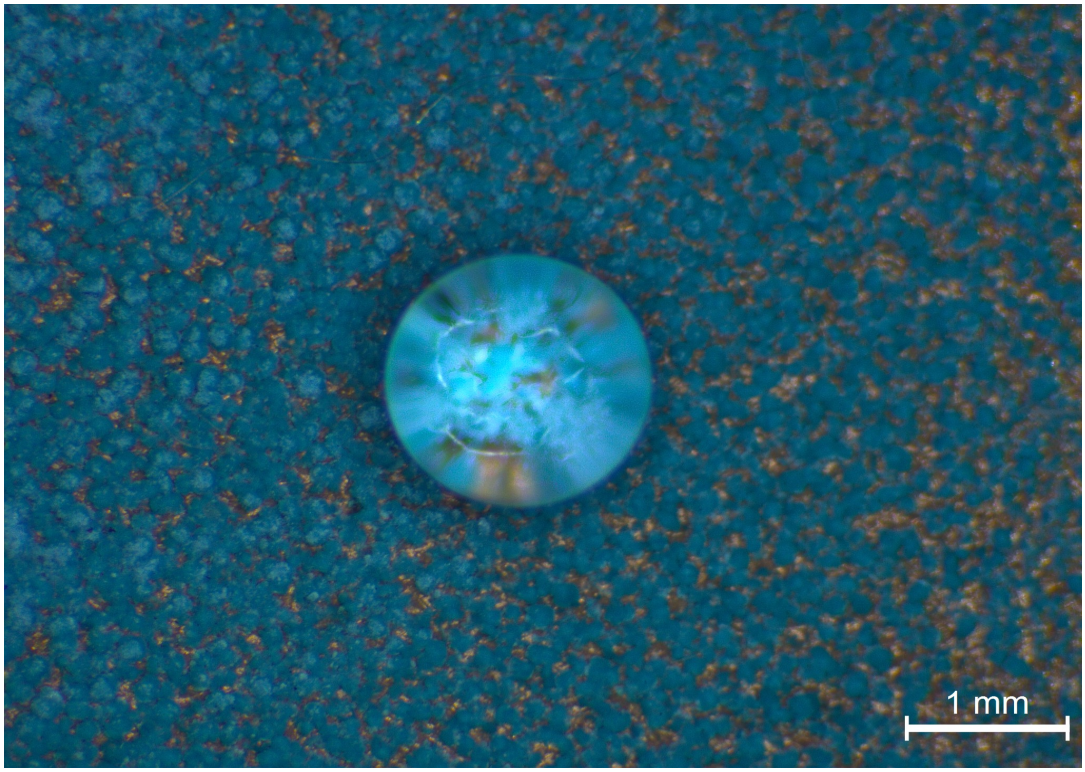

Fig. 62. Water droplet standing on the hydrophobic surface of the 3 days treated sample

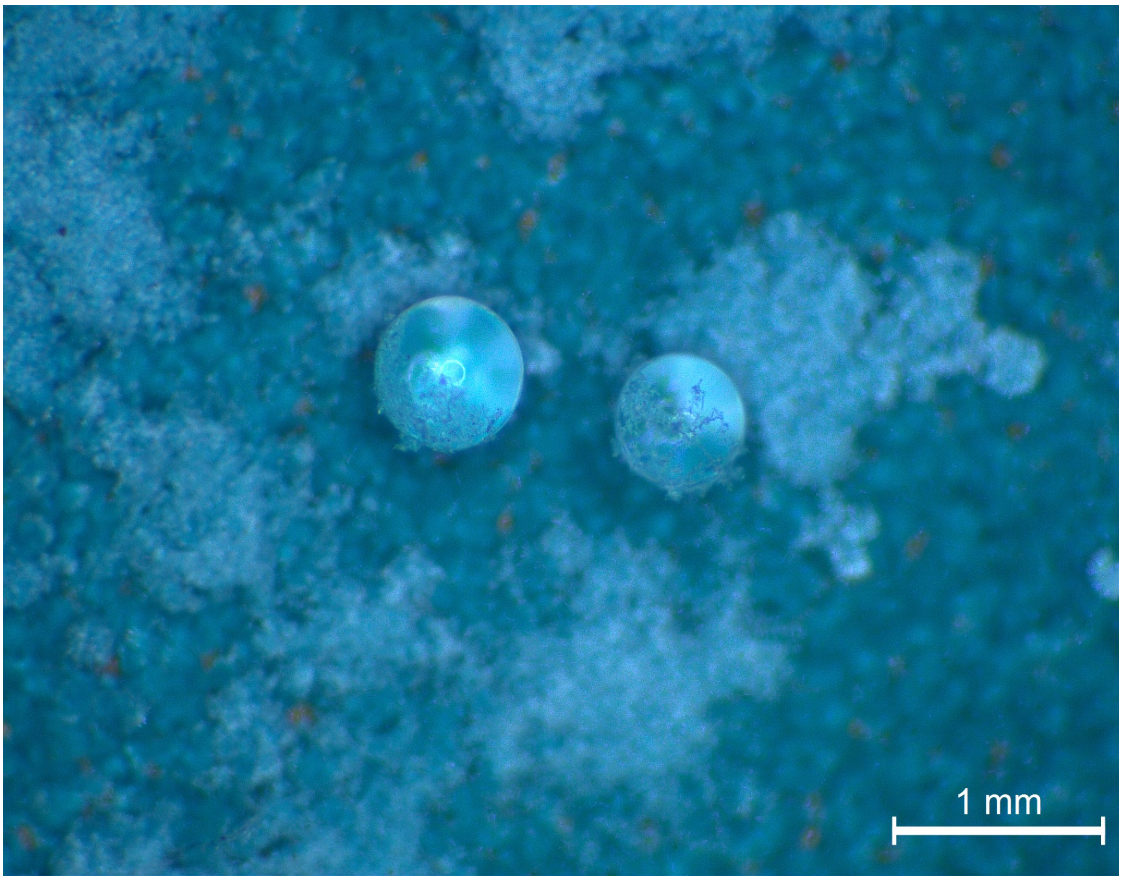

Fig. 63. Water droplets standing on the hydrophobic surface of the 6 days treated sample

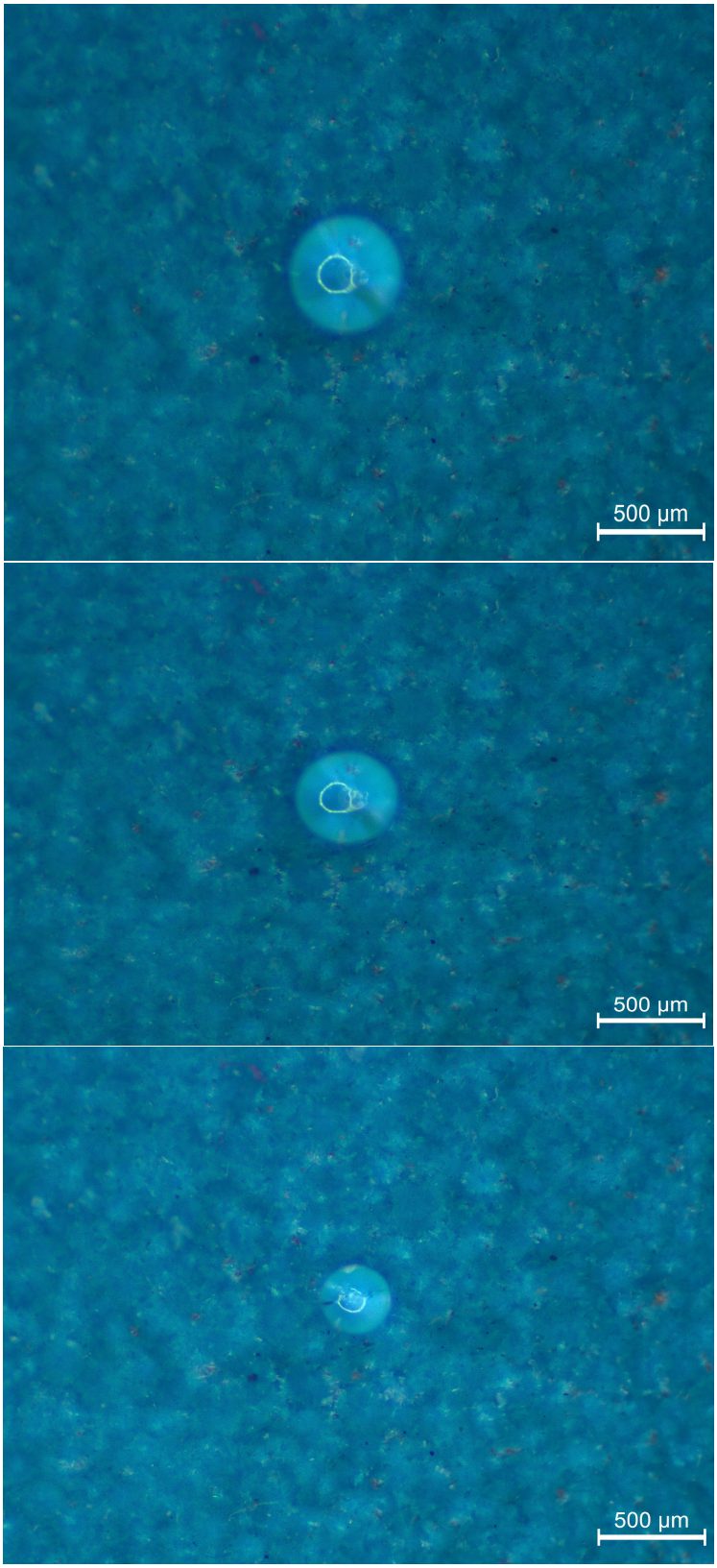

Fig. 64. Images showing the depression/compression of the droplet standing on the super-hydrophobic film of the 10 days treated copper specimen

6.4. Stereo Microscopy and Scanning Electron Microscopy

In order to evaluate the profile and structure of the treated surface we tried to apply Scanning Electron Microscopy and Stereo Microscopy . After the mounting and grinding (80 – 1500) process, the specimens were chemically modified in an ethanol solution of n-tetradecanoic acid 0.06M at room temperature for 3 days,for 6 days and for 10 days, in order to form a respective Super-hydrophobic film on the fresh copper surfaces, as we described above.

The new surfaces were observed with a Stereo Microscope.The "flowerlike structure" of the surfaces was shown in all SM images (Fig. 65-70). It is interesting to see the progress of the film during the passing of the immersion days, how the thickness increases and the density of the film reaches its ideal value. We can also observe some mountain and valley areas, which can be examined in a much more perspicuous way through the SEM.

The treated surfaces were then observed with a Scanning Electron Microscope. The images of the specimens surface morphology are shown in the SEM observations (Fig. 71-76), where the "flowerlike structure" of the surface is revealed clearly. Furthermore, it can be seen that the Cu surface becomes quite rough and develops "mountain-like" structure. We can observe some mountain and valley areas in Fig. 71-76. The "Mountain ridges" with a middle height of 150 nm, length 0.5–3 μm are homogeneously distributed over the whole sample surface. The two-tier scale of microscopic (as we observe the "flowerlike structure" in the Stereo microscope and SEM images), and nanoscopic (as we see the AFM image Fig. 79) roughness is typical for the Lotus leaf, showing Super-hydrophobic properties, and it is undisputed that a topography like this one is advantageous for the superhydrophobic effect.

It is well known that hierarchical surface architecture represents optimized structures for super- hydrophobic surfaces. Based on the data already known, we can describe two main superhydrophobic surface architectures for surfaces, the micropapillae with wax crystals (Lotus leaf) and micropapillae with cuticle folds (Viola petals). Some remarkable differences exist between the surface architecture of the lotus leaf and Viola petals. In Viola petals microstructures are larger (average height of 40.2 μm) than those of lotus leaves, which have microstructures with an average height of 15 μm. The nanofolds in Viola have an average thickness of 0.26 μm, while the wax tubules of lotus are only 100 nm thick and ~0.5–3 μm in length.

By combining the results of the SM, SEM and the AFM image we can tell that the structure of the n- tetradecanoic layer is a hierarchical structure, micro roughness covered with nano roughness, and specifically micropapillae with wax crystals like the Lotus leaf. That hierarchical structure was not only necessary to have high contact angle but also essential for the stability of the composite interface (water-solid and water- air).

This structure is suggested to provide the superior water –repellent properties, due to the air trapped in the gaps among the flower-like clusters and the sheets of the film. The super-hydrophobic film reduces the susceptibility of copper substrate to corrosion, by trapping the air in the voids and acting as a coating in the same time. This method can be considered as easily applied, time-saving and could contribute to the development of super-hydrophobic surfaces for improving the corrosion resistance of engineering materials.

We can also see a cross-section of the "mountain-like" structure. We tried to obtain images also of the cross section of the treated surface. We tried to cut the treated specimens in very low speed using diamond cutter mini-tom. Images of the cross section of specimens are presented in Fig 77-78. It seems like the treatment is destroyed and is difficult to obtain a clear image of both substrate and treatment.

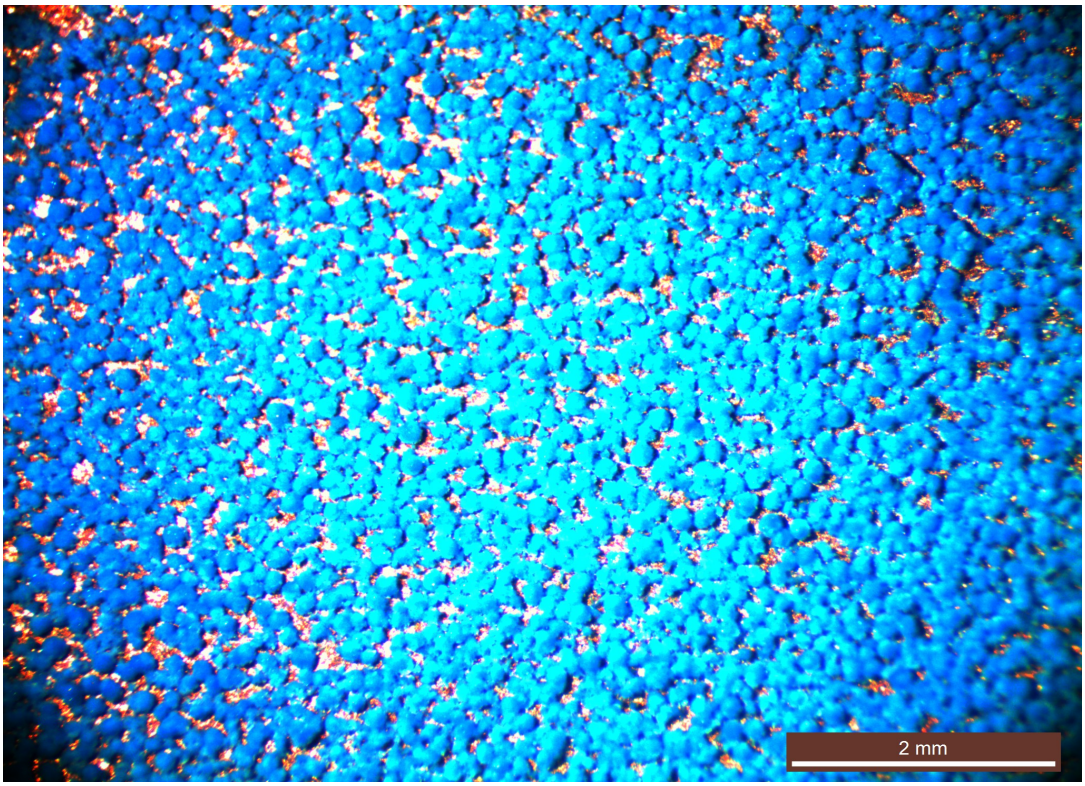

Fig. 65. SM image of the flowerlike structure on the chemically modified surface after 3 days of immersion time

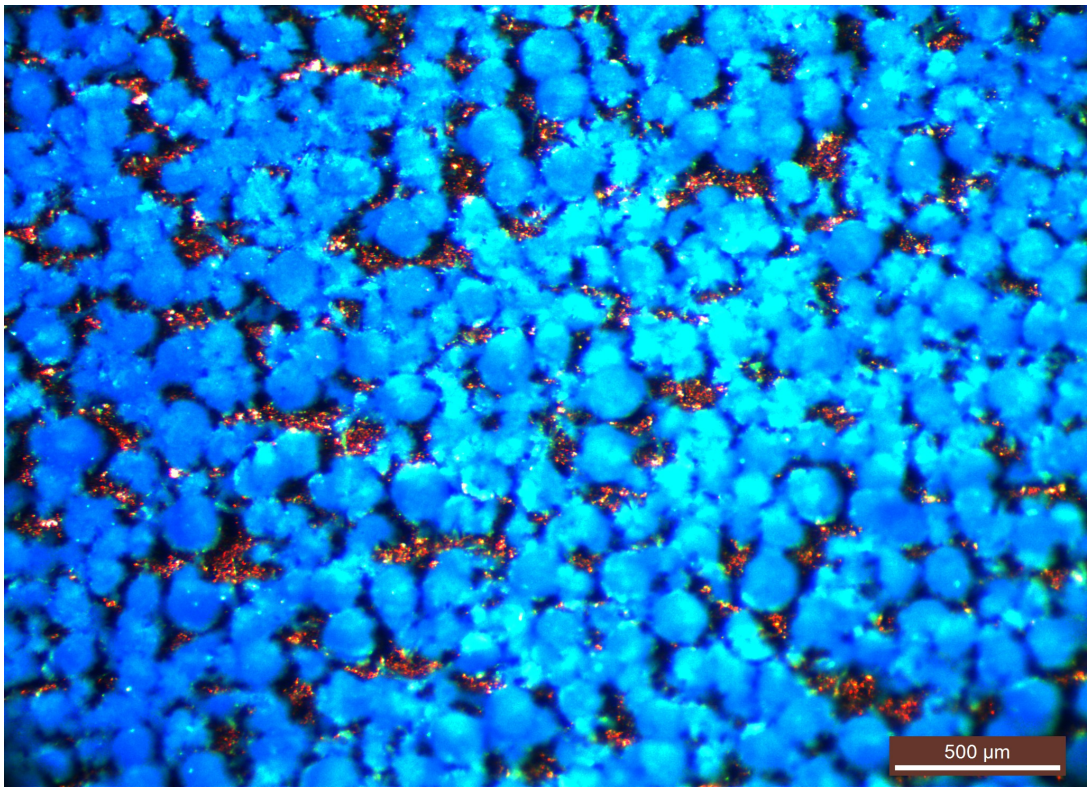

Fig. 66. SM image of the flowerlike structure on the chemically modified surface after 3 days of immersion time

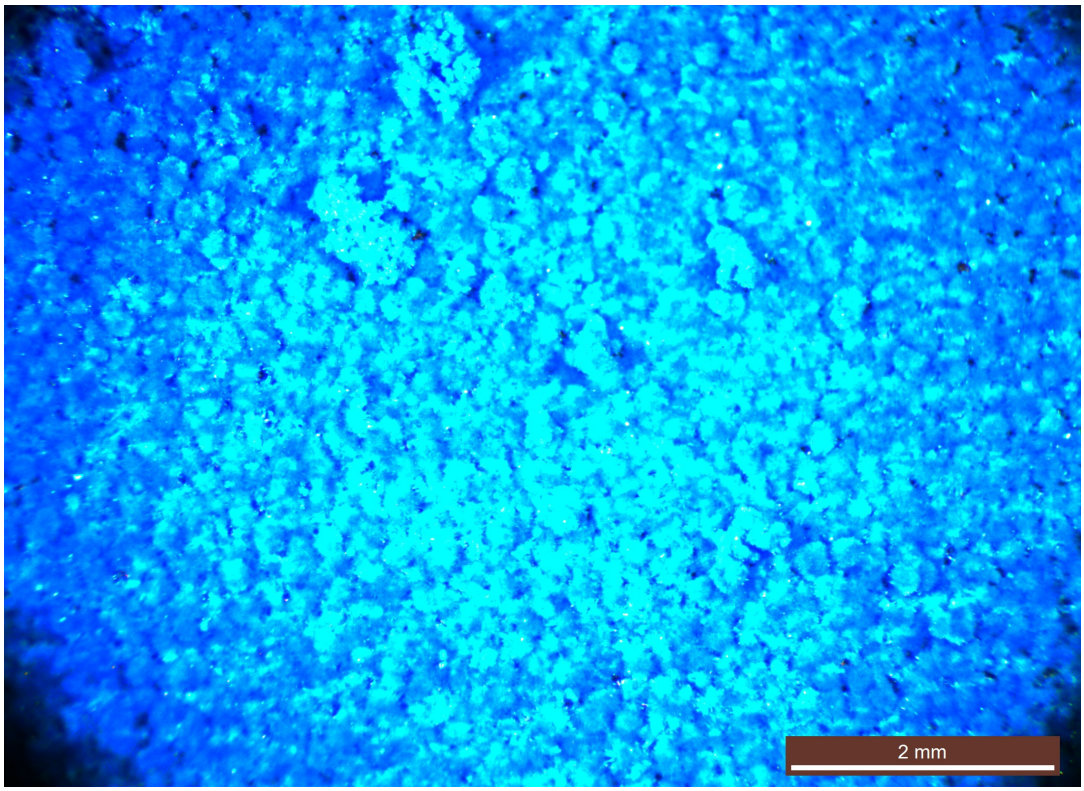

Fig. 67. SM image of the flowerlike structure on the chemically modified surface after 6 days of immersion time

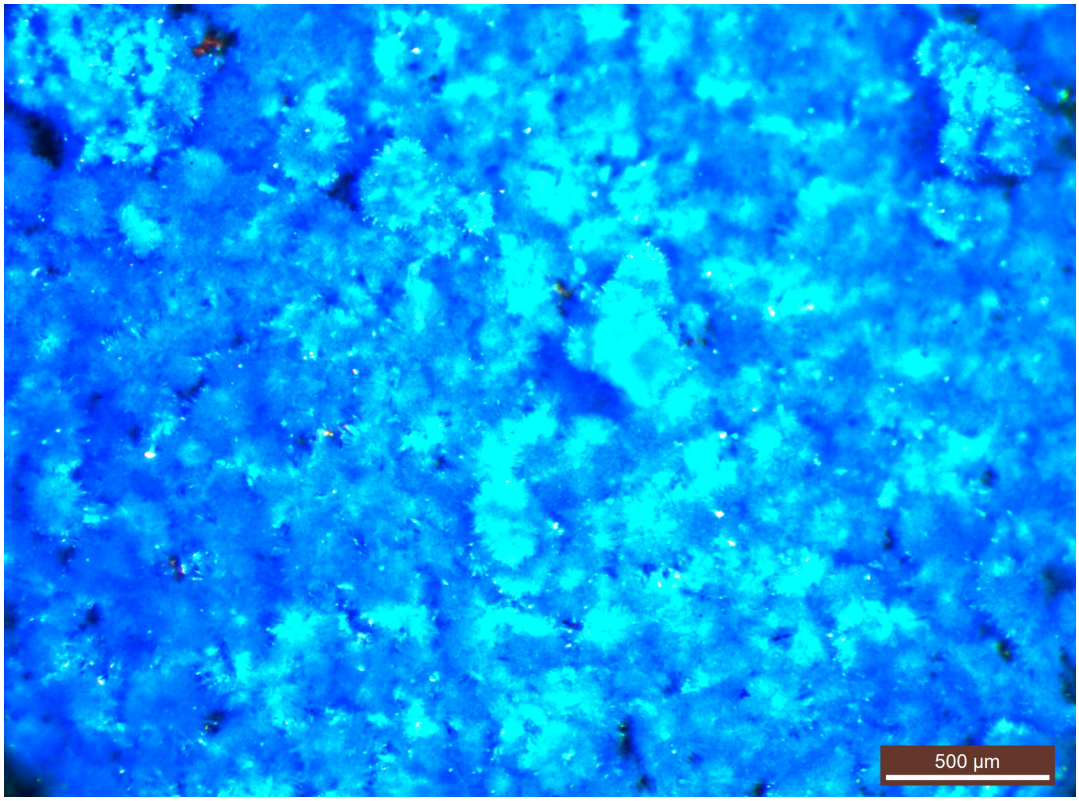

Fig. 68. SM image of the flowerlike structure on the chemically modified surface after 6 days of immersion time

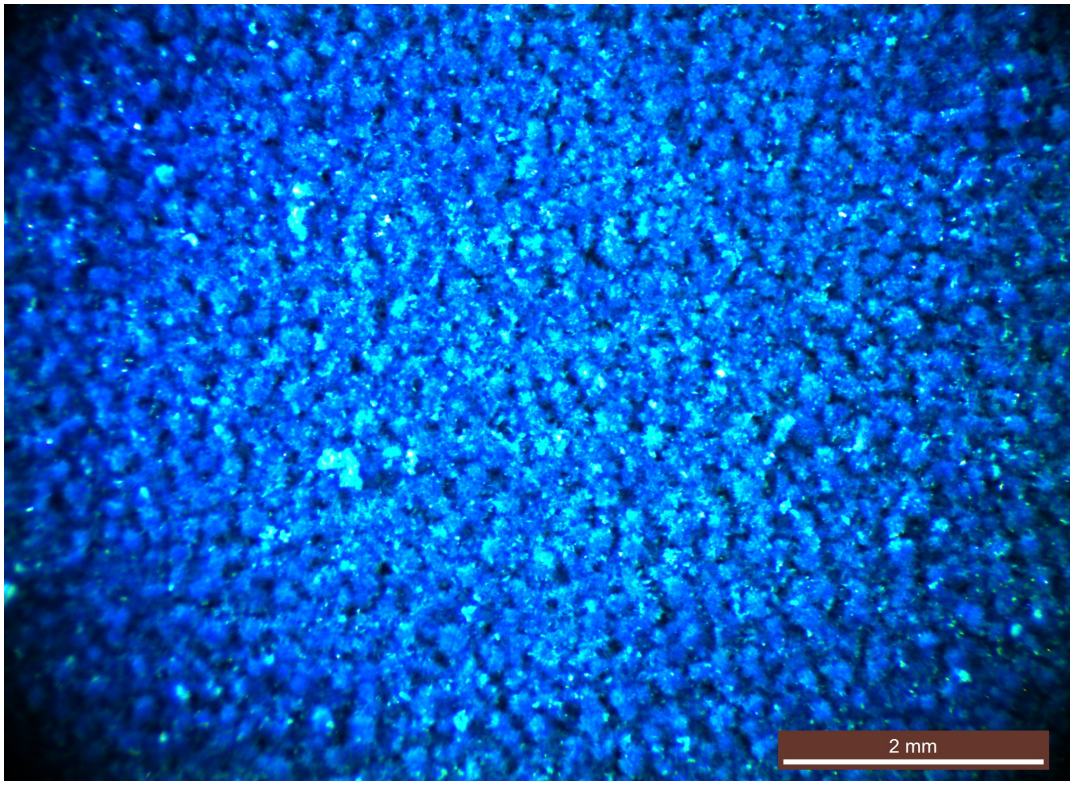

Fig. 69. SM image of the flowerlike structure on the chemically modified surface after 10 days of immersion time

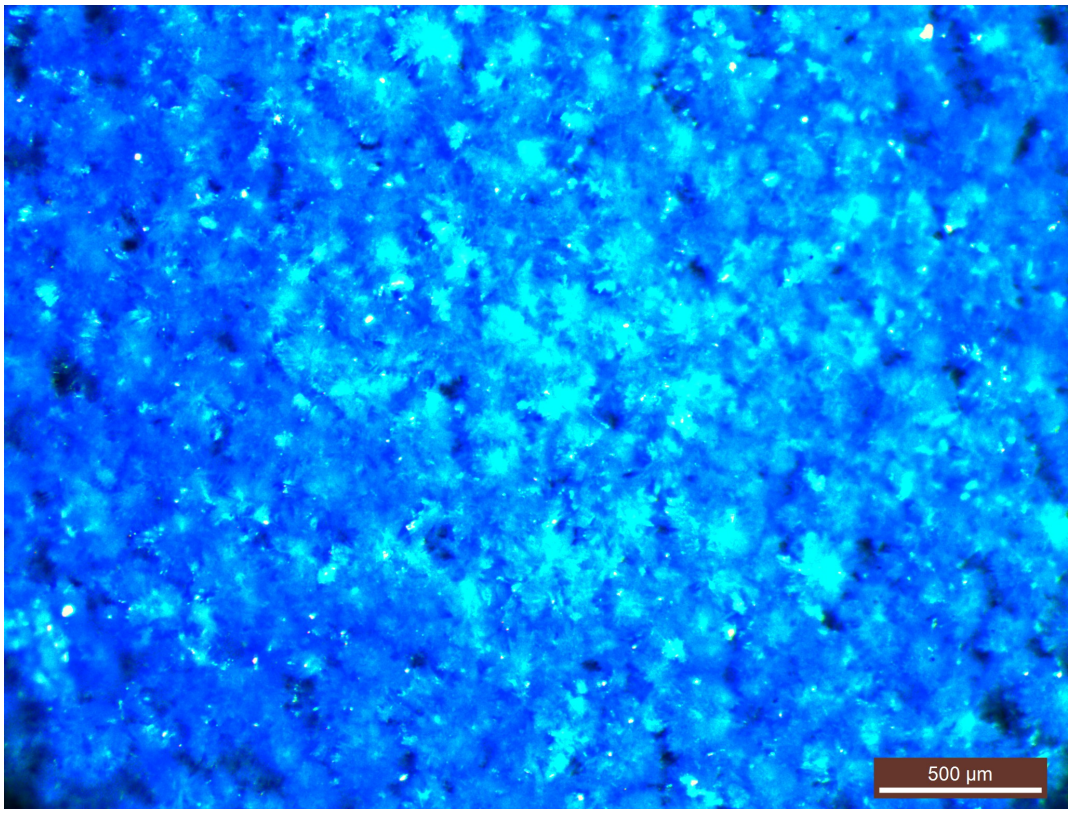

Fig. 70. SM image of the flowerlike structure on the chemically modified surface after 10 days of immersion time

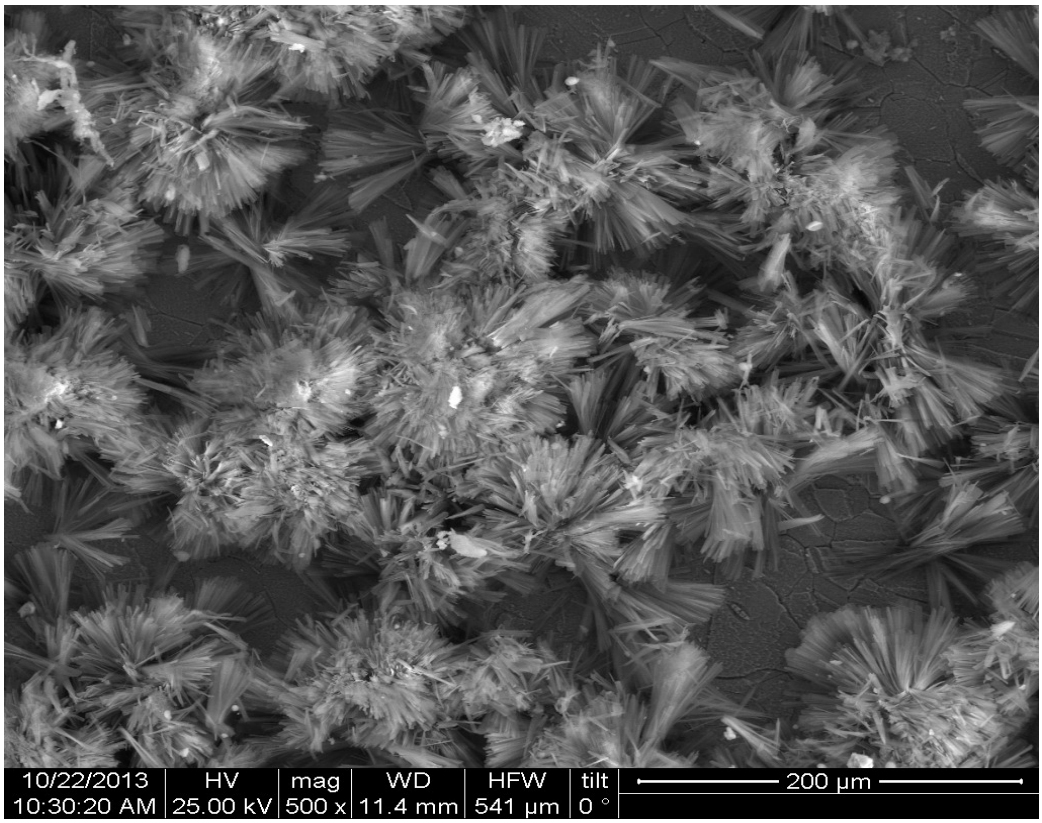

Fig. 71. Flowerlike structure on the chemically modified surface after 3 days of immersion time, SEM image x500

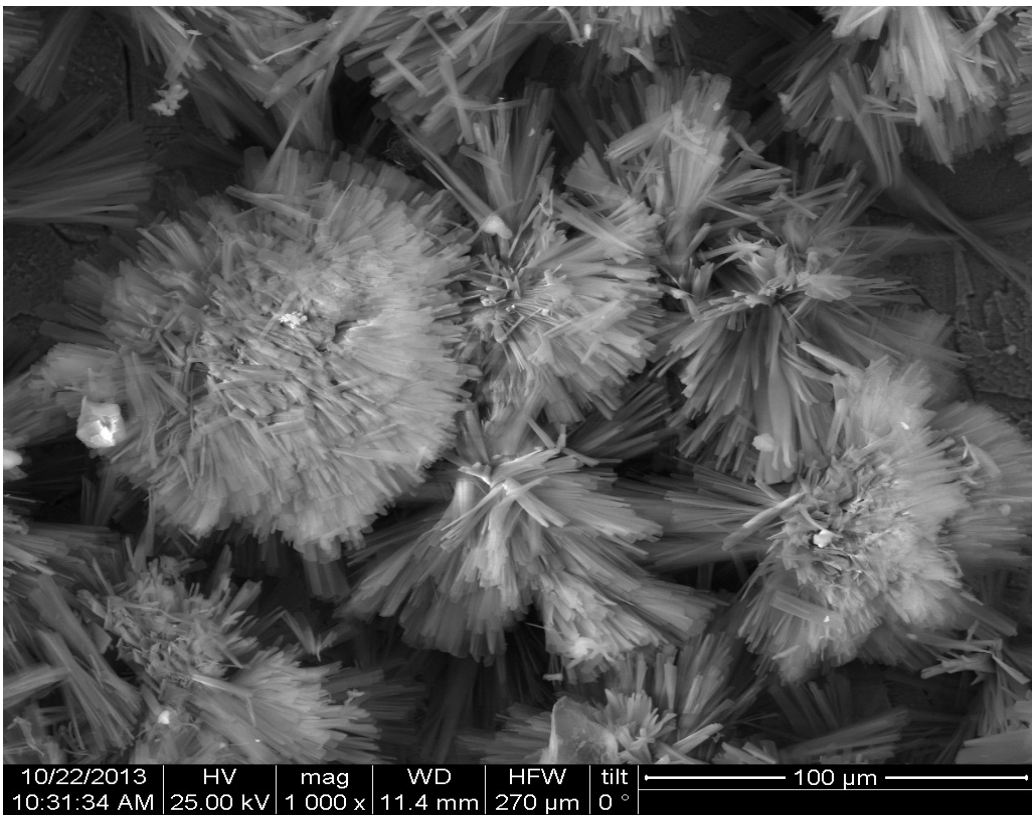

Fig. 72. Flowerlike structure on the chemically modified surface after 3 days of immersion time, SEM image x1000

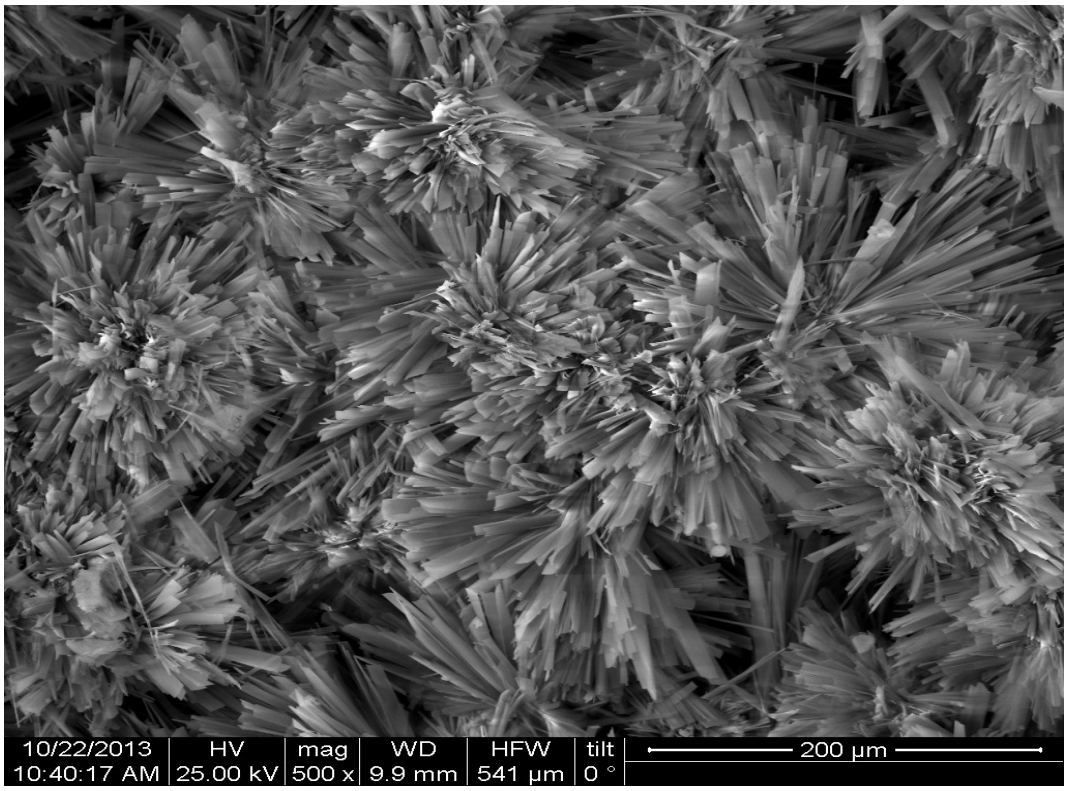

Fig. 73. Flowerlike structure on the chemically modified surface after 6 days of immersion time, SEM image x500

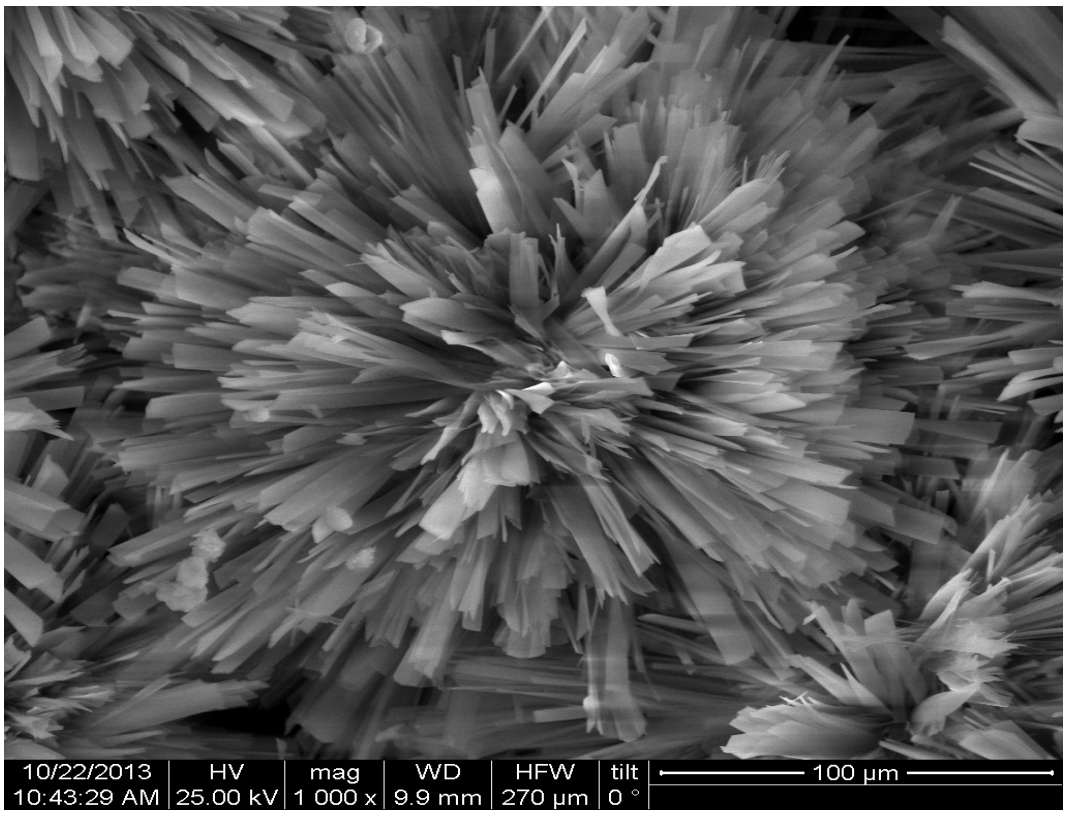

Fig. 74. Flowerlike structure on the chemically modified surface after 6 days of immersion time, SEM image x1000

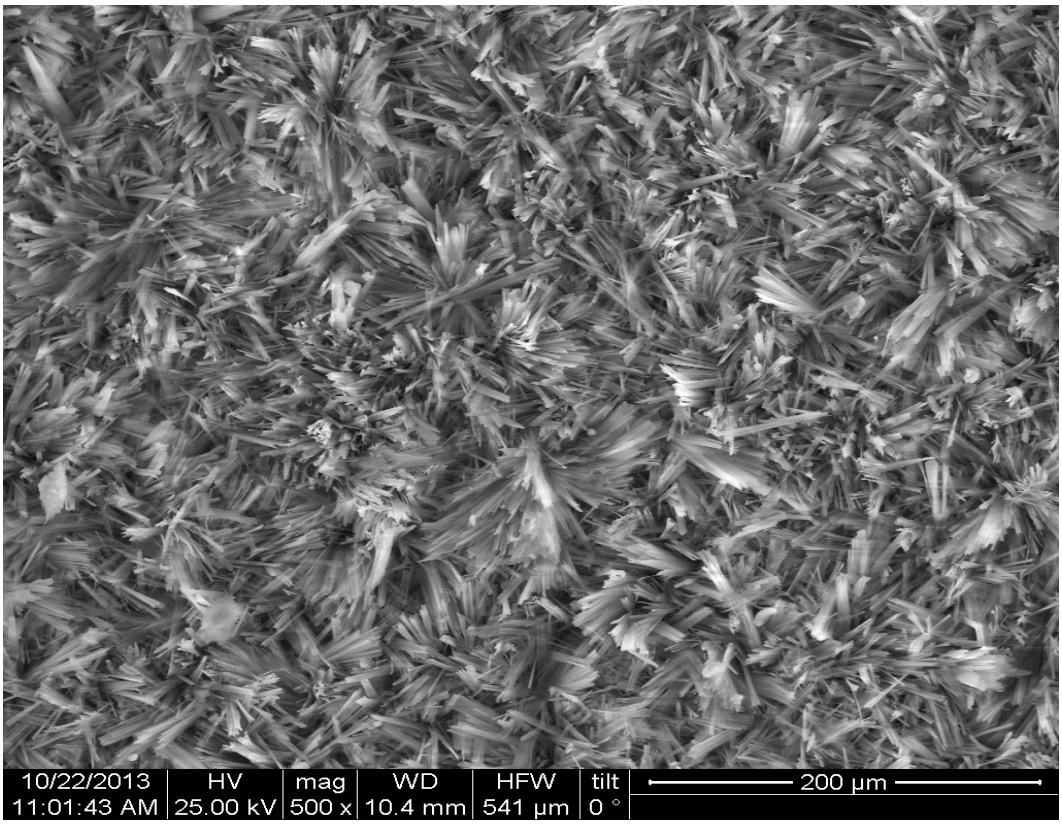

Fig. 75. Flowerlike structure on the chemically modified surface after 10 days of immersion time, SEM image x500

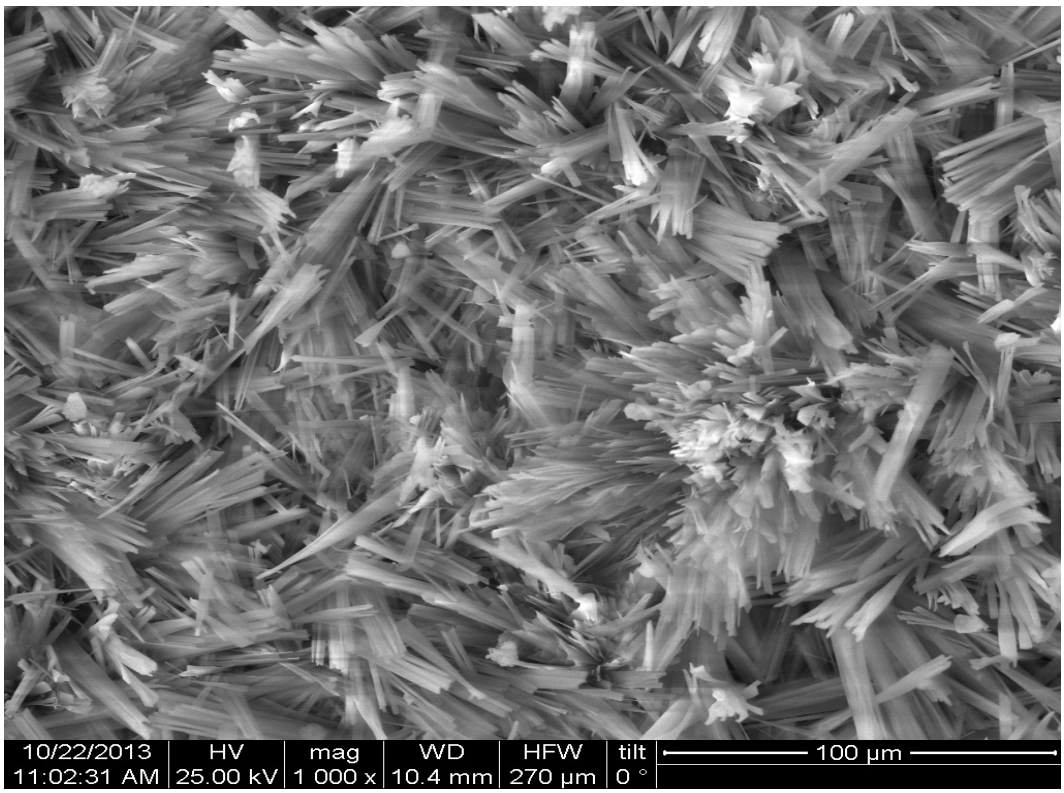

Fig. 76. Flowerlike structure on the chemically modified surface after 10 days of immersion time, SEM image x1000

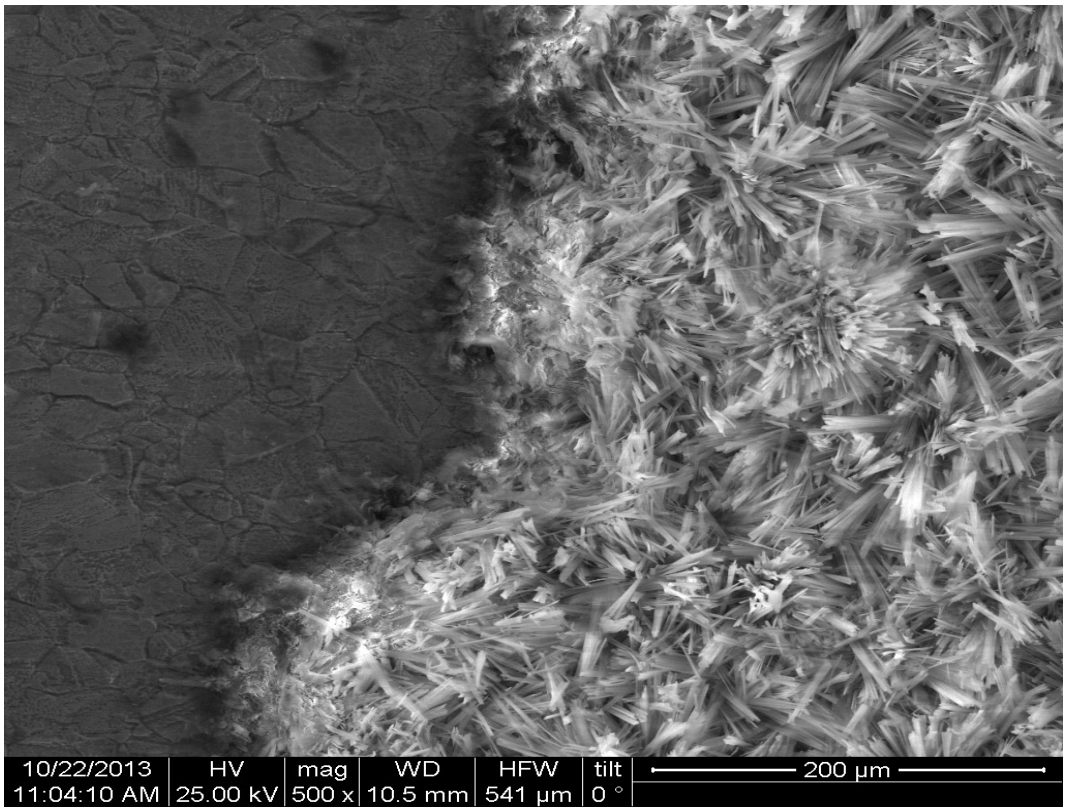

Fig. 77. Cross-section of a chemically modified specimen

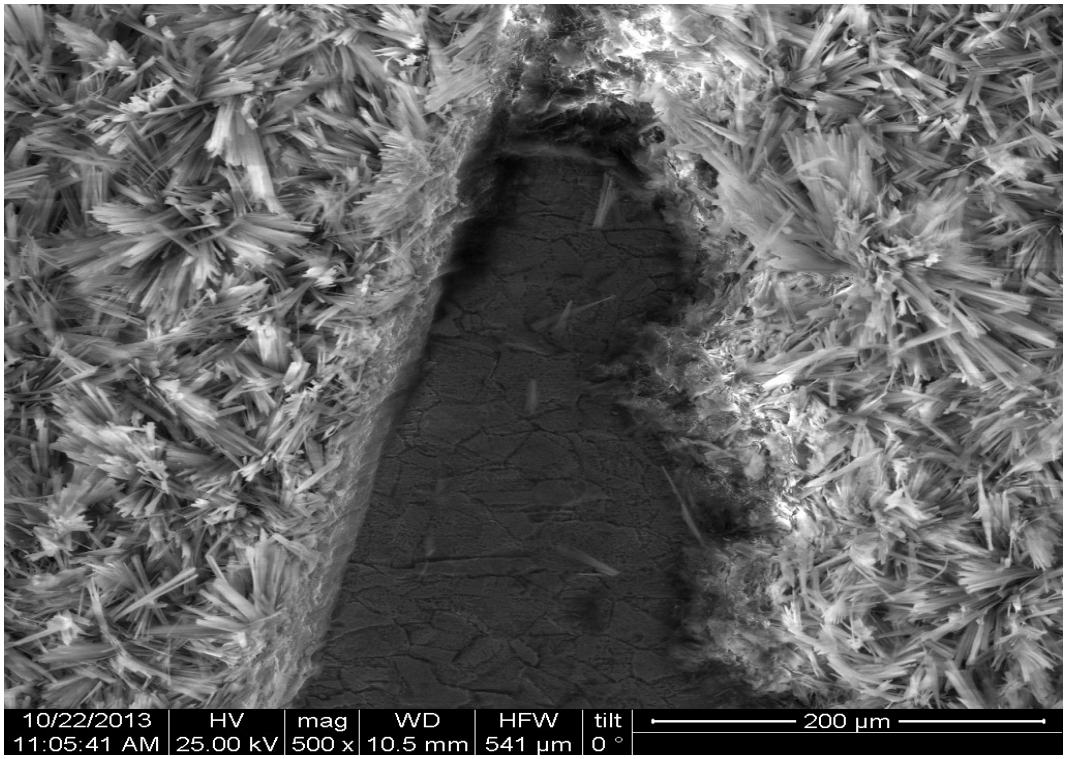

Fig. 78. Cross-section of a chemically modified specimen

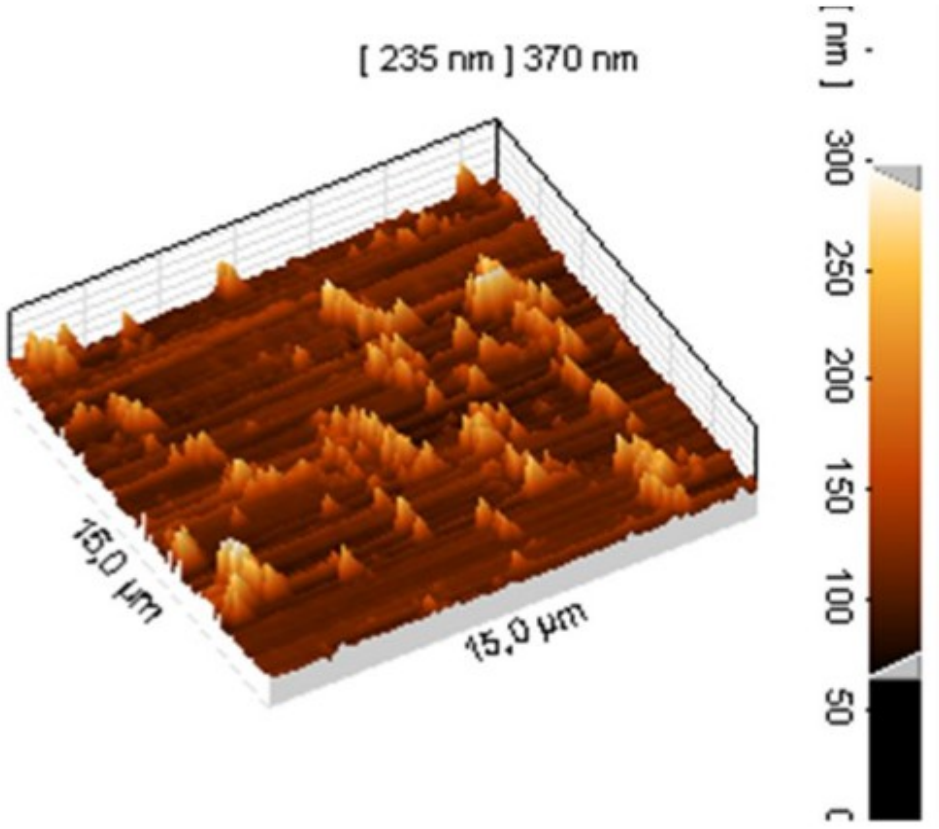

Fig.79. A 3D image, of the “mountain-like” structure, of Super-hydrophobic film on the fresh copper surface

6.5. Electrochemical Experiments

We conducted two sets of electrochemical measurements. One set with Open Circuit measurements, which were followed by Potentiodynamic polarization measurements. The open circuit measurements were applied mainly to obtain a stable potential for the Potentiodynamic Polarization measurements.

The working cell was a standard three-electrode cell, having a Pt net as a counter electrode and Saturated Calomel Electro (SCE) as reference electrode. Working solutions prepared at room temperature were 3,5% NaCl (0.6M, ph~6-7). We studied two different types of specimens: the pure electrolytic tough pitch copper substrates and the chemically modified substrates with the Super-hydrophobic film.

For the first substrate category the results of electrochemical measurements were taken after the mounting and grinding (up to 1500 SiC) process. For the second substrate category the specimens mounted, grinded (up to 1500 SiC), and immersed in an ethanol solution of n-tetradecanoic acid 0.06M at room temperature for 3 days, 6 days and 10 days.

6.5.1. Open Circuit Experiments

In the Open Circuit set we run eight (8) experiments, each had 40000 sec (~11 hours) duration. The Average Potential calculated after the first 10000 seconds, for better stabilization of potential. The measurements of the experiments are presented in the following Table 2.

OPEN CICUIT			
Experiment	Type of Experiment	Average Potential (mV)	Average Potential per type of specimen (mV)
Peirama A	*Bare*	*-269.83*	*-264.63*
Peirama B	*Bare*	*-259.43*	
Peirama C	*3 days*	*-221.59*	*-221.39*
Peirama D	*3 days*	*-221.19*	
Peirama E	*6 days*	*-207.04*	*-207.89*
Peirama F	*6 days*	*-208.74*	
Peirama G	*10 days*	*-170.85*	*-165.04*
Peirama H	*10 days*	*-159.23*	

Table. 2. Open Circuit Measurements

The open circuit value for bare copper was -0,2646 V, which is in accordance to the literature ~250mV. Reading the values of the Open Circuit Experiment Table we can conclude that the potential developed is much smaller for all the treated specimens. The potential is decreased slightly for the 3 day immersed specimens, but greatly for the 10 day and quite big for the 6 day as well. The potential decrease is solid proof that super-hydrophobic copper specimens we produced present thermodynamics susceptibility to corrosion.

The curves for open circuit experiments are presented in Figs 80-87.

Trying to explain the phenomenon that takes place when the clean copper specimen is immersed into the NaCl 3.5% solution we can observe the following. When the copper specimen is immersed in the NaCl solution CuCl is formed, strongly adhered to the surface.

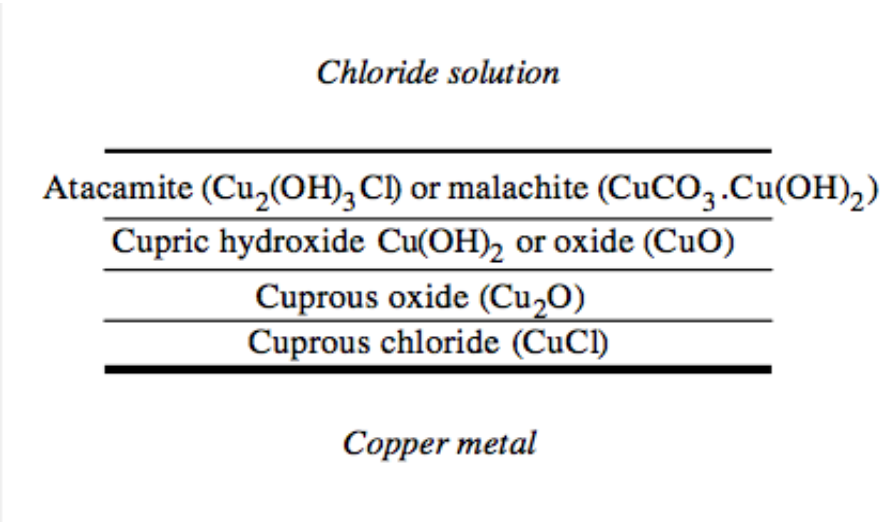

Fig. 88. General stratification scheme of species in a mature copper corrosion product film in seawater

It was proposed that the cuprous chloride, which is only slightly soluble in dilute sodium chloride, reacts to produce cuprous oxide (cuprite) which was the main constituent of thick scales . The cuprous oxide was generally oxidized over time to cupric hydroxide ($Cu(OH)_2$), atacamite ($Cu_2OH)_3Cl$) or malachite($CuCO_3Cu(OH)_2$) in the presence of seawater. It was predicted that if the chemical nature of scale formation is considered only as a function of oxygen supply, a general stratification of corrosion products for a mature film, as shown in Fig. 88, should be observed.

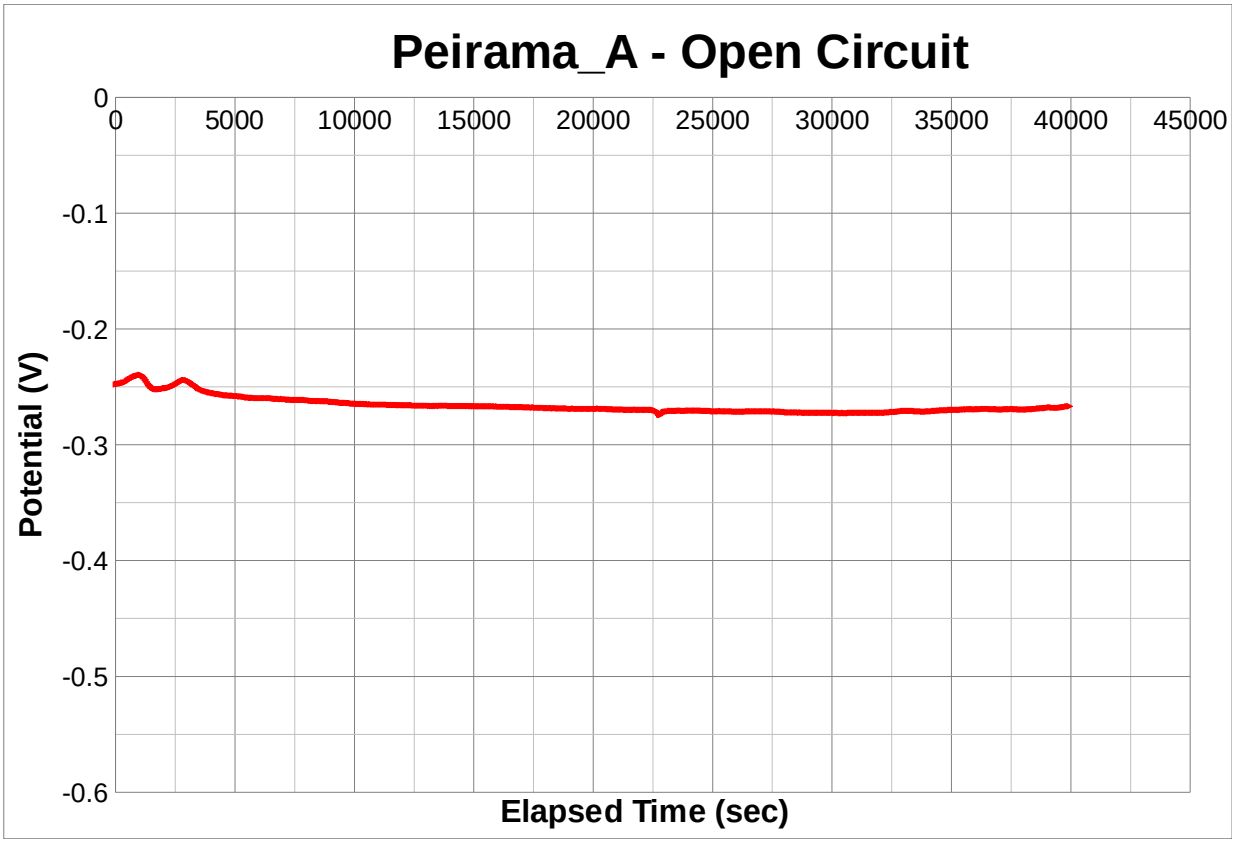

Fig. 80. Peirama_A- Bare copper surface- Open Circuit Curve

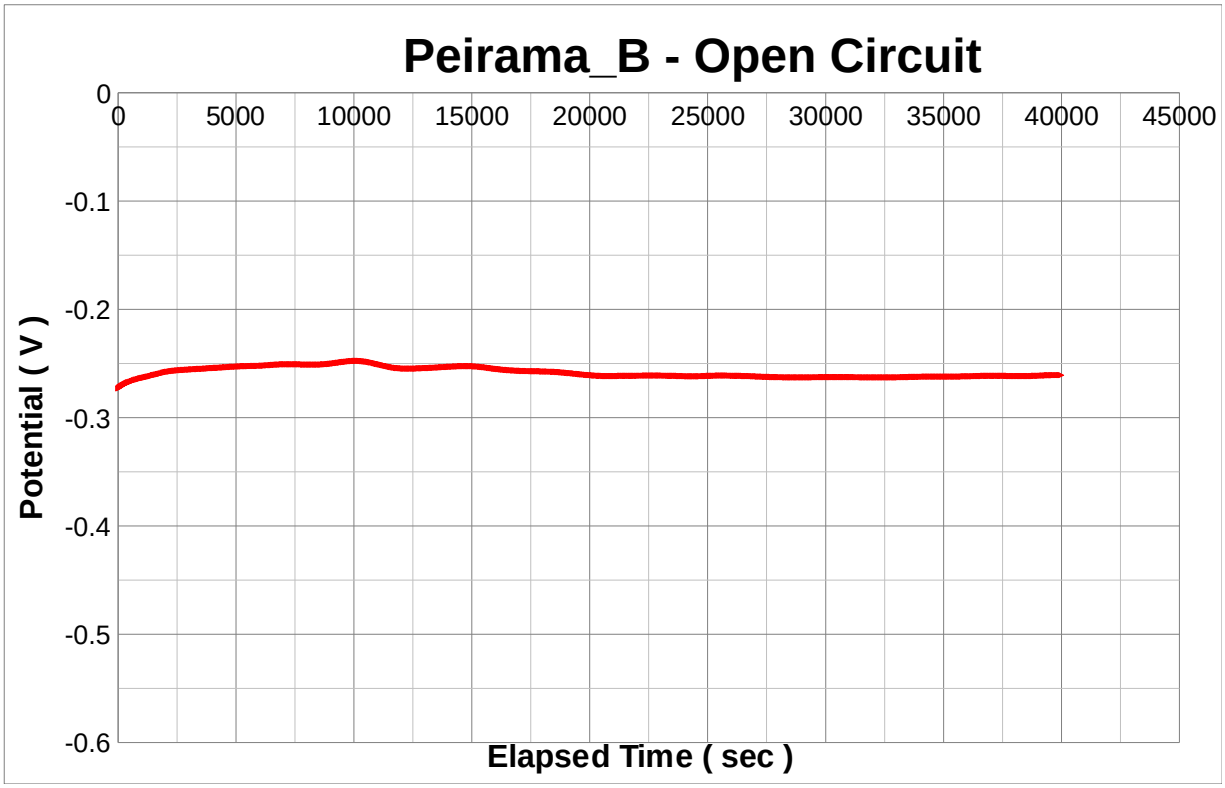

Fig. 80. Peirama_B- Bare copper surface- Open Circuit Curve

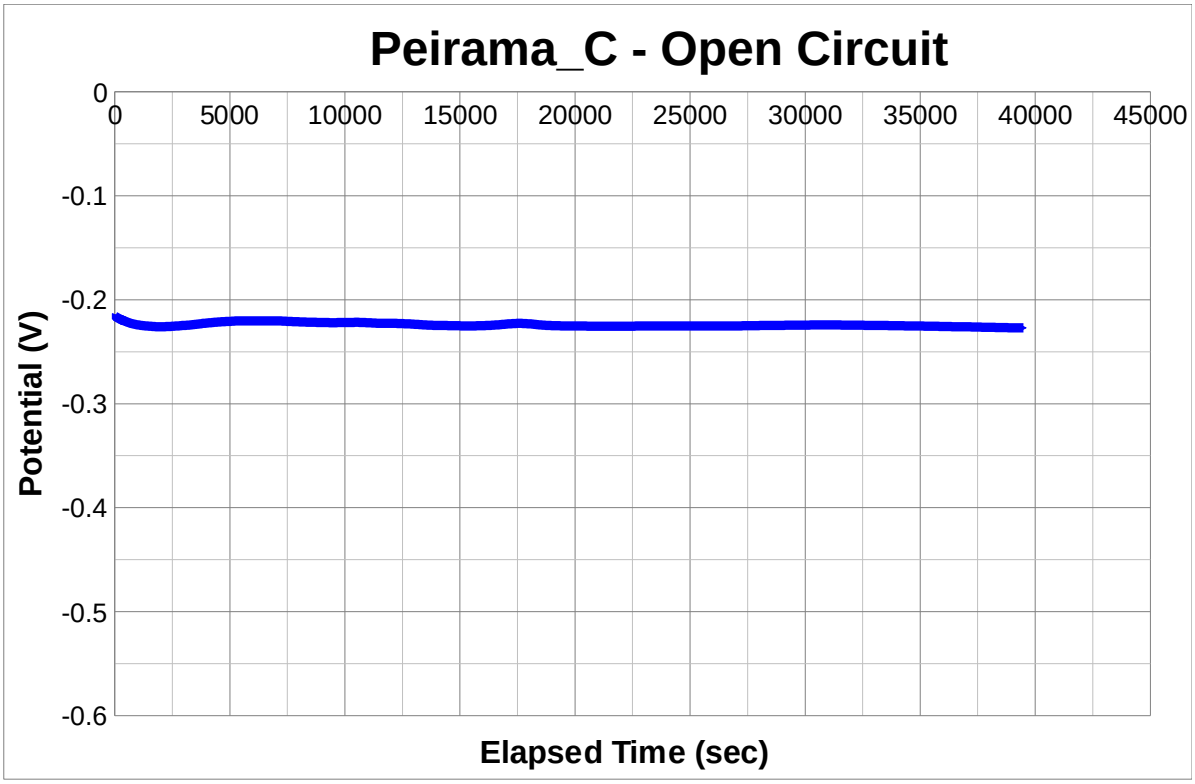

Fig. 81. Peirama_C- Treated copper surface for 3 days- Open Circuit Curve

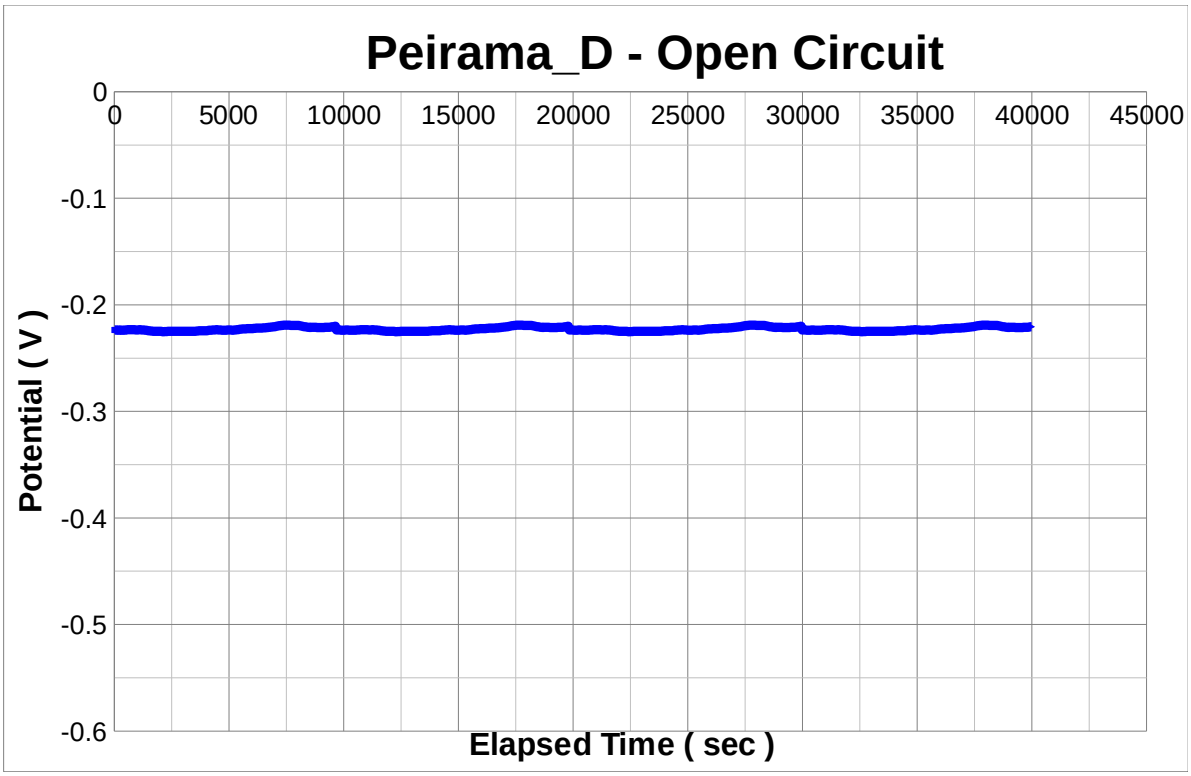

Fig. 82. Peirama_D- Treated copper surface for 3 days- Open Circuit Curve

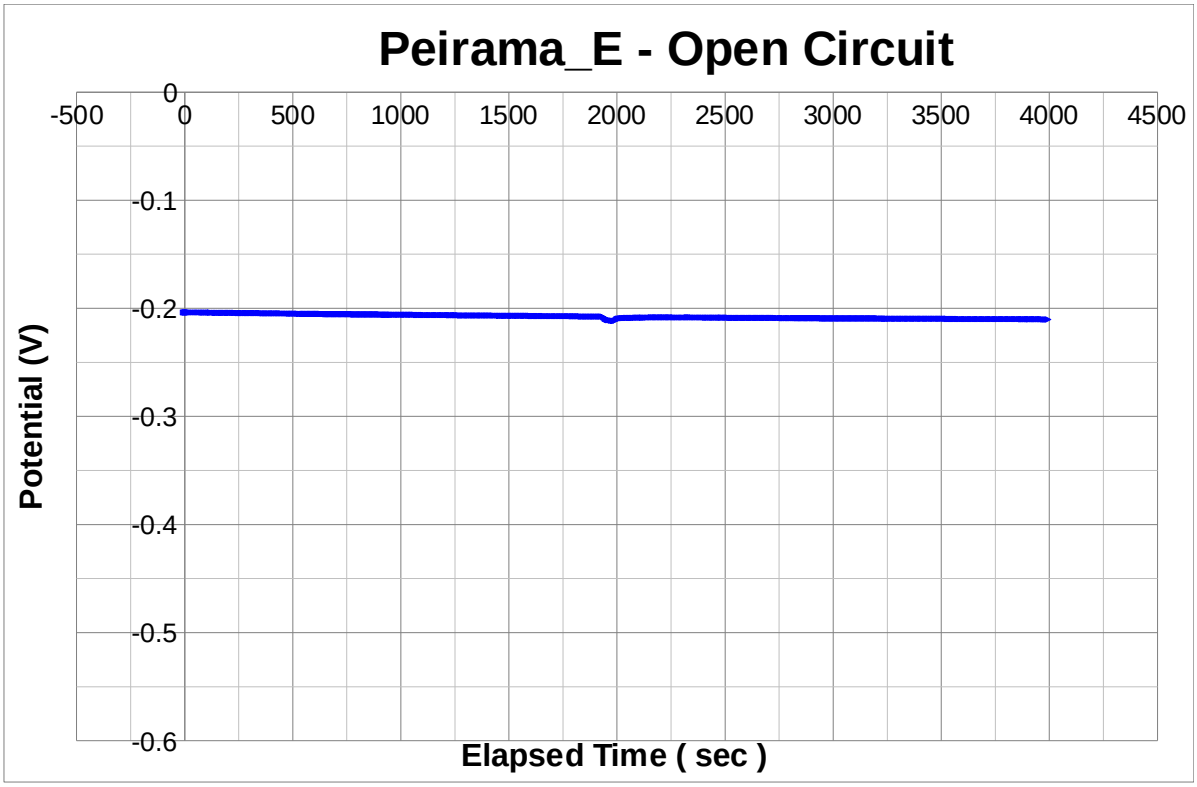

Fig. 83. Peirama_E- Treated copper surface for 6 days- Open Circuit Curve

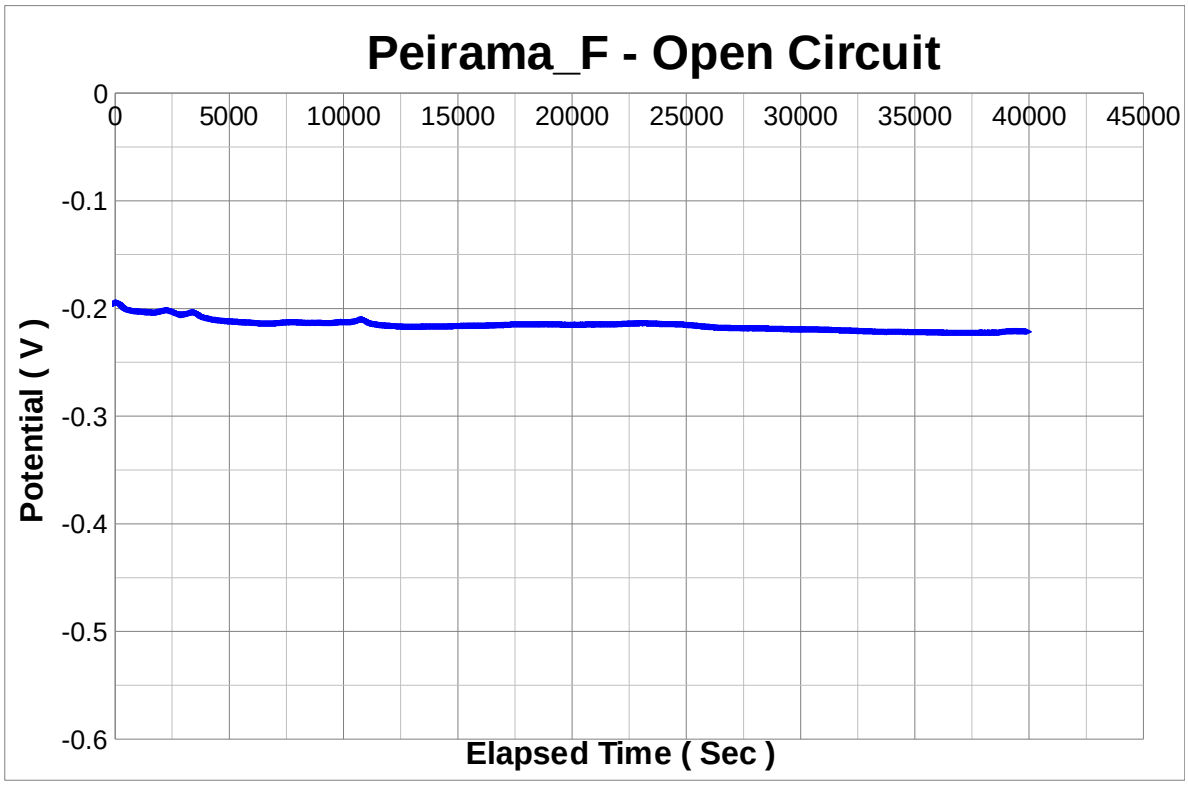

Fig. 84. Peirama_F- Treated copper surface for 6 days- Open Circuit Curve

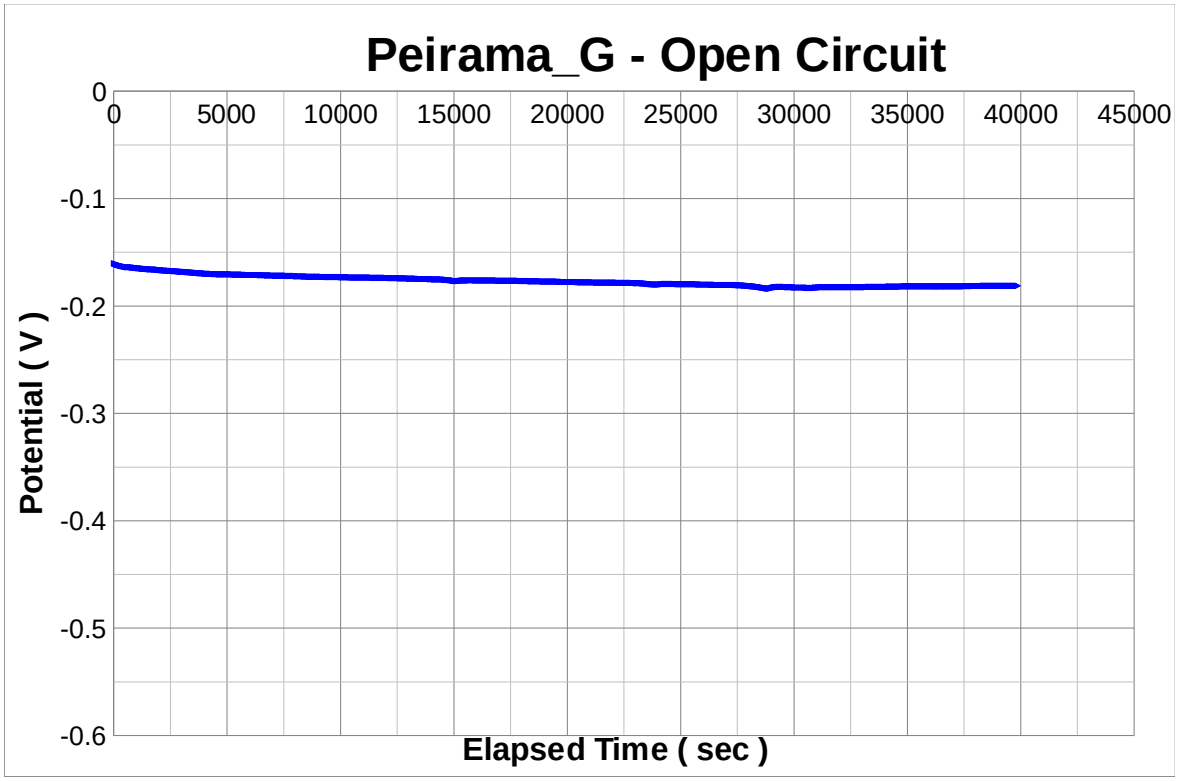

Fig. 85. Peirama_G- Treated copper surface for 10 days- Open Circuit Curve

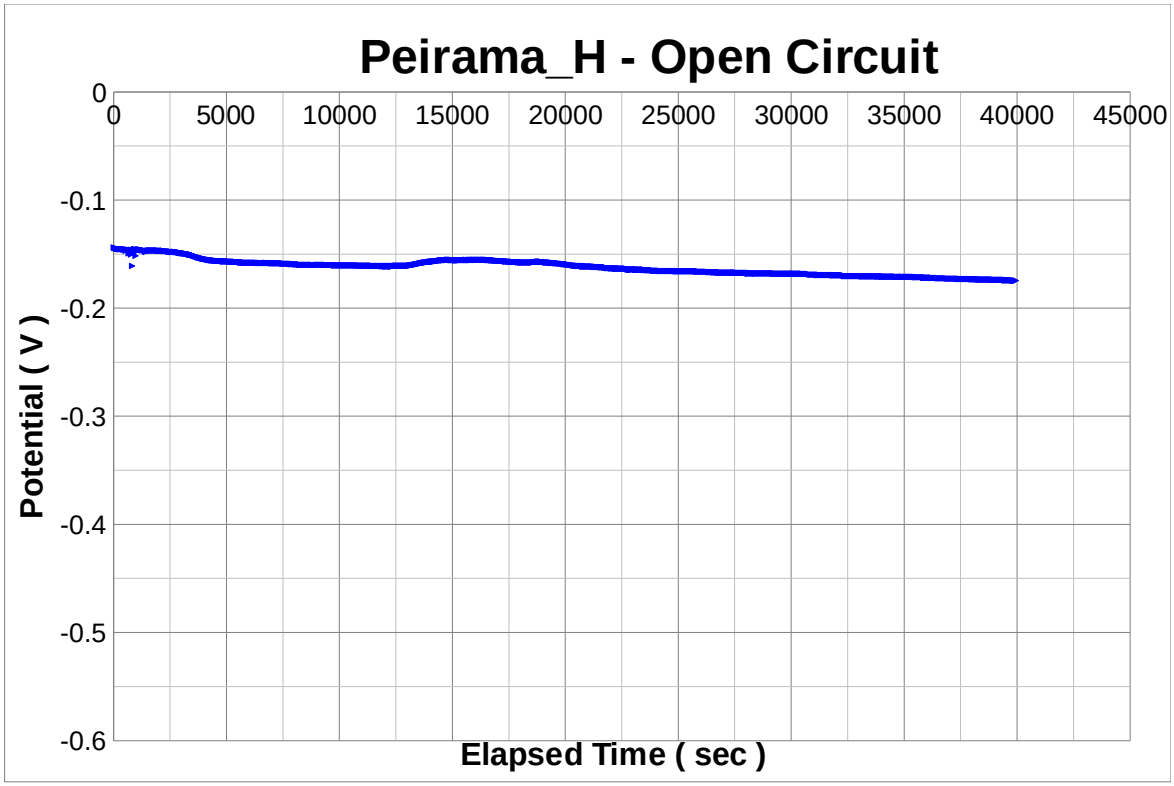

Fig. 86. Peirama_H- Treated copper surface for 10 days- Open Circuit Curve

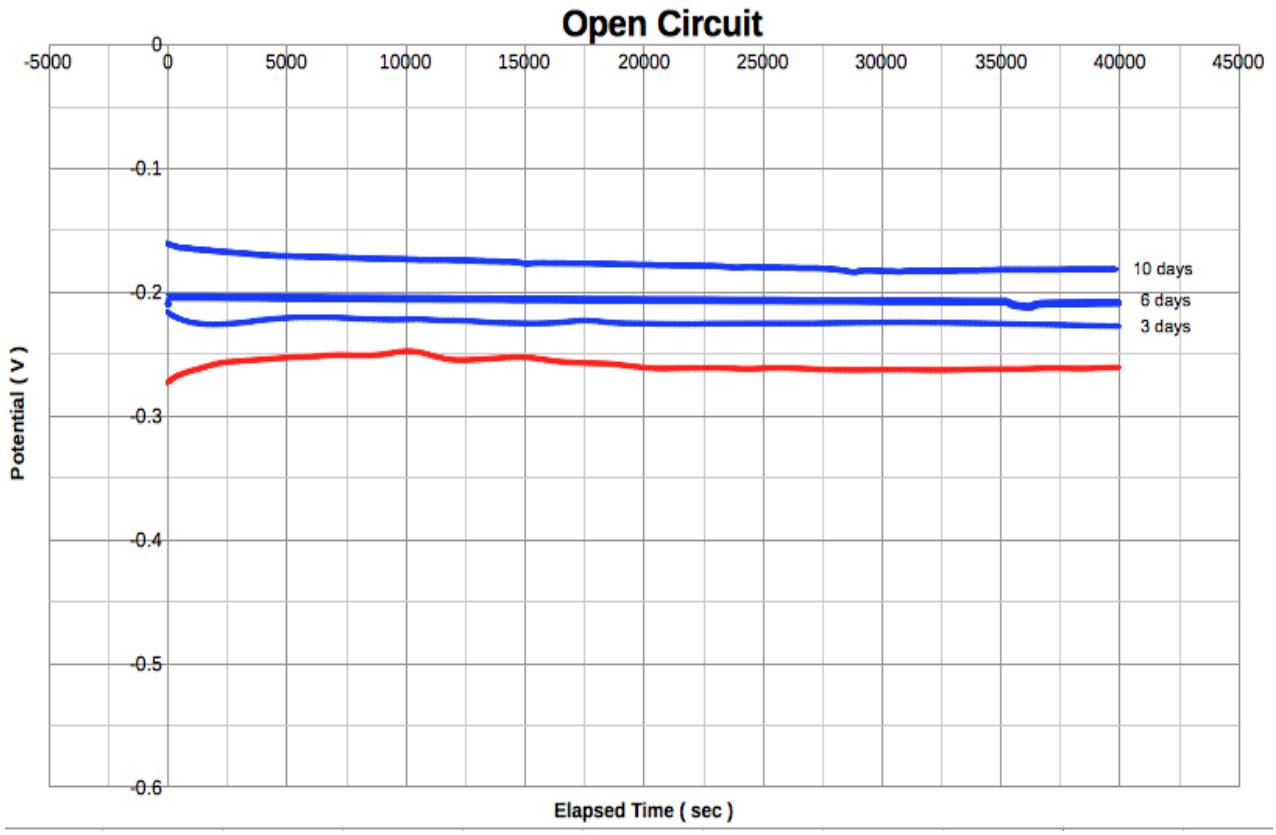

Fig.87. Open Circuit Curves for Treated and Bare Copper Surface

6.5.2. Potentiodynamic Experiments

In the Potentiodynamic polarization set of experiments, seven (7) electrochemical experiments were conducted:

- one for pure copper surface
- two for copper surfaces with 3 days immersion time in an ethanol solution of 0.06M n-tetradecanoic acid
- two for copper surfaces with 6 days immersion time in an ethanol solution of 0.06M n-tetradecanoic acid
- two for copper surfaces with 10 days immersion time in an ethanol solution of 0.06M n-tetradecanoic acid

A range of potential from -0,8Volts to +0,6 Volts, was applied, with scan ratio of 2 mV/sec. The curves obtained are presented in the following Fig. 90-97. The potentiodynamic experiments preceded the open circuit experiments.

In aerated Cl- solution the cathodic reaction is either water and/or the oxygen reduction according to

$$O_2 + 2H_2O + 4e^- \rightarrow 4OH^- \quad (1)$$

Oxygen reduction is the main cathodic reaction in aerated solution, which is responsible for the high cathodic, corrosion and anodic currents.The anodic dissolution of copper can be represented in all solutions as follows:

$$Cu \rightarrow Cu^+ + e^- \quad (2)$$

$$Cu^+ + Cl^- \rightarrow CuCl \quad (3)$$

$$Cu^+ + Cl^- \rightarrow CuCl_2 \quad (4)$$

Anodic currents in 3% NaCl alone display three distinct regions, Fig. 88.: a Tafel region at lower over-potentials extending to the peak current density i_{peak}, a region of decreasing currents until a minimum i_{min} is reached, and a region of sudden increase in current density leading to a limiting value i_{lim}. The anodic curves start with the dissolution of copper to form the cuprous ion equation (2) leading to an increase in the current to the maximum values i_{peak}. Then CuCl is formed on the copper surface equation (3), resulting in a decrease in the current to i_{min}, which then goes into the solution due to the formation of $CuCl_2^-$ equation (4), upon further potential increase, causing the current to increase again to i_{lim}. Copper is probably further oxidized to Cu(II) at higher potentials.

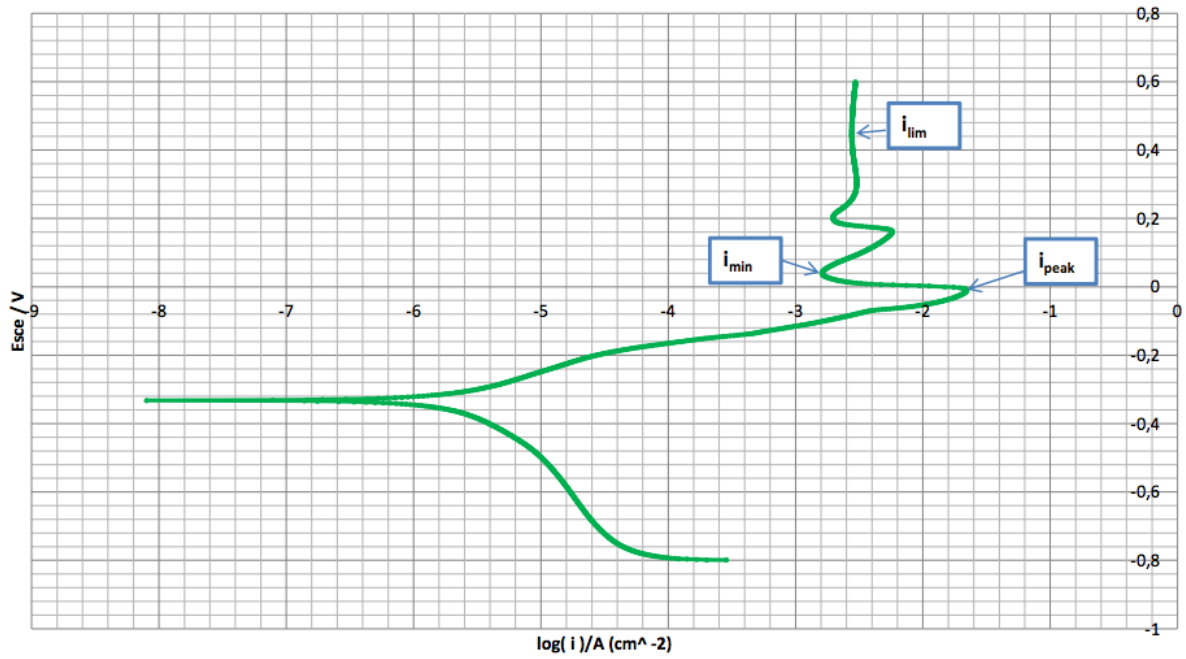

Fig. 88. Three district regions of the anodic current, *i*peak, *i*min, *i*lim.

From the Potentiodynamic curves the following results Table 3 were obtained, after applying Tafel fit for region of +25mV vs E_{corr}, in order to calculate I_{corr} . For the Tafel fit, it must be noted that only the anodic part of the curves was elaborated, Fig. 89.

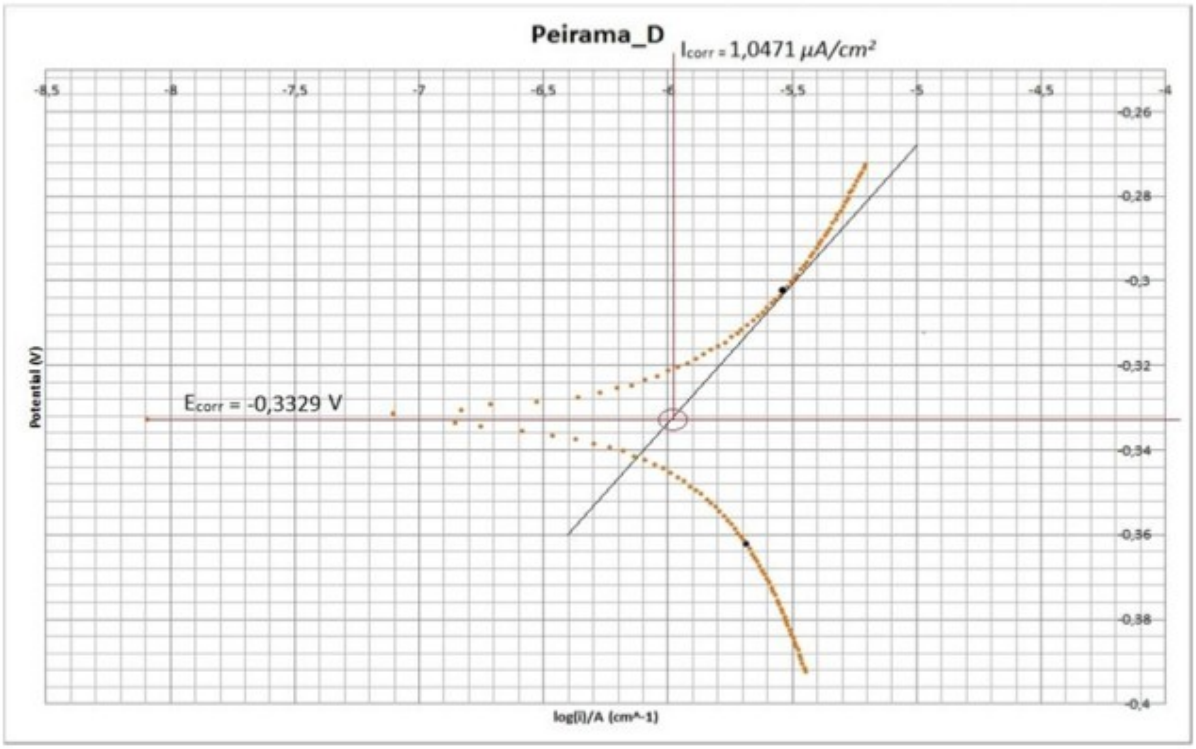

Fig. 89. Tafel fit for the anodic part of the potentiodynamic curves

The Corrosion Rate values were calculated from the following equation:

$$Corrosion\ Rate = \frac{0{,}13 * (EW) * I_{corr}}{d}$$

Where Corrosion Rate is in mpy(mili-inches per year), EW accounts for equivalent weight (gr), I_{corr} in μA/cm2 and d is for density (gr/cm3) .

Experiment	E_{corr} (mV)	Extreme log(i) (A/cm^2)	log(i_{corr}) (A/cm^2)	I_{corr} (μA/cm^2)	**Corrosion Rate (mpy)**
Peirama A	*-361.4*	*-5.809*	*-5.56*	*2.754*	***1.275***
Peirama B	*-282.5*	*-7.598*	*-5.61*	*2.455*	***1.137***
Peirama C	*-278.8*	*-7.698*	*-5.59*	*2.570*	***1.190***
Peirama D	*-221.3*	*-7.885*	*-5.8*	*1.585*	***0.734***
Peirama E	*-219.2*	*-7.835*	*-5.83*	*1.479*	***0.685***
Peirama F	*-175.1*	*-8.301*	*-6.15*	*0.708*	***0.328***
Peirama G	*-176.3*	*-8.181*	*-6.12*	*0.759*	***0.351***

Table. 3. Measurements of the Potentiodynamic Experiments

In presence of super-hydrophobic surface, both the cathodic and anodic currents, as well as corrosion currents, are shown to decrease and the E_{Corr} values shifted in the positive direction Fig. 90-97 super-hydrophobic surface produced positive results mainly on the copper anodic oxidation reaction, whose currents are reduced by about three orders of magnitude, the cathodic currents are reduced only by about one order of magnitude. Moreover, three distinct regions of anodic dissolution are not as obvious as bare sample. And the anodic dissolution currents do not increase sharply with over-potential. It indicates that the dissolution of copper and the transport of Cl- are strongly restrained by the super-hydrophobic film.

Reading the results of the Table 3 above, we can safely conclude that the treated specimens present superior behaviour against corrosion, comparing to the bare copper specimens. The corrosion rate measured for the bare copper specimens is , which is in accordance to the literature ~0.032 mm/year or 1,26 mpy (mili-inches per year). For the superhydrophobic surface of the 10 days immersion the corrosion rate is 3~4 times lower than this of the bare copper, for the 6 days immersed 2 times lower and even for the 3 days immersed is slightly better, approximately ~100 mili inches lower per year.

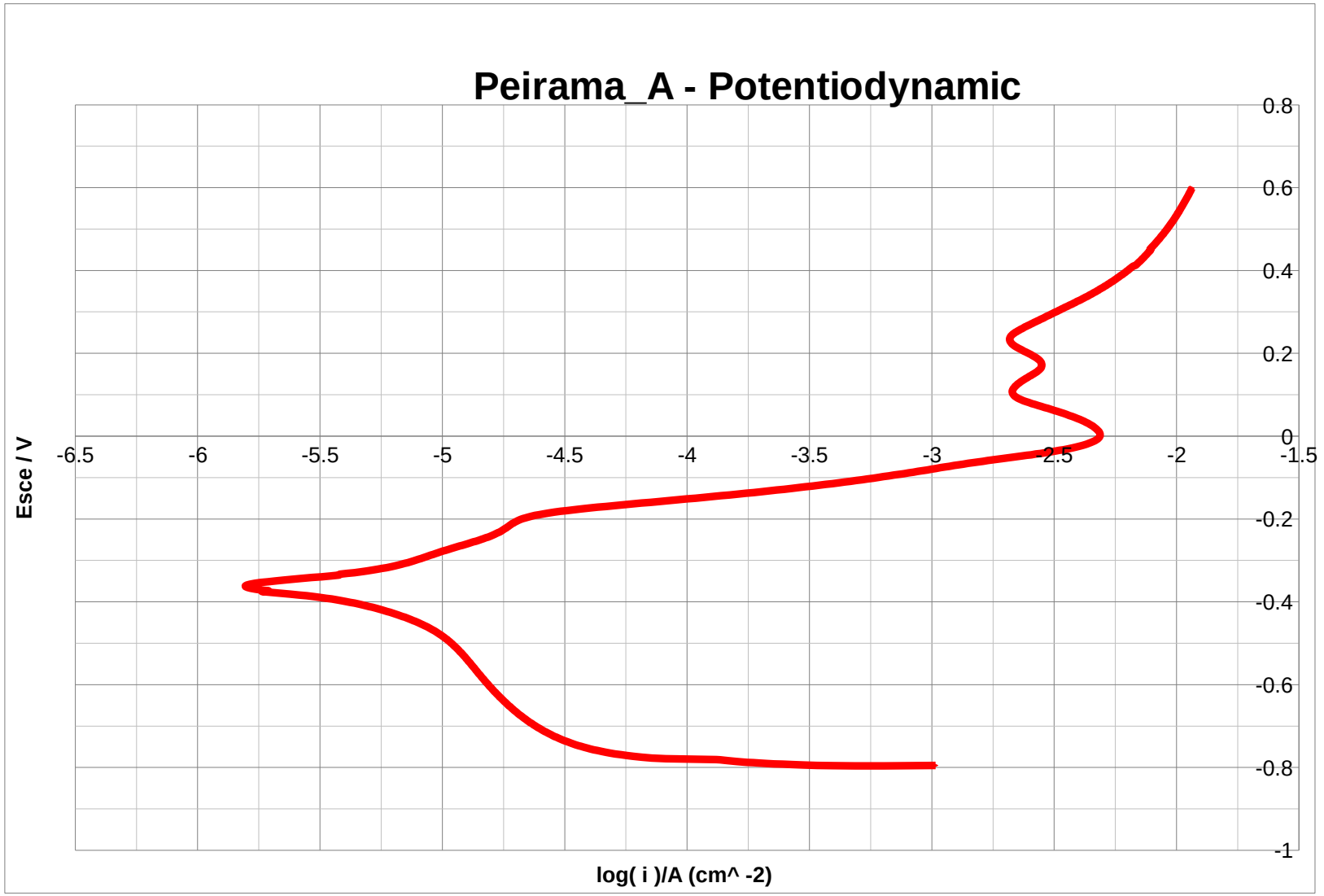

Fig. 90. Peirama_A- Bare copper surface- Potentiodynamic Curve

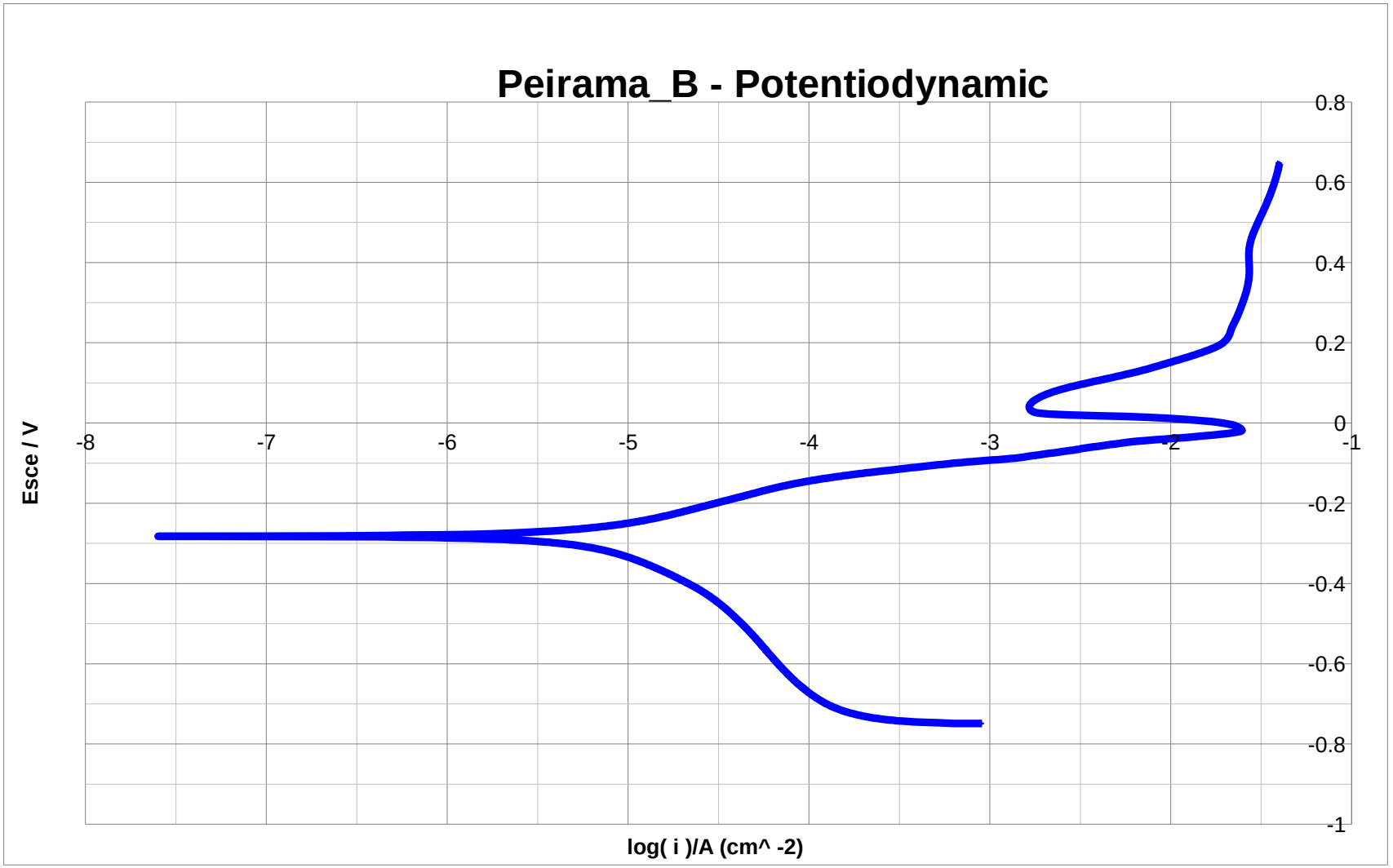

Fig. 91. Peirama_B- Treated copper surface for 3 days- Potentiodynamic Curve

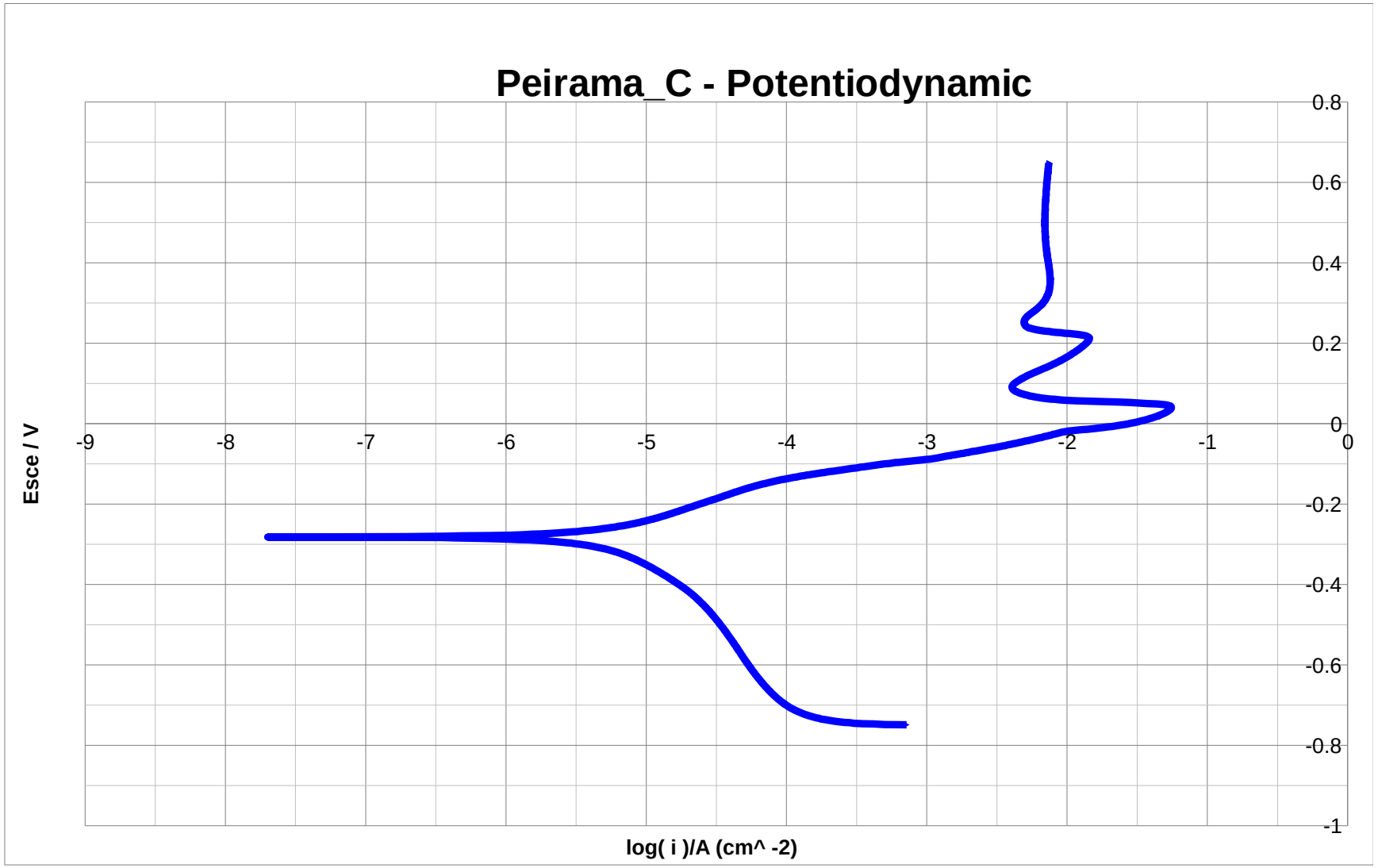

Fig. 92. Peirama_C- Treated copper surface for 3 days- Potentiodynamic Curve

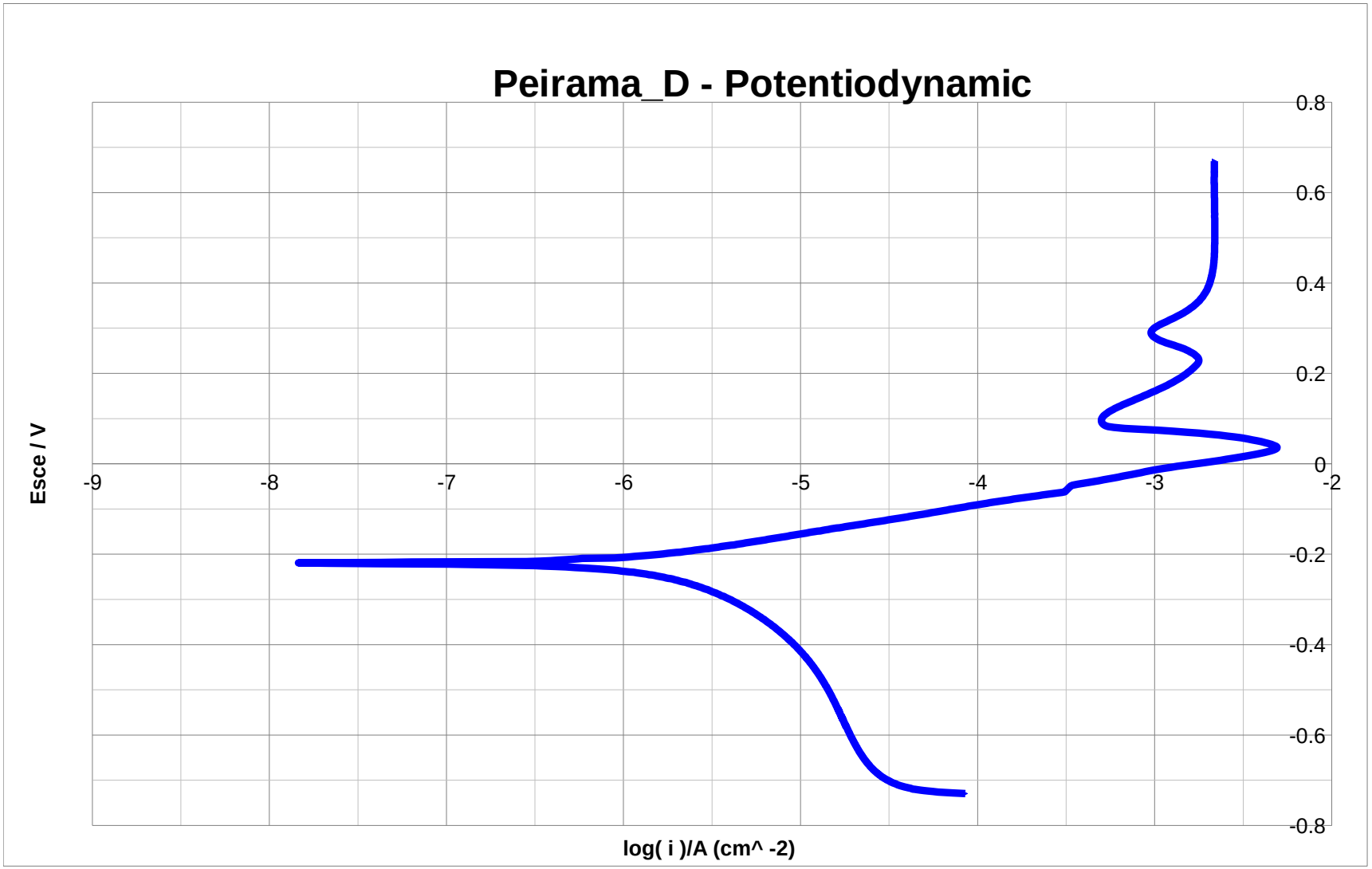

Fig. 93. Peirama_D- Treated copper surface for 6 days- Potentiodynamic Curve

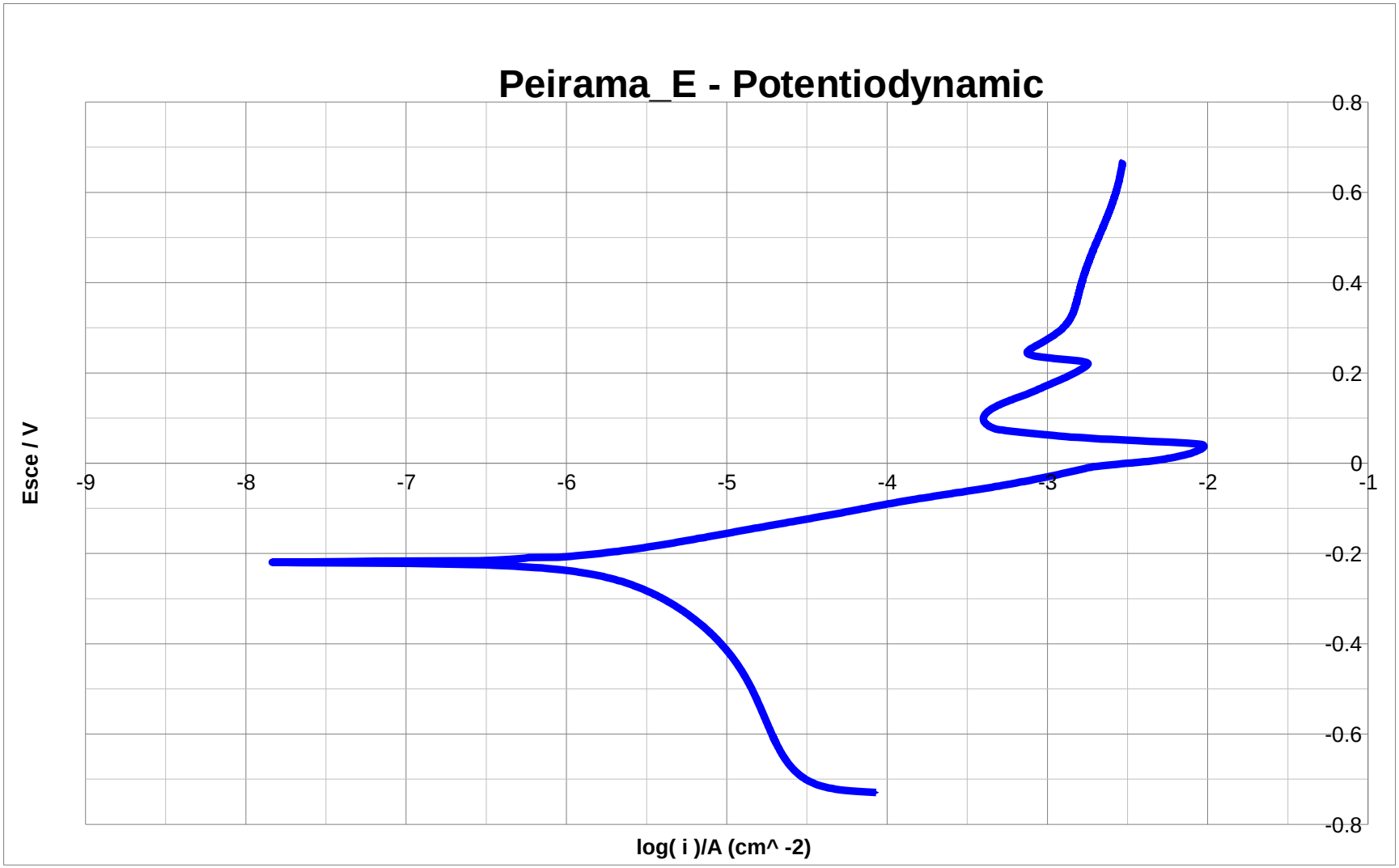

Fig. 94. Peirama_E- Treated copper surface for 6 days- Potentiodynamic Curve

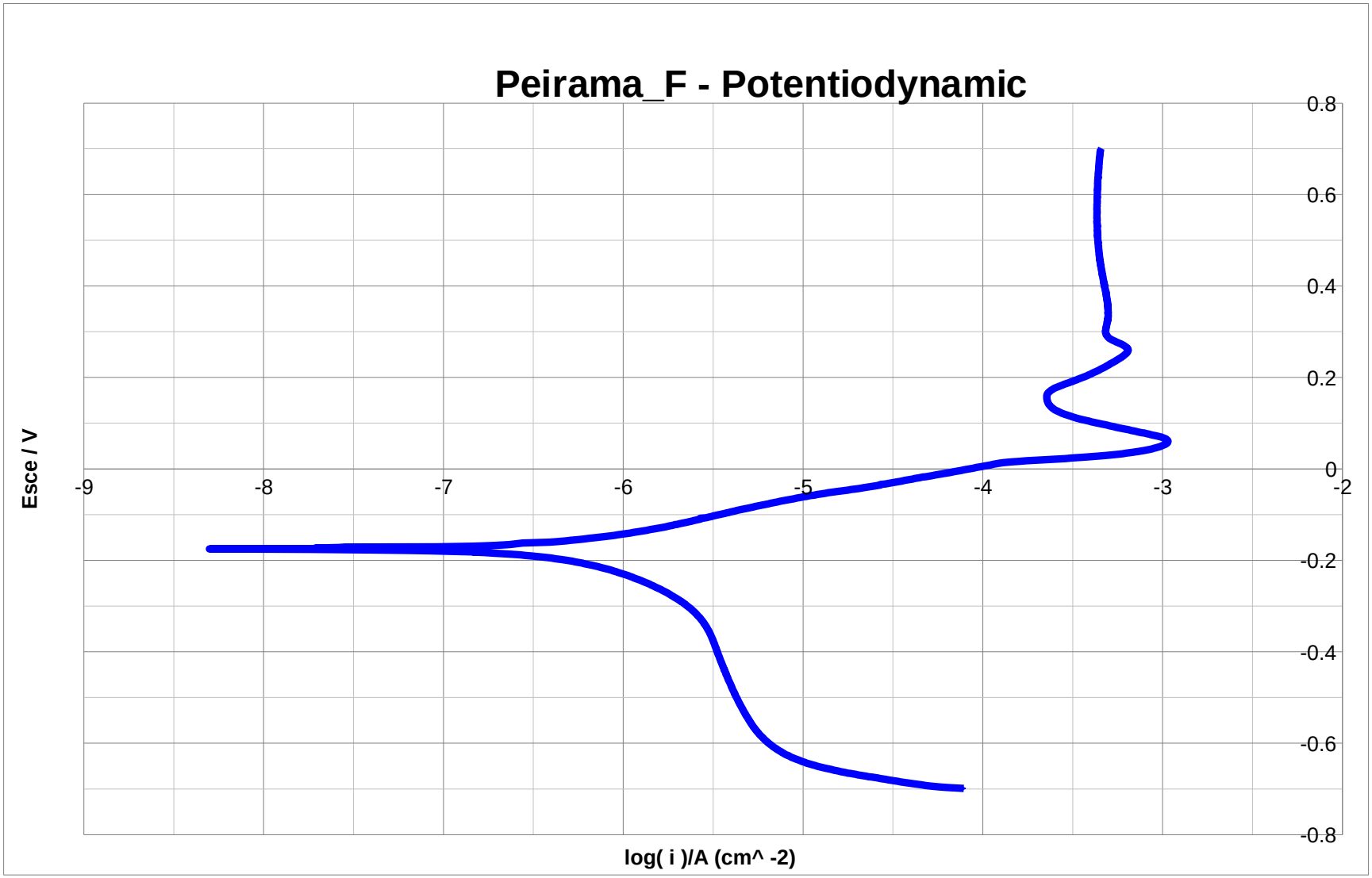

Fig. 95. Peirama_F- Treated copper surface for 10 days- Potentiodynamic Curve

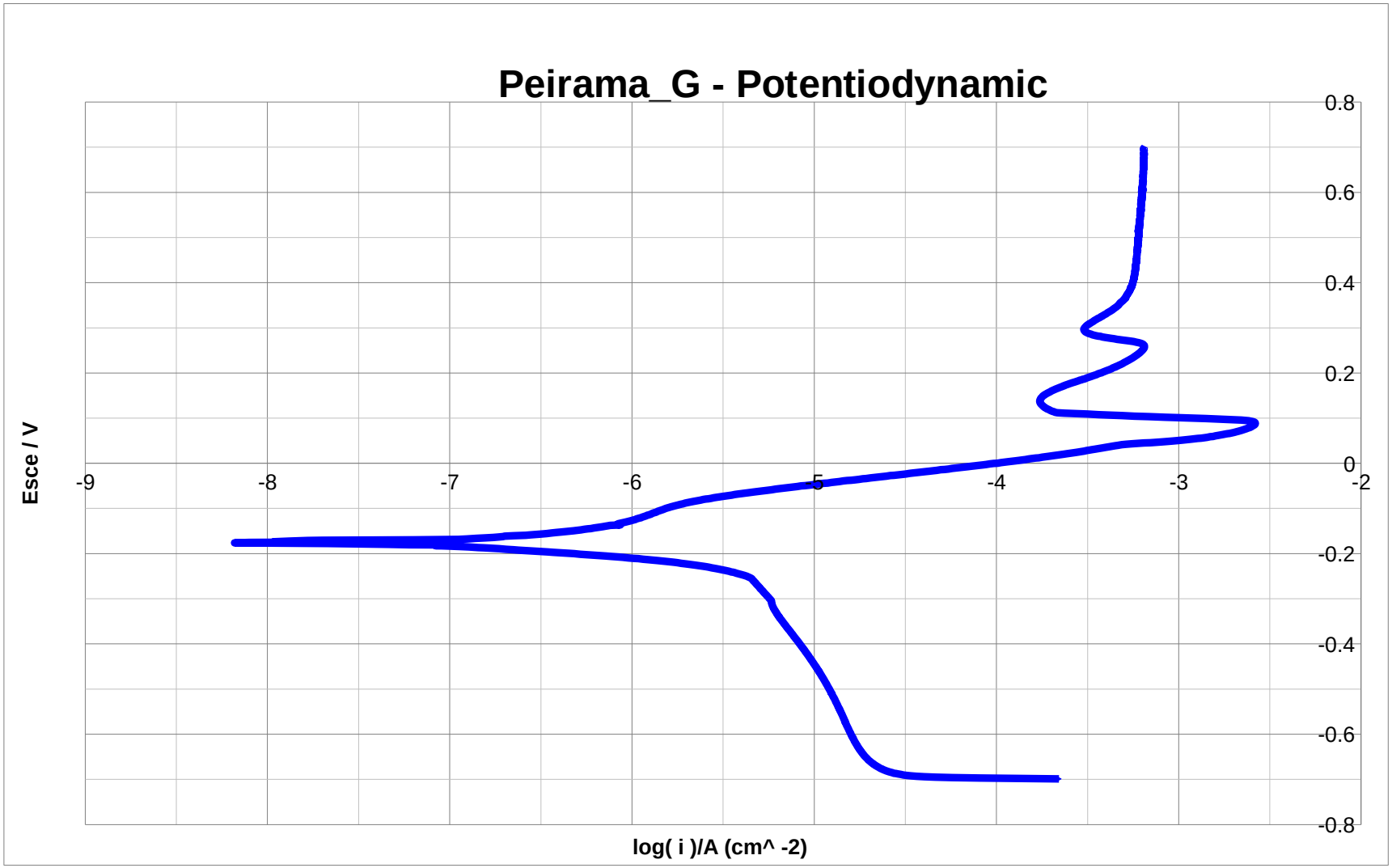

Fig. 96. Peirama_G- Treated copper surface for 10 days- Potentiodynamic Curve

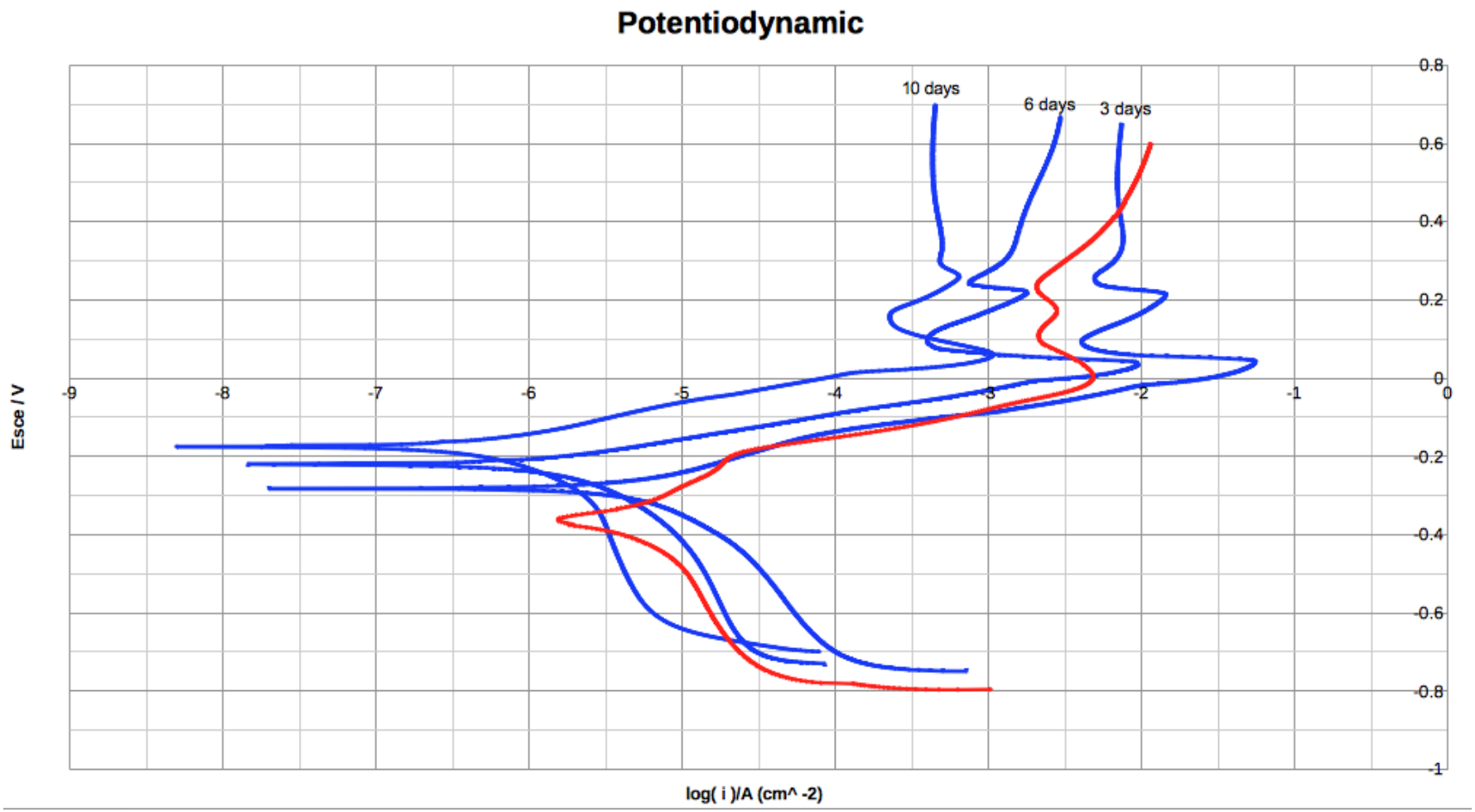

Fig. 97. Peirama_ - Potentiodynamic Curves

7. Conclusions

A series of parameters were examined in order to prepare a novel super-hydrophobic film on copper samples with a CSD method. The method we studied is simple and inexpensive. The front surface of the copper specimens were polished using silicon carbide papers from 80 to 1500 grade, then degreased with acetone, washed with distilled water and dried . Cu substrates should be etched in 70% HNO_3 for 10 s to remove surface oxides. T Subsequently they have to be immersed in an ethanol solution of 0.06M n- tetradecanoic acid, in an angle not bigger than 30°, for 10 full days at room temperature. The above is the optimized CSD method we came up to, after our experiments. The time and procedure are ideal for the fabrication of a stable flowerlike structure.

The contact angle measurements revealed that the difference between the treated and the clean surface is significantly large, more than two times. The measurements obtained for the clean copper are typical, and in accordance to the literature for super-hydrophobic treatments. For the 10 day immersed specimen the contact angle achieved was extreme, nearly 180°, so an extreme super-hydrophobic film was produced. For the 6 days and 3 days a decent super-hydrophobic and hydrophobic film were achieved respectively. We also tried and removed the coating from the treated specimen,the measured contact is still high, more than 100, implying that may be there is another layer, which still provides hydrophobic properties to the surface.

Stereo Microscopy and Scanning Electron Microscopy observations revealed a stable “flowerlike structure” of the surface, with mountain and valley areas. These observations combined with the results of the AFM images, prove that the structure of the n- tetradecanoic layer is a hierarchical structure (micro roughness covered with nano roughness). That hierarchical structure was not only necessary to have high contact angle but is also essential for the stability of the composite interface (water-solid and water- air).

Electrochemical experiments, Open Circuit and Potentiodynamic Polarization proved present superior behavior for the treated specimens against corrosion, comparing to the bare surface of the copper. The values of Ecorr and Icorr measured were significantly lower, meaning the super-hydrophobic film fabricated helps develop a higher corrosion resistance for the copper samples, with lower values for corrosion rate.

Summarizing, all experimental results proved that the super-hydrophobic surface can improve the corrosion resistance of copper significantly, playing an important role in corrosion behavior. A composite interface formed by the flowerlike surface nanostructures, water droplet and air trapped in the crevices is responsible for the superior water-repellent property we examined. Such surfaces are of great importance for many industrial applications, and may present a solution to long-standing problems of environmental contamination and corrosion of metals.

8. Bibliography

[1] Peng Wang, Dun Zhang, Ri Qiu, “Liquid/solid contact mode of super-hydrophobic film in aqueous solution and its effect on corrosion resistance”, Corrosion Science 54 (2012) 77–84

[2] Peng Wanga, Ri Qiua, Dun Zhanga, Zhifeng Lina, Baorong Houa, “Fabricated super-hydrophobic film with potentiostatic electrolysis method on copper for corrosion protection”, Electrochimica Acta 56 (2010) 517–522

[3] Y.Y. Yan, N. Gao , W. Barthlott , “Mimicking natural superhydrophobic surfaces and grasping the wetting process: A review on recent progress in preparing superhydrophobic surfaces”, Advances in Colloid and Interface Science 169 (2011) 80–105

[4] Tao Liu, Yansheng Yin, Shougang Chen , Xueting Chang, Sha Cheng, “Super-hydrophobic surfaces improve corrosion resistance of copper in seawater”, Electrochimica Acta 52 (2007) 3709–3713

[5] Tao Liu, Shougang Chen, Sha Cheng, Jintao Tian, Xueting Chang, Yansheng Yin, “Corrosion behavior of super-hydrophobic surface on copper in seawater”, Electrochimica Acta 52 (2007) 8003–8007

[6] Zhiguang Guo, Weimin Liu, Bao-Lian Su, “Superhydrophobic surfaces: From natural to biomimetic to functional”, Journal of Colloid and Interface Science 353 (2011) 335–355

[7] Elena Celia, Thierry Darmanin, Elisabeth Taffin de Givenchy, Sonia Amigoni, Frédéric Guittard , “Recent advances in designing superhydrophobic surfaces”, Journal of Colloid and Interface Science 402 (2013) 1–18

[8] Liqun Zhu, Yan Jin, “A novel method to fabricate water-soluble hydrophobic agent and super-hydrophobic film on pretreated metals”, Applied Surface Science 253 (2007) 3432–3439

[9] Ming-De Pei, Bo Wang, Er Li, Xue-hong Zhang, Xue-mei Song, Hui Yan, “The fabrication of superhydrophobic copper films by a low-pressure-oxidation method”, Applied Surface Science 256 (2010) 5824–5827

[10] Kyungjun Leea, Sungnam Lyua, Sangmin Leea, Youn Sang Kimb, Woonbong Hwanga, “Characteristics and self-cleaning effect of the transparent super-hydrophobic film having nanofibers array structures”, Applied Surface Science 256 (2010) 6729–6735

[11] Xiuqing Xu, Liqun Zhu, Weiping Li, Huicong Liu, “A variable hydrophobic surface improves corrosion resistance of electroplating copper coating”, Applied Surface Science 257 (2011) 5524–5528

[12] Xianfeng Wanga, Bin Dinga,b, Jianyong Yub, Moran Wangd, “Engineering biomimetic superhydrophobic surfaces of electrospun nanomaterials”, Nano Today (2011) 6, 510—530

[13] Hans J. Ensikat, Petra Ditsche-Kuru1, Christoph Neinhuis, Wilhelm Barthlott1, "Superhydrophobicity in perfection: the outstanding properties of the lotus leaf", Beilstein J. Nanotechnol. (2011), 2, 152–161.

[14] Anna J. Schulte, Damian M. Droste1, Kerstin Koch, Wilhelm Barthlott, "Hierarchically structured superhydrophobic flowers with low hysteresis of the wild pansy (Viola tricolor) – new design principles for biomimetic materials", Beilstein J. Nanotechnol. (2011), 2, 228–236.

[15] Yoseph Bar-Cohen, "Biomimetics—using nature to inspire human innovation", Bioinsp. Biomim. 1 (2006) P1–P12

[16] Mengnan Qua, Jinmei Hea and Junyan Zhang, "Superhydrophobicity, Learn from the Lotus Leaf", ISBN: 978-953-307-025-4, InTech

[17] Hans J. Ensikat, Matthias Mayser, and Wilhelm Barthlott, "Superhydrophobic and Adhesive Properties of Surfaces: Testing the Quality by an Elaborated Scanning Electron Microscopy Method", Langmuir (2012), 28, 14338−14346

[18] Reiner Furstner and Wilhelm Barthlott, "Wetting and Self-Cleaning Properties of Artificial Superhydrophobic Surfaces", Langmuir (2005), 21, 956-961

[19] Hans J. Ensikat, Anna J. Schulte, Kerstin Koch, and Wilhelm Barthlott, "Droplets on Superhydrophobic Surfaces: Visualization of the Contact Area by Cryo-Scanning Electron Microscopy", Langmuir (2009), 25(22), 13077–13083

[20] L.Nunez, E. Reguera, F. Corvo, E. Gonzalez, C. Vazquez (2005), Corrosion of copper in seawater and its aerosols in a tropical island, Corros. Sci. 47, 461-484.

[21] S.Wang, L. Feng, L. Jiang, (2006), One-Step Solution-Immersion Process for the Fabrication of Stable Bionic Super-hydrophobic Surfaces, Adv. Mater. 18, 767-770.

[22] Th. Tsiourva, A. Fellios, A. Karantonis, D. I. Pantelis, Corrosion behavior of super-hydrophobic film on copper substrate in 3.5% NaCl solution, (2014)